Astronomy & Astrophysics

(CAUCASUS)

International Scientific Journal

2

SAMTSKHE-JAVAKHETI STATE UNIVERSITY PRESS

2016

UDC 52(050)(479.22)

A-89

Astronomy & Astrophysics

(CAUCASUS)

Samtskhe-Javakheti State University Press

Email: astronomy@sjuni.edu.ge

EDITOR'S NOTE

The second volume of the international scientific journal Astronomy & Astrophysics (Caucasus) contains the scientific works delivered as scientific reports by their authors at International Scientific Conference Modern Problems of Astrophysics – II' held at Samtskhe-Javakheti State University on September 26-28, 2016.

Many world leading scientists were invited to the International Scientific Conference as participants, who delivered up to 30 interesting reports (including the sponsored articles).

Second Volume presents only the scientific works delivered by 8 speakers (and 27 co-speakers) written at about 15 leading scientific establishments of the world. Other Conference materials will be published in the third volume of the same scientific journal.

Professor Revaz Chighladze,

Doctor of Physical and Mathematical Sciences, Editor of international scientific journal "ASTRONOMY & ASTROPHYSICS (CAUCASUS)".

Astronomy & Astrophysics (Caucasus) 2, (2016) (4-16)

DETERMINATION OF MONOCHROMATIC COEFFICIENTS OF ABSORPTION OF MOLECULAR GASES IN THE ATMOSPHERE OF JUPITER AND SATURN

A. A. Atai[1] and E. R. Yuzbashov[2]

1. Shamakhi Astrophysical Observatory named after N. Tusi of Azerbaijan National Academy of Sciences

2. Institute of Physics of Azerbaijan National Academy of Sciences

Email: atai1951@yahoo.com

Abstract

A new method to determine the monochromatic absorption coefficients' values of ammonia in a visible range of the spectrum for atmospheres of Jupiter and Saturn has been proposed on the base of observed and laboratory spectral data for the corresponding bands. The calculation of values k_ν in a thermal mode for atmospheres of Jupiter and Saturn was conducted by "fitting" of the laboratory data of the planetary atmosphere. The results of the calculation show that in the conditions of atmospheres of Jupiter and Saturn in far wings of the absorption band NH_3 λ 6475 Å, the values of k_ν are comparable with the laboratory measurements, but in the central region of this band the deviation increases even approximately by ~2.8 times.

As mentioned, the measurements of monochromatic absorption coefficients for ammonia were done at a room temperature. Therefore, the determination of those coefficients in the conditions of Jupiter and Saturn is of a great interest. According to the laboratory measurements, band $6\nu_1$ (λ 5520 Å) is weaker than band $5\nu_1$ (λ 6475 Å) approximately by 6,5 times. The calculated integral absorption coefficients for bands NH_3 λ 6475 Å and λ 5520 Å in the spectrum of Jupiter differ by 8 times.

Key words: Jupiter, Saturn, monochromatic coefficients, absorption coefficients, NH_3, 6475 Å band

Received October 19, 2016; revised December 19, 2016

1. Introduction

The study of complex vertical structure of the atmospheres of the giant planets is an important part of the study of dynamic processes in the physics of atmospheric phenomena. When studying the vertical structure of the atmospheres of the giant planets, there arises a great deal of difficulties associated with the choice of the atmospheric model. Therefore, the analysis of even the same observation data, in terms of different assumptions of the vertical structure of a cloud layer, gives different values of the parameters to determine. For the detailed study of the given issue, it is necessary to systematize the available data more thoroughly and consider a number of important factors, such as the dependence of the values of monochromatic coefficients of absorption of molecular gases k_ν on pressure and temperature, as well as the role of aerosol scattering, accurate identification of the relative concentration of gases, efficient optical thickness, etc.

As it is known, sizeable absorptions in the spectra of the giant planets are mostly associated with the presence of methane, ammonia and their compounds that make up a small proportion of their

atmospheres, but play an important role in the dynamic processes of the atmospheric phenomena (the role nearly similar to that played by the water vapor in the earth's atmosphere), and create color shades of the planets. The above-said is also true with the atmosphere of Saturn.

The main components of the atmospheres of the giant planets are hydrogen and helium, which create great partial pressures and in their turn, affect the formation of absorption bands of NH_3 and CH_4 and lead to the shift and extensions of these spectral lines. As a result, the observed spectra of these gases differ significantly from the laboratory spectra of the corresponding gases.

A growing number of laboratory and theoretical studies of the peculiarities of the absorption lines of ammonia and methane, depending on the temperature and pressure (Keffer Ch.E. et al, 1986, 1986a; Smith W.H. et al, 1990; Mickelson M.E. et al,. 1991; Ramaprasad K.R. et al, 1978) have inspired some new works (Karkoshka E., 1994; Karkoschka E. & Tomasko M.G., 1992; Karkoschka E., 1998; Lyulin O.M. et al., 2011) in the field of modeling the atmospheres of the giant planets. In particular, more exact locations of the lines, their intensity, expansion coefficients of the lines as a result of the collision (expansion during the collisions with other molecules) and self-expansion under the pressure (collision takes place between the molecules of the same sort). The works (Keffer Ch.E. et al., 1986, 1986a; Lyulin O.M. et al., 2011) give the calculation of the half-widths of some lines of methane and ammonia as a result of pressure created by various gases within eth temperature range of $77–295^0$K.

The dependence of the absorption coefficients on the temperature is seen in the change of both, the intensity of the absorption lines and half-widths of the spectral lines. The impact of temperature on the absorption coefficient plays a secondary role as compared to the pressure, but despite this, the impact of temperature must be considered in calculating the absorption coefficients. Ramaprasad K.R. et al. (Ramaprasad K.R. et al., 1978) demonstrated that in the field of low temperatures, even in case of measurements with a low spectral resolution, the methane absorptions show a considerable dependence on temperature.

For most absorption spectra, the overlap of the spectral lines having different intensities and half-widths of the absorption lines, as well as different temperature dependencies, lead to a very complex dependence of the absorption coefficients on temperature. This dependence is a function of a wave number and changes with the change of pressure. Chou and Arking (Chou M.D. & Arking A., 1980) represented the dependence of monochromatic absorption coefficients of spectral lines of band ν_4 NH_3, disturbed by the action of N_2, on temperature by the following formula: $k_\nu(T) = \kappa_\nu(T_0)\cdot(a_\nu + b_\nu T + c_\nu T^2)$, and identified the decline of the absorption coefficient with the temperature decline.

According to Shi Zhang (Shi G. Zhang, 2007) and Bauer A. et al. (Bauer A. et al., 1993), the dependence of absorption coefficient $k_\nu(T)$ on temperature can be presented by a simple power law:

$$k_\nu = k_\nu(T_0)\left(\frac{T}{T_0}\right)^A$$

where A is temperature exponent and T_0 is the attached temperature (T_0=235 K).

The first attempt to determine the absorption coefficients for bands CH_4 in terms of the planet atmospheres is seen in the works (Karkoshka E., 1994; Karkoschka E. & Tomasko M.G., 1992; Karkoschka E., 1998) for all giant planets, as well as for the atmosphere of Titan. E. Karkoschka (Karkoschka E., 1998) points to the existence of a new absorption band in the Jupiter and Saturn spectra close by λ 9300 Å (identifying it by means of ammonia absorption), and also offers a new method to determine the temperature of the atmospheric layers, at which the methane absorption bands are formed. However, at the same time, he puts forward some requirements for determining the temperature of the atmospheric layers, which are not always possible to meet.

Unfortunately, at present, no reliable data about k_ν, available for methane (Smith W.H. et al., 1990; Mickelson M.E. et al., 1991), are available for ammonia even in laboratory conditions (the

differences of k_ν is approximately 10% in the centers of the absorption banks and differ by several times near the continuous spectrum. The results of the preliminary calculations to determine k_ν for ammonia were published in the work by Atai (Atai A.A., 2009).

A.V. Morozhenko (Morozhenko A.V., 2002, 2003) cast a doubt to the results of the research by E. Karkoschka et al. (Karkoschka E. & Tomasko M.G., 1992; Karkoschka E., 1998). Based on the analysis of the laboratory data of Smith et al. (Smith W.H. et al., 1990) as well as M.E. Mickelson et al. (Mickelson M.E. et al., 1991), he identified a principally new method to define the monochromatic absorption coefficients for CH_4 for giant planets more accurately. The authors of the work (Morozhenko A.V. & Ovsak A.S., 2009) had to adjust the results of the previous works because of the difference of the values of pressure obtained with KA "Galileo" (Ragent B. et al., 1998).

In his recently published work, Morozhenko (Morozhenko A.V., 2009) notes that in addition to the existing three bands of ammonia absorption (λ = 5520, 6450 и 7920 Å), the Jupiter spectrum contains a depression wavelength λ=6040Å, with its shape resembling the ammonia absorption band, and which is absent in the spectra of Uranus or Neptune. In addition, by considering that the assessable values of monochromatic absorption coefficients for k_ν for some ammonia bands is the superposition of the coefficients of two gases:

$$k_\nu = k_\nu (CH_4) + \gamma' k_\nu (NH_3), \quad (1)$$

he identified the values of product of γk_ν and $\gamma' k_\nu$ (where γ, γ are the relative concentrations of ammonia in relation to the hydrogen-helium mixture and methane, respectively).

In the works (Morozhenko A.V., 2002, 2003, 2006; Morozhenko A.V. & Ovsak, A.S., 2009), the recalculated values of k_ν for thermal conditions in the atmospheres of planets is done by successive approximations. At the same time, we found some incorrectness in an expression used to calculate the effective optical depths by E.G.Yanovitskiy (Avramchuk V.V., 1977).Therefore, the authors of the works (Morozhenko A.V. & Ovsak, A.S., 2009) failed to even identify an approximate error of k_ν and therefore, these data could not to be unique. Therefore, the given method of A.V. Morozhenko approximately restores the vertical structure of cloud layers of the giant planets.

In recent decade, the study of giant planets have also been carried out with the help of space telescope "Hubble", space probes "Cassini-Huygens" and "Galileo". The new data gained from the spacecrafts (Huygens probe, HST - Hubble Space Telescope), as well as images obtained at eh moment of the launch of a Spectral Radiometer (DISR - Descent Imager Spectral Radiometer) inspired E. Karkoshka and M. Tomasko (Tomasko MG et al, 2008; Karkoschka E. & Tomasko MG, 2010) to return to their previous work and to revise the conditions of gas absorption in the atmospheres of planets the Jupiter group.

Clearly, it would be useful, if such an important parameter as the monochromatic absorption coefficient were determined by the laboratory measurements by using a simpler method. This work is an attempt to reach this goal to determine the monochromatic absorption coefficients in the bands of ammonia (λ5520 Å, λ 6475 Å) and methane (λ 6190 Å) in the spectra of Jupiter and Saturn based on the laboratory measurements for the same absorption bands.

2. Description of the method

As it is known, in the real planetary atmospheres, there is quite a complicated vertical profile of a temperature and pressure. If we assume that the values of these parameters are constant in each individual layer, in the observed reflected spectrum of the planet, the contributions of all the layers are summed up. Therefore, the corrections to the laboratory values of k_ν (T_0; P_0) will be different for the different portions of the circuit of the absorption band (where, T_0,P_0 are the values of temperature and pressure conditions in the laboratory).

The simple method offered by us to find the values of monochromatic absorption coefficient for molecular gases is based on the analysis of data of the observed spectrum of the planets and the values of the laboratory spectrum of the given absorption molecular gas band (Lutz B.L. et al., 1982), by considering the deviation of the vertical structure of the cloud layer from the condition of homogeneity (Morozhenko the A.V., 2002, 2003, 2006). In order to consider the deviation of the vertical structure of the cloud layer from the condition of homogeneity, a graph dependence of ln (Nl/τs) on ln (Nl) was construed in the contours of different bands of absorption of molecular gases. Here, Nl is the amount of gas in the line of sight (km•amagat) (or m•amagat) and τs is the scattering component of the effective optical depth τ_{eff} of forming diffusive-reflected radiation by means of a homogeneous semi-infinite layer, the values of which are determined by albedo data of a single scattering in the molecular ω_ν absorption band and in the continuous spectrum ω_c:

$$\frac{Nl}{\tau_s} = \frac{\omega_\nu^{-1} - \omega_c^{-1}}{k_\nu} = \frac{\bar{n}}{\bar{\sigma}_s}, \quad (2)$$
$$Nl = \left(Nl \big/ \tau_s \right) \tau_{eff}\, \omega_\nu$$

Here k_ν is a monochromatic ammonia absorption coefficient, $\bar{\sigma}_s$ and $\bar{n}$ are averaged values of gas volume concentrations and volume coefficients of the environment scattering along the entire optical path. For plotting the dependence of ln (Nl / τs) on ln (Nl), the observation spectral geometric albedo values (or luminance factor) for the given absorption band is needed. In addition, it is necessary to know about the spectral course of these values in the zone of the spectrum of the planet, where no absorption of molecular gases occurs. It is in this spectral region, one can assume that is the absorption of aerosol is predominant and it is ascribed to the absorption in the continuous spectrum. Based on these values, the contribution of aerosol absorption in the continuous spectrum of the reflection of the planets is calculated.

As it is known, in the spectra of the giant planets, the absorption bands of molecular gases are formed starting from the zone of spectrum λ> 4300 Å and intensifies in the direction of the long-wave portion of the spectrum, while the role of the aerosol decreases and the level of the continuous spectrum is reduced, mostly at the expense of intensifying gas absorptions.Therefore, it is very important to know about the course of brightness in the zones of the spectrum, in which the absorption in CH_4 bands is almost imperceptible. When λ> 5000 Å, the existence of multiple absorption bands in the spectra of the giant planets makes the calculation of the aerosol absorption in the continuous spectrum difficult. It is in these areas of the spectra of Jupiter and Saturn, is a linear decrease of the aerosol absorption is observed. We can therefore assume that the nature of the spectral dependence of the aerosol absorption is described by the same interpolation expression for all absorption bands.

As noted above, many gas molecular absorption parameters depend on thermodynamic conditions (such as temperature and pressure). On the other hand, some of the typical gas qualities, such as the relative changes in energy transitions responsible for the formation of the absorption band almost remain unchanged. For example, the dependence graphs of ln (Nl / τs) = f (ln (Nl)), obtained on the basis of the laboratory data for absorption bands NH3 λ6475Å, λ5520Å coincide (within the limits of error) with similar graphs drafted on the basis of the calculated values of k_ν, corresponding to the atmospheric conditions of Jupiter in the above-mentioned absorption bands.

Spectral values of ω are determined by comparing the values of the observed reflective coefficients of brightness (or A_g) with the estimated data for the model of an optically homogeneous semi-infinite layer. To calculate τ_{eff}, E.G. Yanovitskij (Yanovitskij E.G., 1997) offered a new method, the essence of which is as follows: as it is known, in reality, the absorption spectrum of a planet is determined with relative error ε, and the valid information about the optical properties of the medium are carried only by the photons, which are mainly scattered only in the corresponding surface layer of the atmosphere. After all, the changes in the optical properties of the atmosphere in the quite deep

layers of the medium can be recorded by means of observations provided they are accomplished with due accuracy. This is why, the author of the work (Yanovitskij E.G., 1997) preferred to determine effective optical thickness (τ_0^e) of the surface layer of the semi-infinite atmosphere, in which the observed spectrum of the planet in the frequency ν is formed from the equation at the given accuracy of the observations:

$$\frac{\rho_\infty(\mu,\mu_0,\varphi-\varphi_0)-\rho(\mu,\mu_0,\varphi-\varphi_0,\tau_0^e)}{\rho_\infty(\mu,\mu_0,\varphi-\varphi_0)}=\varepsilon\,, \quad (3)$$

where $\rho(\mu,\mu_0,\varphi-\varphi_0,\tau_0^e)$ are the reflection coefficient of the surface layer of the atmosphere with optical thickness τ_0^e, isolated from the entire semi-infinite atmosphere. Such an assessment is necessary when interpreting any spectral or photometric observations of the planets. We used the results of the calculations (Yanovitskij E.G., 1997) to assess τ_0^e for given ε for the simplest model of the plane homogeneous semi-infinite atmosphere, although equation (2) applies to any non-homogenous model of the atmosphere. The presented results of numerical calculations of value τ_0^e at scattering angle $\gamma=\pi$ show that value τ_0^e is relatively weakly dependent on the angle of light incidence, but greatly depends on the optical properties of the atmosphere, especially on the shape of the indicatrix of scattering (Morozhenko A.V., 2004). It should be noted that the physical characteristics of the particles of the upper cloud layers of atmospheres of Jupiter and Saturn, determined by polarimetric measurements (Morozhenko A.V., 2004), allow estimating the spectral values of the scattering indicatrix.

When plotting the function of ln (Nl / τ_s) on ln (Nl) calculations were performed for Rayleigh, as well as a two-term of the scattering Henyey-Greenstein

$$\chi(a)=\frac{a(1-g_1^2)}{(1+2g_1\cos a+g_1^2)^{\frac{3}{2}}}+\frac{(1-a)(1-g_2^2)}{(1+2g_2\cos a+g_2^2)^{\frac{3}{2}}}\,, \quad (4)$$

where the parameters have the following values: a = 0.938, g_1 = 0.90 and g_2 = - 0.23 [21].

Thus, the procedure to determine the monochromatic absorption coefficient for k_ν in the atmosphere of the planets can be briefly described as follows: based on the laboratory measurements of NH_3 and CH_4 absorption spectra, the graphs of dependence between ln (Nl/τ_s) and ln (Nl) for a given wavelengths are drafted. Then, for the same selected wavelengths, the corresponding values of ln(Nl) and β_ν are selected, where $\beta_\nu=\omega_\nu^{-1}-\omega_c^{-1}$. Then, the value of ln (Nl / τ_s) is calculated based on the same dependence drafted based on the observed spectra of a planet. Consequently, the value of β_ν/κ_ν is calculated for the planet, and the value of k_ν in a planetary atmosphere is determined as the next step.

Thus, based on the laboratory spectra and measurements of monochromatic absorption coefficient for bands NH_3 λ 6475 Å, X 5520 Å and CH_4 λ 6190 Å at room temperature, as well as observed spectra of Jupiter and Saturn, the value of k_ν for the specified bands in a thermal regime of these planets is determined.

3. COMPUTING RESULTS

CH_4 λ 6190 Å. In order to be sure of the reliability of the results obtained by us, we calculated the monochromatic absorption coefficient values for methane in absorption band of CH_4 λ 6190 Å by using the above-mentioned method. For this purpose, we selected the observational data for the

equatorial zones of Jupiter and Saturn obtained by F. Moreno and A. Molina (Moreno F. & Molina A., 1990, 1991), J. Ortlza et al. (Ortlz J.L. et al, 1992) , J. Woodman et al. (Voodman J.H. et al, 1979), M.S. Dementyev et al. (Dementyev M.S. & Morozhenko A.V., 1990), as well as the measurements on photovoltaic spectrophotometry of S. M. Gaysina (Gaysin S.M., 1979) and V.D. Vdovichenko (Vdovichenko V.D., 1980).

In order to do the calculations, in the first place, we chose the observational data obtained on December 5th and 6th of 1976 on the basis of photoelectric measurements with single-channel and dual-channel scanning spectrometers (Gaysin S.M., 1979; Vdovichenko V.D., 1980). The scanning of the Jupiter image in CH_4 absorption band and adjacent areas of the continuous spectrum were repeatedly carried out along both, the central meridian and equatorial zone within the wavelength range of 0.3-1.1 mcm. This allowed efficiently considering the aerosol absorption in the short wavelength region of the spectrum of the planet. The influence of aerosol absorption on the observational data of the above-mentioned authors was considered by using the results of measurement of the brightness coefficients performed by V.G. Teifel (Teifel V.G., 1980).

As a laboratory data for CH_4 λ 6190 Å, we used the results of research of Lutz B. et al., (Lutz B.L. & Owen T., 1980). Based on dependencies $\ln(Nl/\tau_s)=f(\ln(Nl))$, we calculated the monochromatic absorption coefficients in band CH_4 λ 6190 Å in the spectra of Jupiter and Saturn by using the above-described procedure (Figure 1, Table 1).

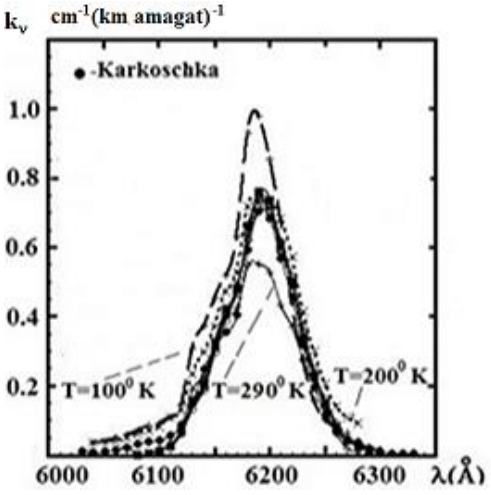

Figure 1a. Comparison of the results of calculations of monochromatic absorption coefficients for CH_4 λ 6190 Å: the squares (dark and blank) correspond to the results of observations (Gaysin S.M., 1979; Vdovichenko V.D., 1980) (the dark squares are the indicatrix of scattering according to A. Morozhenko (Morozhenko A.V., 2004), the blank squares are for the Rayleigh indicatrix of scattering in the atmosphere of Jupiter; blank circles are obtained based on the observations by Moreno (Moreno F. & Molina A., 1991;. Ortlz J.L. et al, 1992), blank rhombs are the calculations according to the observations by Karkoshka (Karkoshka E., 1994), and dark circles are the computational results (Karkoshka E., 1994). The results of laboratory measurements (Smith W.H. et al., 1990) are indicated with a dotted line.

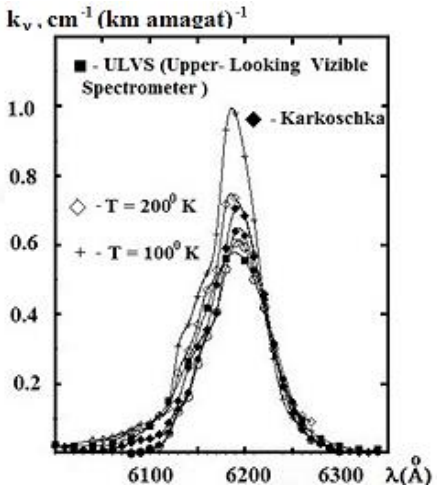

Figure 1b. Comparison of the results of calculations of monochromatic absorption coefficients for CH_4 λ 6190 Å: the squares (dark) are the data of ULVS (Upper-Looking Visible Spectrometer) (Karkoschka E. & Tomasko M.G., 2010), dark circles denote the results of observations by Woodman et al. (Voodman J.H. et al., 1979), blank circles are obtained based on the observations by Moreno (Moreno F. & Molina A., 1990, 1991; Ortlz J.L. et al, 1992), blank rhombs are the results of laboratory measurements (Smith W.H. et al, 1990) with T = 200K, and dark rhombs are the results of calculations (Karkoshka E., 1994).

Table 1. Spectral values of k_v cm^{-1} (km • amagat) $^{-1}$ to the absorption band for CH_4 *λ 6190* Å.

The values of monochromatic absorption coefficients for the methane band in the laboratory conditions given in the Table were taken from the works (Lutz B.L. et al, 1982;. *marked [1] in the Table*), and the corresponding values of k_v for planet conditions were calculated by selecting the observational data obtained in the works (Karkoshka E., 1994*[2]*; Moreno F. & Molina A., 1991*[6]*;

Ortlz J.L. et al., 1992*[7]*; Dementyev M.S. &Morozhenko A.V., 1990*[3]*; Gaysin S.M., 1979*[4]*; VdovichenkoV.D., 1980*[5]*).

λ (Å)	Lnk_ν						
	Lab. rev. [1]	*computed [2]*	*The results of calculations by the authors of the specified work about the observational data:*				
			[4,5]	*[3]*	*[6,7]*	*[2]*	
			Jupiter				Saturn
6040	-	-4.828	-	-	-	-	-
6050	-	-4.710	-	-	-	-	-
6060	-	-4,343	-	-	-	-	-
6070	-	-3.912	-	-	-	-	-
6080	-6.907	-3.506	-7.020	-6.773	-6.96	-6.904	-6.942
6090	-5.809	-3.270	-4.771	-5.711	-5.865	-5.826	-5.726
6100	-4.200	-3.194	-3.964	-4.378	-4.329	-4.290	-4.158
6110	-3.507	-2.900	-3.219	-3.624	-3.676	-3.630	-3.516
6120	-2.465	-2,430	-2.747	-2.812	-2.755	-2.687	-2.644
6130	-1.661	-1.890	-1.969	-2,056	-2.008	-1.931	-1.950
6140	-1.470	-1.406	-1.592	-1.743	-1.676	-1.638	-1.627
6150	-1.103	-1.174	-1.289	-1.269	-1.220	-1.19	-1.176
6160	-0.904	-1.036	-1.000	-0.998	-0.746	-0.925	-0.909
6170	-0.855	-0.906	-0.734	-0.714	-0.478	-0.748	-0.706
6180	-0.605	-0.524	-0.504	-0.525	-0.334	-0.475	-0.451
6190	-0.598	-0.349	-0.311	-0.341	-0.354	-0.346	-0.301
6200	-0.638	-0.381	-0.316	-0.364	-0.523	-0.370	-0.320
6210	-0.839	-0.566	-0.494	-0.536	-0.702	-0.549	-0.482
6220	-0.994	-0.783	-0.702	-0.712	-1.042	-0.731	-0.659
6230	-1.291	-1.152	-1.100	-1.087	-1.447	-1.075	-0.993
6240	-1.609	-1.640	-1.500	-1.480	-1.828	-1.480	-1.400
6250	-1.945	-2.154	-1.920	-1.904	-2.388	-2.036	-2.000
6260	-2.465	-2.688	-2.542	-2.543	-3.111	-2.731	-2.768
6270	-3.101	-3.194	-3.215	-3.210	-3.403	-4.086	-4.002
6280	-3.283	-3.650	-3.632	-3.821	-4.088	-4.840	-4.456
6290	-4.017	-4.200	-4.273	-4.548	-5.186	-5.74	-3.876
6300	-5.300	-4.710	-	-	-5.30	-6.06	-4.190
6310	-6.908	-5.298	-	-	-	-	-
6320	-	-5.521	-	-	-	-	-

The results of our calculations of lnk_ν for the absorption band of CH_4 λ6190Å, based on the observation material (Karkoshka E., 1994; Moreno F. & Molina A., 1990, 1991;. Ortlz J.L. et al, 1992; Voodman J.H. et al, 1979;. Dementyev M.S. & Morozhenko A.V., 1990) well correspond to the results of measurements (Karkoshka E., 1994; Ortlz J.L. et al, 1992).The discrepancy between the calculation results of the values of monochromatic absorption coefficients in the wings of bands of CH_4 λ 6190 Å is due to the limitation of the laboratory spectrum along the wavelength and inaccurate definition of k_ν values (Lutz B.L. et al., 1982).

The comparison of the obtained values of monochromatic absorption coefficient with the gained results (Karkoshka E., 1994; Karkoschka E. & Tomasko M.G., 2010) has proved the correctness of the application of the above-mentioned method to determine any molecular gases present in the atmospheres of the planets (see Figure 1 a and b).

NH_3 λ 6475 Å. This absorption band is the strongest in the visible region of the spectrum of Jupiter; however, ammonia also plays an important role in the formation of the infrared spectrum of Jupiter and Saturn (Guinet M. et al., 1960). The experimentally determined intensity parameter of fundamental bands is essential for the immediate calculation of monochromatic absorption coefficient and the concentration of ammonia. Therefore, the determination of these coefficients in terms of Jupiter and Saturn is of great interest.

As compared with Jupiter, the equilibrium temperature of Saturn is lower, and consequently, the pressure of the saturated vapors of ammonia decreases greatly. This phenomenon can be associated with the fact that a portion of ammonia gas on Saturn condenses, forming a crystal cover of the planet, and thus shielding the internal cloud layer of the planet, responsible for the effective gas absorption.

According to the observational data for the equatorial zone of Jupiter (Moreno F. & Molina A., 2010; Voodman J.H. et al, 1979) and Saturn (Moreno F. & Molina A., 1990), laboratory measurements (Lutz B.L. & Owen T., 1980), as well as computation results (Yanovitskij E.G., 1997; Morozhenko A.V., 2004) for absorption band NH_3 λ 6475Å, the dependence of $\ln(Nl/\tau_s)$ on $\ln(Nl)$ for these planets were drafted separately. Following the drafting of dependence $\ln(Nl/\tau_s) = f(\ln(Nl))$, the values of monochromatic absorption coefficients for NH_3 λ 6475 Å were calculated (Table 2, Fig. 2).

Table 2. Spectral values of k_v cm^{-1} $(m \bullet amagat)^{-1}$ for the absorption bands NH_3 *λ 6475* Å and *λ 5520 Å*.

The monochromatic values of monochromatic absorption coefficients in the laboratory for each ammonia band given in the Table were taken from the work (Lutz B.L. & Owen T., 1980; *marked [1] in the Table*)), and the corresponding values for planet conditions were calculated by selecting the observational data obtained in the works (Karkoshka E., 1994 [2]; Moreno F. & Molina A., 1991 [3]; Ortlz J.L. et al, 1992 [4]; Moreno F. & Molina A., 1990 [5]; Voodman J.H. et al., 1979 [6]).

λ (Å)	Ln k_v				λ (Å)	Ln k_v		
	Lab.	Jupiter		Saturn				
	[1]	*[3,4]*	*[2]*	*[5]*		*[1]*	*[2]*	*[6]*
6360	-9.903	-	-10.002	-	5460	-12.206	-11.6	-11.549
6370	-9.433	-10.435	-9.509	-10.415	5465	-10.82	-10.22	-10.213
6380	-8.805	-10.087	-8.876	-10.58	5470	-10.26	-9.63	-9.633
6390	-8.422	-9.310	-8.464	-9.255	5475	-9.433	-8.79	-8.821
6400	-8.146	-8.741	-8.098	-8.695	5480	-8.65	-8.65	-8.65
6410	-7,601	-8.193	-7.528	-8.133	5485	-8.08	-8.00	-8.00
6420	-6.908	-7.626	-6.740	-7.572	5490	-7.51	-7.37	-7.37
6430	-6.096	-6.163	-5.603	-6.124	5495	-7.21	-6.98	-6.98
6440	-5.573	-4.823	-4.573	-4.824	5500	-7.38	-7.17	-7.17
6445	-5.318	-4.260	-3.987	-4.274	5505	-7.92	-7.81	-7.81
6450	-5.613	-4.476	-4.400	-4.485	5510	-8.22	-8.14	-8.14
6460	-6.645	-6.171	-6.139	-6.127	5515	-7.60	-7.45	-7.45
6470	-5.809	-4.679	-4.570	-4.809	5520	-7.26	-7.01	-7.01
6475	-5.250	-4.216	-3.969	-5.365	5525	-7.38	-7.20	-7.21
6480	-5.485	-4.815	-4.465	-5.884	5530	-7.60	-7.46	-7.47
6490	-5.907	-5.366	-5.014	-6.223	5535	-7.82	-7.68	-7.68
6500	-6.166	-5.900	-5.470	-6.848	5540	-7.96	-7.83	-7.83
6510	-6.365	-6.353	-5.826	-7.545	5545	-8.06	-7.95	-7.95
6520	-6.709	-6.886	-6.300	-8.289	5550	-8.20	-8.12	-8.12
6530	-7.131	-7.614	-6.930	-8.810	5555	-8.39	-8.32	-8.32
6540	-7.293	-8.346	-7.163	-9.658	5560	-8.65	-8.58	-8.58
6550	-7.958	-8.859	-7.856	-11.883	5565	-8.96	-8.91	-8.91
6560	-8.422	-9.686	-8.355		5570	-9.12	-9.17	-9.17
6570	-9.567	-11.793	-9.481		5575	-9.50	-9.45	-9.45
6580	-9.903		-9.881		5580	-9.90	-9.86	-9.85
6590					5585	-10.26	-10.22	-10.22
6600					5590	-10.72	-9.53	-10.22
6610					5595	-11.33	-11.30	-11.31
6620					5600	-11.74	-11.71	-11.69

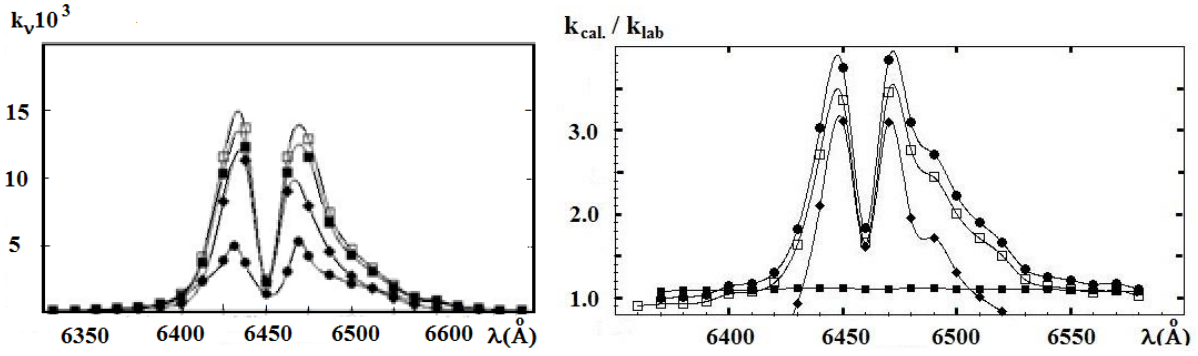

Fig. 2. Comparing the contours of monochromatic absorption coefficients k_v (cm^{-1} (km • amagat) $^{-1}$) of band NH_3 λ 6475 Å:

(Left panel) dark squares - in the conditions of Jupiter's atmosphere (based on the observational data (Karkoshka E., 1994), blank squares - in the conditions of the atmosphere of Saturn (Karkoshka E., 1994), rhombs - in the conditions of Jupiter's atmosphere (Voodman J.H. et al., 1979), dark circles - data of the work (Lutz B.L. et al, 1982) at room temperature.

(Right panel) dark rhombs denote the dependence of the ratio of the calculated and laboratory measurements of monochromatic absorption coefficients in band NH_3λ 6475 Å for Jupiter (Moreno F. & Molina A., 1991). Dark circles mare the dependence of the relationship between the calculated and laboratory measurements of monochromatic absorption coefficients in band NH_3 *λ 6475* Å for Saturn (Karkoshka E., 1994), light squares denote the same for Saturn (Moreno F. & Molina A.,

1991). Dark squares mark the relationship of the calculated monochromatic absorption coefficients of Jupiter with Saturn.

Recalculation of values k_v for the thermal regime in the atmosphere of Jupiter and Saturn was done by the cut-and-try approach of the laboratory data to the planetary atmosphere. First of all, surely, to k_v values, the laboratory data were applied (Lutz B.L. et al., 1982).The calculation results showed that in the atmospheres conditions of Jupiter and Saturn, in the far wings of NH_3 λ 6475 Å absorption band, k_v values are comparable to the laboratory measurements, while in the central zones of this band, the deviation increases even by approximately ~ 3.5 times (Fig. 2, the right panel). The obtained values of monochromatic absorption coefficient for NH_3 λ 6475Å bands are exaggerated compared with the corresponding values for the central section of the disc of Jupiter. This may have various reasons, but is mostly associated with the presence of methane absorption in NH_3 λ 6475Å band.

The spectral course of relationship between the calculated values of the monochromatic absorption coefficients and the laboratory measurements is complicated and resembles the course of absorption in band NH_3 λ 6475 Å for both planets. The right panel of Figure 2 shows that the curves describing the relation between the calculated monochromatic absorption coefficients for Jupiter and Saturn are consistent with the peculiarities of the course of absorption of NH_3 λ 6475 Å.

NH_3 λ 5520 Å. Similar calculations were done for Jupiter in the weak absorption band NH_3 λ5520Å band. According to the observations of Voodman (Voodman J.H. et al., 1979), for the equatorial region of Jupiter (as well as across the disk of Jupiter and Saturn, under the observations of E. Karkoshka (Karkoshka E., 1994)), laboratory measurements (Lutz B.L. et al., 1982), as well as computation results (Voodman J.H. et al., 1979), the dependence of ln ln(Nl/τ_s) on ln (Nl) was drafted for NH_3λ5520Å absorption band. Thereafter, the values of monochromatic absorption coefficients for NH_3λ5520Å were calculated (see. Table 2, Fig. 3).

It is clear that many parameters of the molecular gas depend on thermodynamic conditions (such as temperature and pressure), containing the given gas. However, on the other hand, some typical qualities of the gas, such as the relative changes in energy transitions responsible for the formation of the absorption band remain almost unchanged. This is confirmed by the following example: the graphs of ln (Nl/τs) = f (ln (Nl)), derived from the laboratory data for absorption bands of NH_3 λ6475Å, λ5520Å coincide the similar graphs drafted based on the calculated values for the above-mentioned absorption bands in the conditions close to Jupiter's atmospheric conditions (Figure 3).

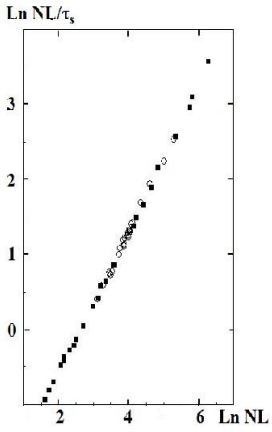

Figure 3. Dependence of (Nl/τ_s) on ln (Nl) for two absorption bands: NH_3 λ6475Å, λ5520Å

Our calculations show that graphs of dependence of ln(Nl/τ_s) on ln (Nl) for two different absorption bands of ammonia λ 5520 Å and λ 6475 Å are found almost on the same line. The discrepancy between these graphs would indicate an error in the measurement of monochromatic absorption coefficients. Unfortunately, the experimental data of monochromatic absorption coefficients for ammonia are very scarce compared to those for methane. Therefore, the determination of these coefficients for the thermal regime of Jupiter and Saturn can be considered an important step in the description of the real structure of the atmospheres of these planets (Fig. 4).

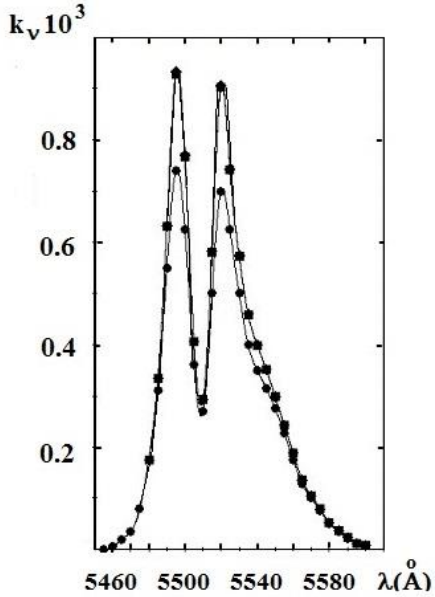

Fig. 4. The calculated values of monochromatic absorption coefficients (cm^{-1} (km•amagat) $^{-1}$) in NH_3 λ5520 Å band. Dark squares mark the data for Jupiter (Karkoshka E., 1994), light squares denote the observational data (Voodman J.H. et al., 1979), dark circles mark the data for Saturn (Karkoshka E., 1994).

We would note that for absorption band NH_3 λ 5520 Å, the values of the ratios between the calculated monochromatic absorption coefficients k_ν and the laboratory measurements for different observational data are identical. In addition, a slight methane absorption in the short-wave wing of NH_3 λ5520Å does not completely overlap this spectrum, unlike absorption band NH_3 λ 6475Å, where the significant methane absorption complicates the accurate determination of monochromatic absorption coefficient values in the observed spectrum of the planet. On the basis of the calculations (Morozhenko A.V., 2009), we tried to determine the value of γ' for NH_3 λ5520Å band. The calculations showed that the value of γ' is not constant and varies with to the depth of the atmosphere of Jupiter and Saturn.

It would be interesting to use the redefined values of k_ν to calculate the relative concentrations of absorbing gas n_g and aerosol particles n_a for bands CH_4 λ 6190 Å and NH_3 λ6475Å (Fig. 5). As Figure 5a shows, the nature of variation of concentration of NH_3 gases evidences that ammonia clouds are formed in the deeper layers than methane clouds and are more sensitive to temperature changes.

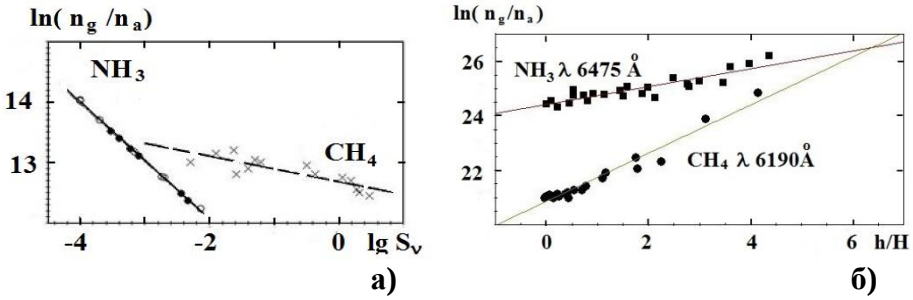

Fig. 5. Dependence of the relative concentration of aerosol lg (n_g/n_a) on absorption coefficient of lg S_ν (a) and h/H (b).

Where *H* is the height of the homogeneous atmosphere for the given kind of gas, and *h* is the provisional height. A more sloping form of the straight line for NH_3 is resulted from an increase in the gas phase in the deeper layers of Jupiter (Figure 5b). Since the methane concentration in the studied heights varies within a relatively small range, a larger slope of the line for CH_4 may be the result of the sharp decrease of the aerosol contribution with increasing penetration depth in the denser layers of the atmosphere of Jupiter.

4. Conclusion

A.V. Morozhenko calculated the values of k_ν on the basis of the observed material of E.Karkoshka (Karkoshka E., 1994) for the Rayleigh scattering. As for us, we calculated the values of k_ν for different scattering indicatrix (as well as for two-term indicatrix (Morozhenko A.V., 2004)) based on the observational data (Karkoshka E., 1994; Moreno F. & Molina A., 1990, 1991; Ortlz J.L. et al. 1992; Voodman J.H. et al, 1979; Dementyev M.S. & Morozhenko A.V., 1990; Gaysin S.M., 1979; Vdovichenko V.D., 1980). When using the values of τ_{eff} taken from the work (Avramchuk V.V. et al., 1977), the results of calculation of monochromatic absorption coefficients differ from one another (Morozhenko A.V., 2002, 2003, 2006; Morozhenko A.V. & Ovsak, A.S., 2009). For the calculations, we used the values τ_{eff}, calculated in the work (Yanovitskij E.G., 1997). In addition, the calculation of monochromatic absorption coefficient in the works (Morozhenko A.V., 2002, 2003, 2006; Morozhenko A.V. & Ovsak A.S., 2009) were based on the laboratory measurements of L.P.Giver (Giver L.P., 1978), on the laboratory measurements by (Lutz B.L. et al, 1982;. Lutz B.L. & Owen T., 1980) in the present work.

In our case, the knowledge of the pressure and temperature data in the atmospheres of the planets is not needed. The reliability of the solution to this problem depends on the accurate determination of the absorption coefficients of the laboratory and observed spectra of a planet.

This method can be used to determine the monochromatic absorption coefficients for any molecular gas in the atmospheres of other planets - Uranus and Neptune.

References

Atai A.A., Astronomichesky Jurnal Azerbaijana, 2009, № 1-2., 31. (in Russian)
Avramchuk V.V., Bugaenko L.A., Morozhenko A.V., Yanovitskij E.G., Astrometriya I astrofizika,1977, N31,54. (in Russian)
Bauer A., Goden M., Carlier J., Ma Q., and Tipping R.H., 1993, J. Quant. Spectrosc. Radiat. Transfer, 50, 463.
Chou M.D., Arking A., J. Atmos. Sci., 1980, 37, 855.
Dementyev M.S. and Morozhenko A.V.,Astron. vestnik, 1990, 24, 275.(in Russian)
Gaysin S.M., Atmosferi Yupitera I Saturna (Sb. statey), Izd-vo“Nauka”Kazakhskoy SSR, Alma-Ata, 1979, 35, 45. (in Russian)

Giver L.P., J. Quant. Spectrosc. Radiat. Transfer, 1978, 19, 311.
Guinet M., Jeseck P., Mondelain D., J. Quant. Spectrosc. Radiat. Transfer, 2011, 112, 1950.
Karkoschka E., Icarus, 1998, 133, 134.
Karkoschka E., Tomasko M.G., Icarus, 2010, 205, 674.
Karkoschka E., Tomasko M.G., Icarus,1992, 97,161.
Karkoshka E., Icarus, 1994, 111, 174.
Keffer Ch.E., Conner Ch.P. and Smith W.H., J.Quant. Spectrosc. Radiat. Transfer, 1986, 35, 487.
Keffer Ch.E., Conner Ch.P. and Smith W.H., J.Quant. Spectrosc. Radiat. Transfer, 1986a, 35, 495.
Lutz B.L., Owen T., Astrophys J., 1980, 235, 285.
Lutz B.L., Owen T., Cess R.D., Astrophys J., 1982, 258, 886.
Lyulin O.M., Perevalov V.I., MorinoI., J. Quant. Spectrosc. Radiat. Transfer, 2011, 112,531.
Mickelson M.E., Larson L.E., Schubert A.,J.Geophys.Res., 1991,96, 17507.
Moreno F. and Molina A., Astron. Astrophys., 1990, 230, 479.
Moreno F., and Molina A., Astron. Astrophys., 1991, 241, 243.
Morozhenko A.V., Tecniques and results of remote sensing of the planetary atmospheres ("Scientific book" project), Kyiv, Naukova Dumka, 2004.
Morozhenko A.V., Kinematika i fizika nebesnix tel, 2002, 18, 376. (in Russian)
Morozhenko A.V., Kinematika i fizika nebesnix tel, 2003, 19, 483. (in Russian)
Morozhenko A.V., Kinematika i fizika nebesnix tel, 2006, 22, 138. (in Russian)
Morozhenko A.V., Kinematika i fizika nebesnix tel, 2009, 25, 259.(in Russian)
Morozhenko A.V., OvsakA.S., Kinematika i fizika nebesnix tel, 2009, 25, 243. (in Russian)
Ortlz J.L.,Moreno F., and Molina A., Astron. Astrophys., 1992, 260, 465.
Ragent B., Colburn D.S., Rages K.A., J.Geophys. Res., 1998, 103, 22891.
Ramaprasad K.R., Caldwell J. and McClure D.S., Icarus, 1978, 35, 400.
Shi G. Zhang, J. Quant. Spectrosc. Radiat. Transfer, 2007, 105,459.
Smith W.H., Conner Ch. P., Baines K. H., Icarus, 1990, 85, 58.
Teifel V.G., Opticheskiye svoystva atmosfer Yupitera i Saturna, Doctor thesis, Alma-Ata, 1980. (in Russian)
Tomasko M.G., Bezard B., DooseL., EngelS., Karkoshka E., Planetary and Space Science, 2008, 56, 624.
Vdovichenko V.D., Uzkopolosnaya absolyutnaya spektrofotometriya Yupitera v λλ 0.6-1.1 μM, PhD thesis, Alma-Ata, 1980. (in Russian)
Voodman J.H., Cochran W.D. and Slavsky D.B., Icarus, 1979, 37, 73.
Yanovitskij E.G., Kinematika i fizika nebesnix tel, 1997, 13, 18.(in Russian)

Astronomy & Astrophysics (Caucasus) 2, (2016) (17-24)

Anticorrelation between changes of Hα spectral line FWHM and Doppler velocities

D. Khutsishvili [1,2,3], T. Zaqarashvili[1,2], E. Khutsishvili[2], T. Kvernadze[2], V. Kulijanishvili[2]
V. Kakhiani[2], M. Sikharulidze[2]

1. Space Research Institute of Austrian Academy of Sciences, Schmiedlstrasse 6, 8042 Graz, Austria
2. E. Kharadze Abastumani Astrophysical Observatory at the Ilia State University, 3/5 Cholokashvili str., 0162 Tbilisi, Georgia
3. Ivane Javakhishvili Tbilisi State University (TSU), 3 Chavchavadze Ave., Tbilisi 0179, Georgia.

Email: daviti.khutsishvili@gmail.com

Received November 2, 2016; revised December 8, 2016

Abstract: From September the 25th, 2012 through October 17, 18 and 19, 2012, new series of Hα spicule spectrograms for 7,500 km heights in the solar chromosphere were obtained by using a 53-cm large non-eclipsing coronagraph of Abastumani Astrophysical Observatory (Georgia). Spectrograms in Hα line were obtained in a second series of the spectrograph, where reversed dispersion equaled to 0.96 Å/mm. Doppler velocities and half-widths of 10 spicules were measured with the cadence of 4.5 sec and standard error equals to ±0.3 km/sec and 0.03 Å. Life times of almost all measured spicules were 12-16 min. Therefore, they resemble the type I spicules.To study and find periodical changes of Hα FWHM, we used the Lomb periodogram algorithm for unevenly distributed time series. We also processed Doppler velocities using the same algorithm for the same spicules in the same images. The confidence levels for our data equaled to 9.0 for 95% and 10.7 for 99% in power units. The periods are mostly above 2 min (> 180 sec). Most periods fall between 5-9 min (300-540 sec). In order to see the possible relations between the changes of Hα FWHM and Doppler velocities, we performed Low Pass FFT Filtering with different cut-off frequencies: 60 sec (0.016 Hz), 100 sec (0.01 Hz) and 200 sec (0.005 Hz). All 10 spicules show clearly anticorreleation properties, especially for the longest periodical changes.

Key words: Spicules, spectral lines, chromosphere, Doppler velocities.

1. Observations and Data Processing

The observations of chromospheric spicules were performed by using a 53-cm Lyot coronagraph of Abastumani Astrophysical Observatory (Georgia) equipped with a high dispersion grating spectrograph (0.96 Å/mm in the second order near 6000 Å) and Apogee CCD U9000 (pixel array: 3056 x 3056; pixel size: 12 x 12 μm; CCD size: 36.7 x 36.7 mm) from September the 25th, 2012 through October 17, 18 and 19, 2012.

The main lens of the coronagraph (D = 530 mm, F = 8000 mm, with focal scale of 16 arcsec/mm) was combined with two achromatic lenses system, and a field lens projects a magnified image of the sun (with diameter of 125 mm) in the coudé focus with the equivalent focal length of 13 m.

The *Ebert*-Fastie system spectrograph is equipped with a 230 x 250 mm and 600 lines/mm grating and has the highest concentration in the spectral range of 4000-6000 Å in the second order. The spectrograph has a circular slit concentric to the solar limb with its diameter slightly exceeding diameter of the limb, and is extended to about 60º of the solar limb arc, while the current CCD U9000 image covers only 20º arc of the limb.

The special complex light filter is used to get the Hα spectral lines of the spicules from the second order and the 4371 Å reference spectral line of solar photosphere from the third order of the spectrograph on the same CCD image (Nikolsky, 1970). The complex light filter consists of two different light filters attached side by side: (i) the narrow Hα filter passing through the second order spectral images of spicules only and blocking all other orders, and (ii) the blue light filter passing through the third order spectral lines of the solar photosphere only and blocking all other spectral orders.

The typical Hα spectral images of the spicules are shown in Figure 1 indicating some of the selected spicules for measurements and data processing.

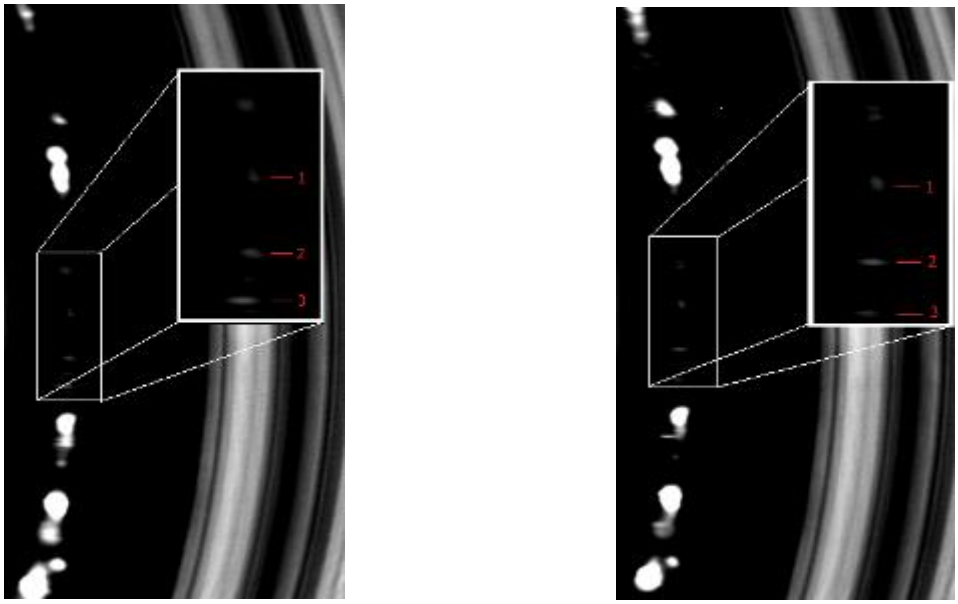

Figure 1. Typical CCD spectral images of the spicules taken on October 18, 2012 at 05:55:15 UT (left) and 05:57:02 UT (right). The images are centered on the solar equator and covers $\pm 10^0$ of the solar latitudes in the vertical direction of the images. The spectral dispersion with the scale of 0.96 Å/mm is oriented along the horizontal axis of the image. The Hα spectral images of the spicules are seen on the left side and the third order reference spectral lines of the solar photosphere are seen on the right side of each CCD image. The area containing the selected spicules for measurements is zoomed separately.

The spectrograph slit was located above the solar limb on the linear distance of about 7,500 km. The exposure time of each image equals 0.3 sec. The images were captured in the series with a cadence of about 4.5 sec between the images mainly limited by the CCD data readout speed. The duration of each series is about 17-19 min. The observation series were carried out by us on the east side of the solar limb within ±10 degree of the latitude interval from the solar equator.

Special attention was paid to the selection of the spicules for further measurements. Consequently, we selected 10 spicules, which were well-isolated and reliably identified during each whole series.

We used an updated version of original astronomical image processing software AImaP 3.59 to reduce the observational data series. In addition to the standard CCD image processing, the software allows manually selecting a row of a CCD image and approximating 1D Gaussian profiles of Hα spectral line of a spicule and a reference spectral line and transforming a distance between their centroids into a Doppler velocity of a spicule. Simultaneously, the software calculates FWHM of Hα spectral line by using the same Gaussian profile.

The measurements were done for each selected spicule in every image of each series. As a result, we obtained the time series of Doppler velocities and the corresponding FWHM of Hα spectral line of a spicule.

To estimate the accuracy of a Doppler velocity and Hα spectral line FWHM measurements, we applied the high pass FFT filtering with the cutoff frequency equaling to 0.016 Hz (60 sec in periods) to the obtained time series and calculated the standard deviations of the filtered data which, equal the following values: ±0.3 km/sec for Doppler velocities and ±0.03 Å for FWHM.

3. Data Analysis

a. Periodical changes of Hα spectral line FWHM (Full Width Half Maximum)

To study and find periodical changes of Hα FWHM and compare them to the changes of the Doppler velocities, we used the Lomb periodogram algorithm (Press et al., 1992) for the unevenly distributed time series.

Table 1 shows the frequencies we found. The confidence levels for our data equal to 9.0 for 95% and 10.7 for 99% in power units. So, almost all frequencies given in the Table are above the confidence levels.

Table 1. Periodical changes of Doppler Velocities and Hα FWHM of the spicules

	Hα FWHM			Doppler Velocities		
Spicule #	Frequency, Hz	Period, sec	Power	Frequency, Hz	Period, sec	Power
17-10-12 #1	0.00198	505	14.4	0.00187	535	49.9
17-10-12 #6	0.00177	564	40.3	0.00163	613	37.5
18-10-12 #1	0.00520	192	17.1	0.00223 0.00594	449 168	21.2 15.3
18-10-12 #2	0.00174	574	20.7	0.00174 0.00267	574 375	34.7 23.9
18-10-12 #3	0.00377	265	20.7	0.00377	265	22.0
18-10-12 #6	0.00142 0.00299	704 334	22.9 30.5	0.00135 0.00327	740 305	17.7 26.6
19-10-12 #5	0.00871	115	25.5	0.00256 0.00511	390 196	43.4 9.5
25-09-12 #1	0.00332	301	14.8	0.00318	314	24.5
25-09-12 #4	0.00143 0.00368	699 272	5.1 7.9	0.00163 0.00388	614 258	38.7 12.6
25-09-12 #5	0.00274	365	25.1	0.00286	350	37.1

As we can see from these results as well as from the Figures below, Hα FWHM shows quite similar periodical changes and the periods are mostly above 3 min (> 180 sec). Most periods fall between 4-9 min (240-540 sec).

b. Anticorrelation between the changes of Hα spectral line FWHM and Doppler velocities

In order to see the possible relations between the changes of Hα FWHM and Doppler velocities, we performed Low Pass FFT Filtering with different cut-off frequencies: 60 sec (0.016 Hz), 100 sec (0.01 Hz) and 200 sec (0.005 Hz).

The images in Figure 2 show 4 stacked drawings of the raw and filtered data with corresponding cut-off frequencies. All 10 spicules demonstrate clearly anticorreleation properties, especially for the longest periodical changes.

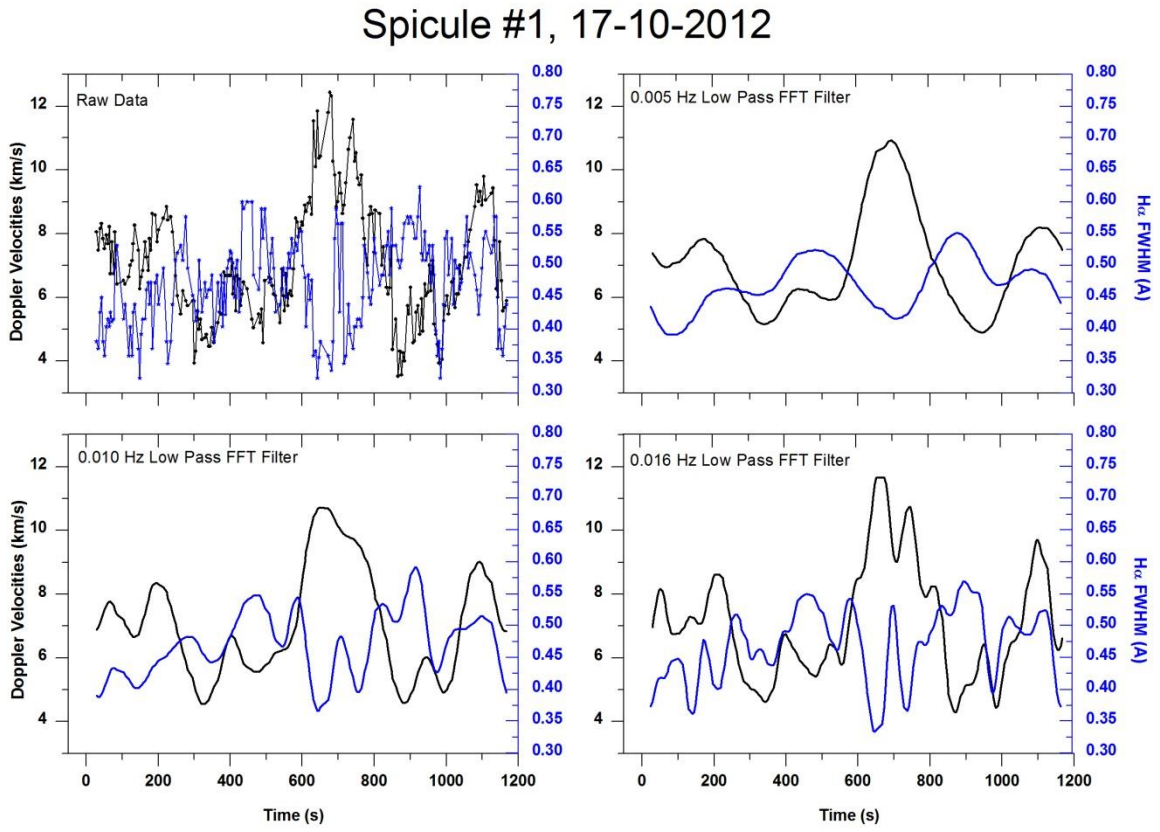

Fig. 2. Anticorrelation between the changes of Hα spectral line FWHM and Doppler velocities

Spicule #1, 18-10-2012

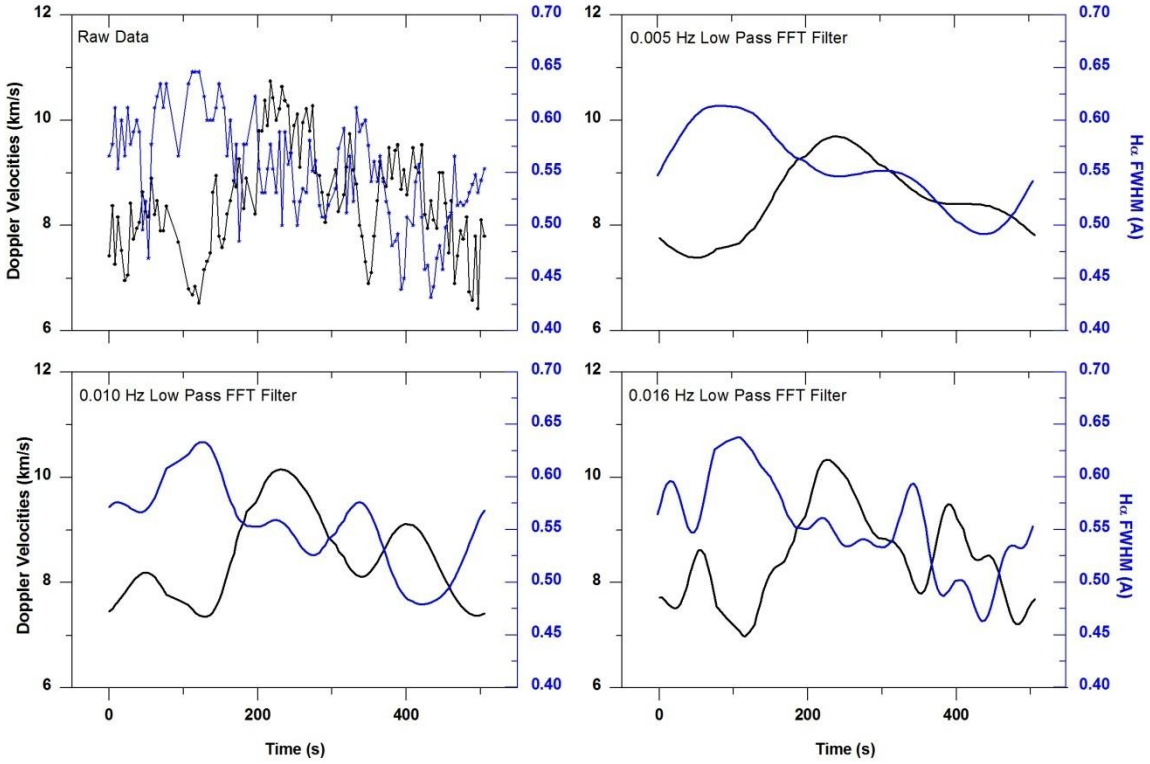

Spicule #2, 18-10-2012

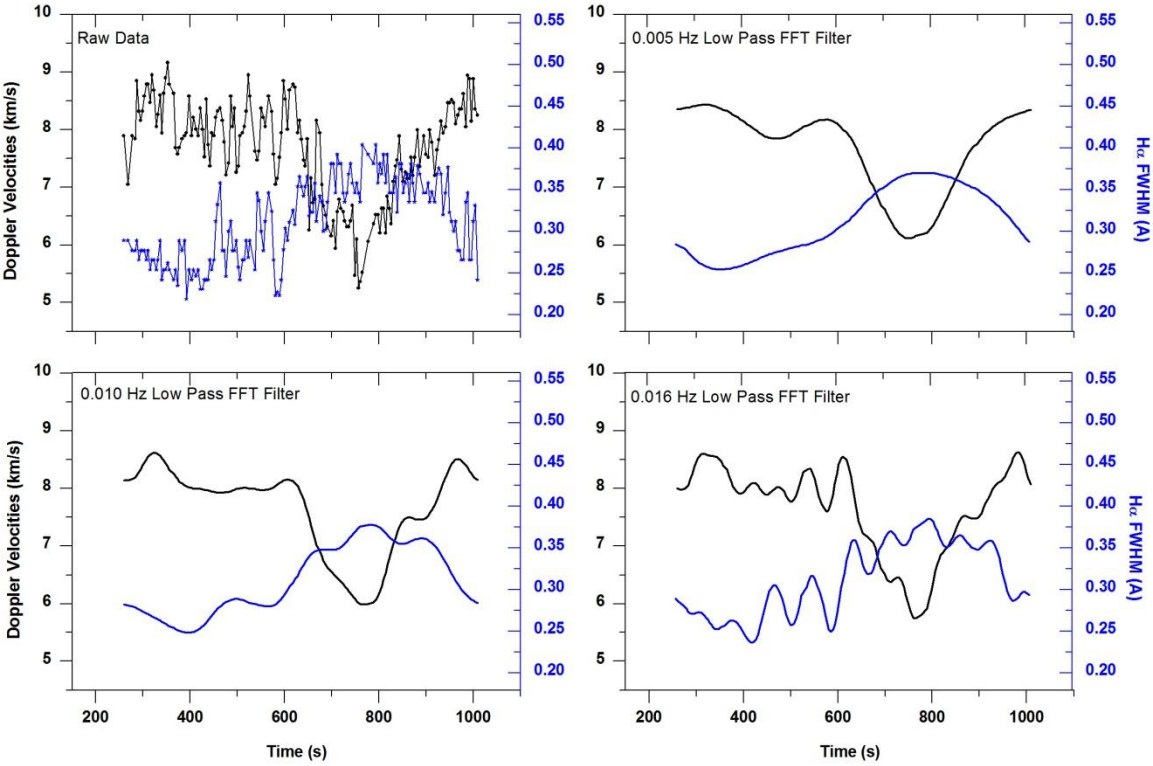

Spicule #6, 18-10-2012

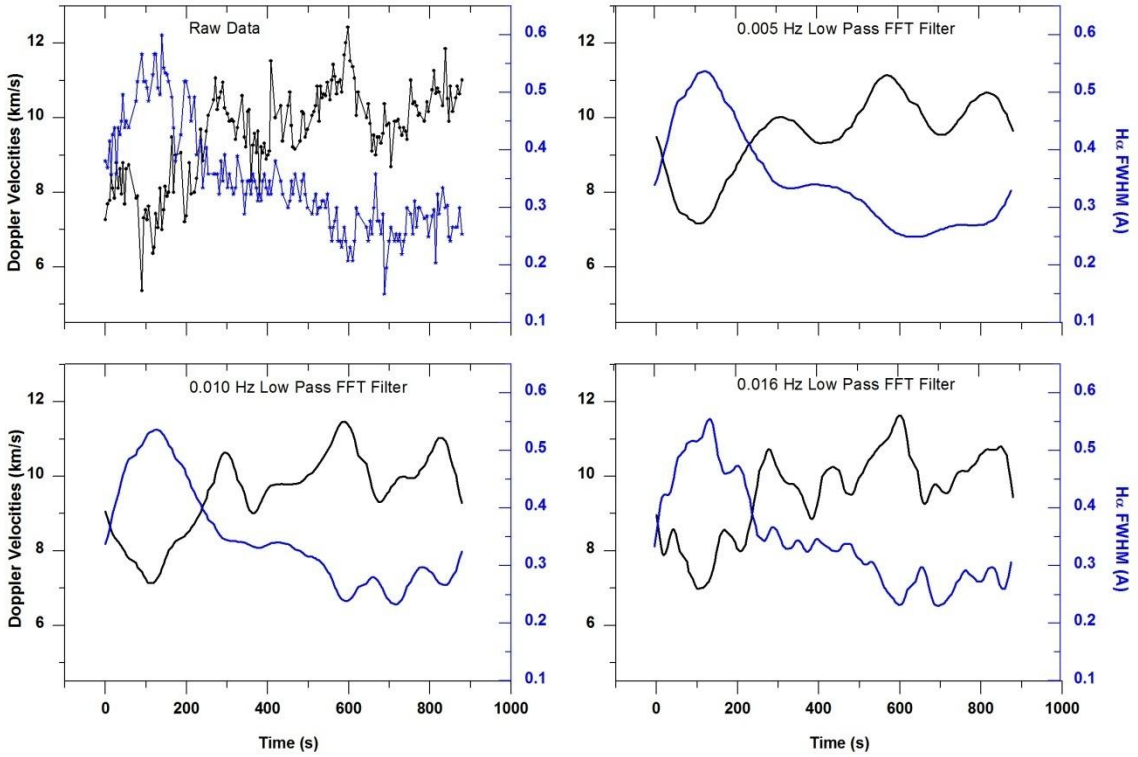

Spicule #3, 18-10-2012

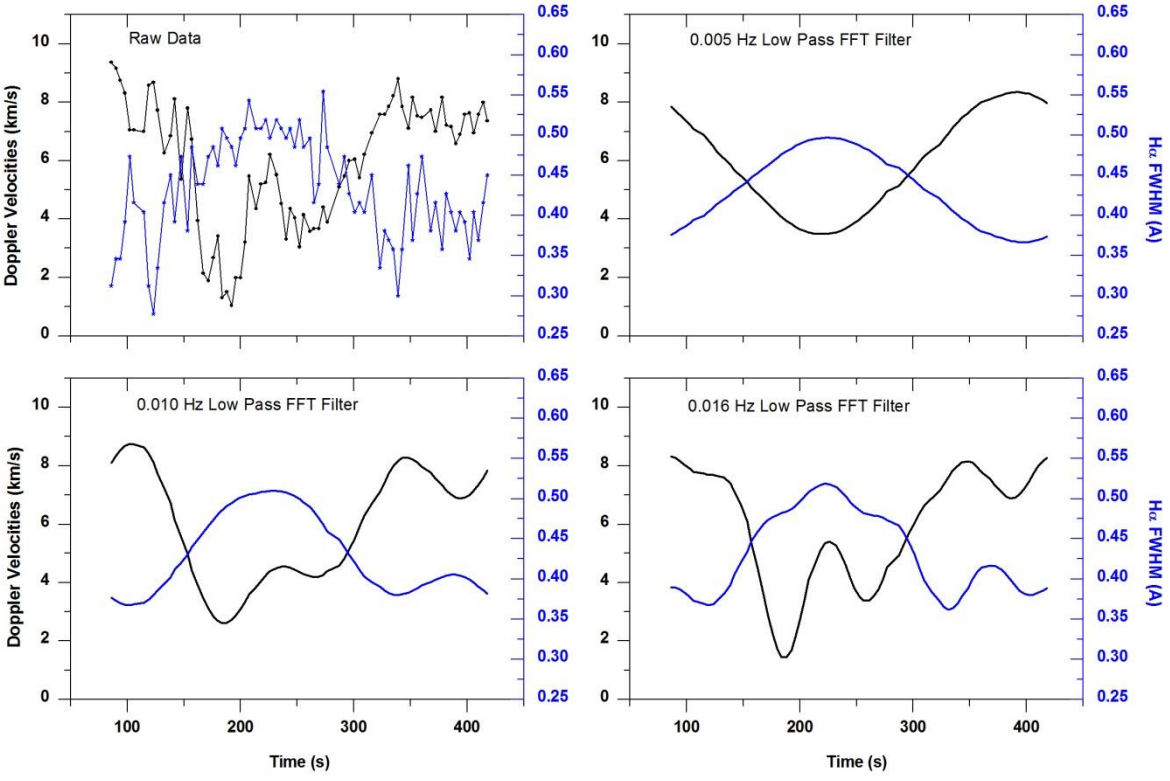

Spicule #5, 19-10-2012

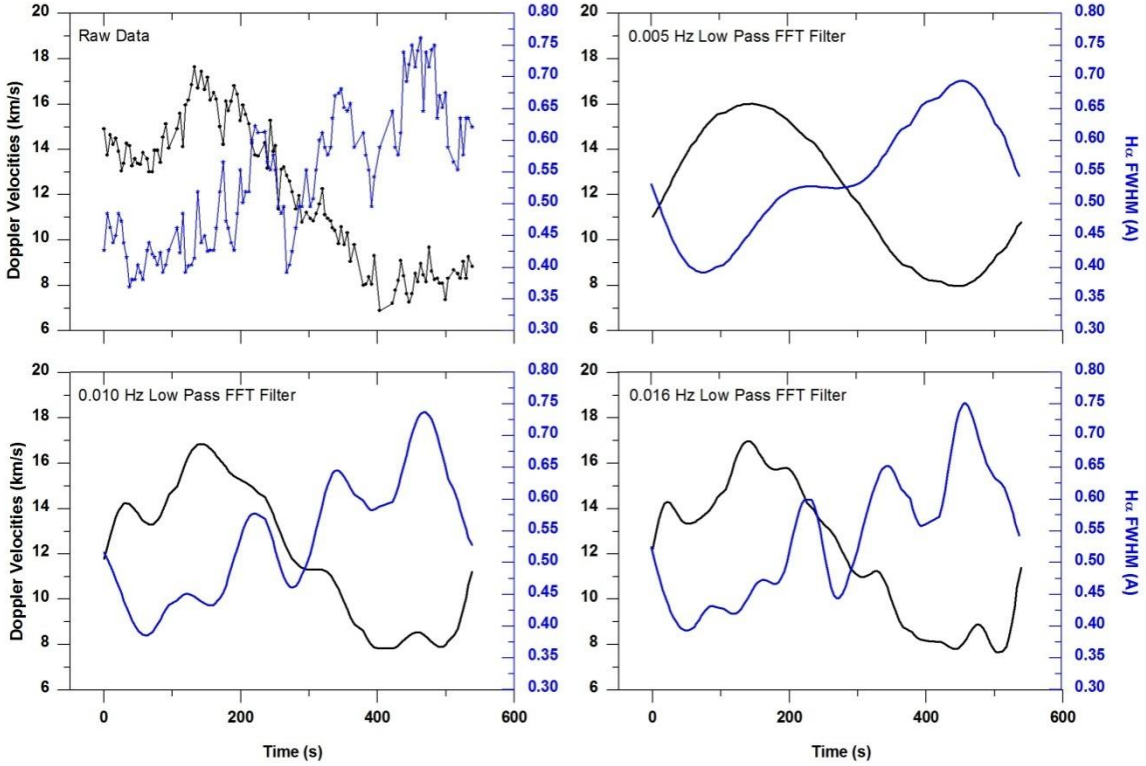

Spicule #1, 25-09-2012

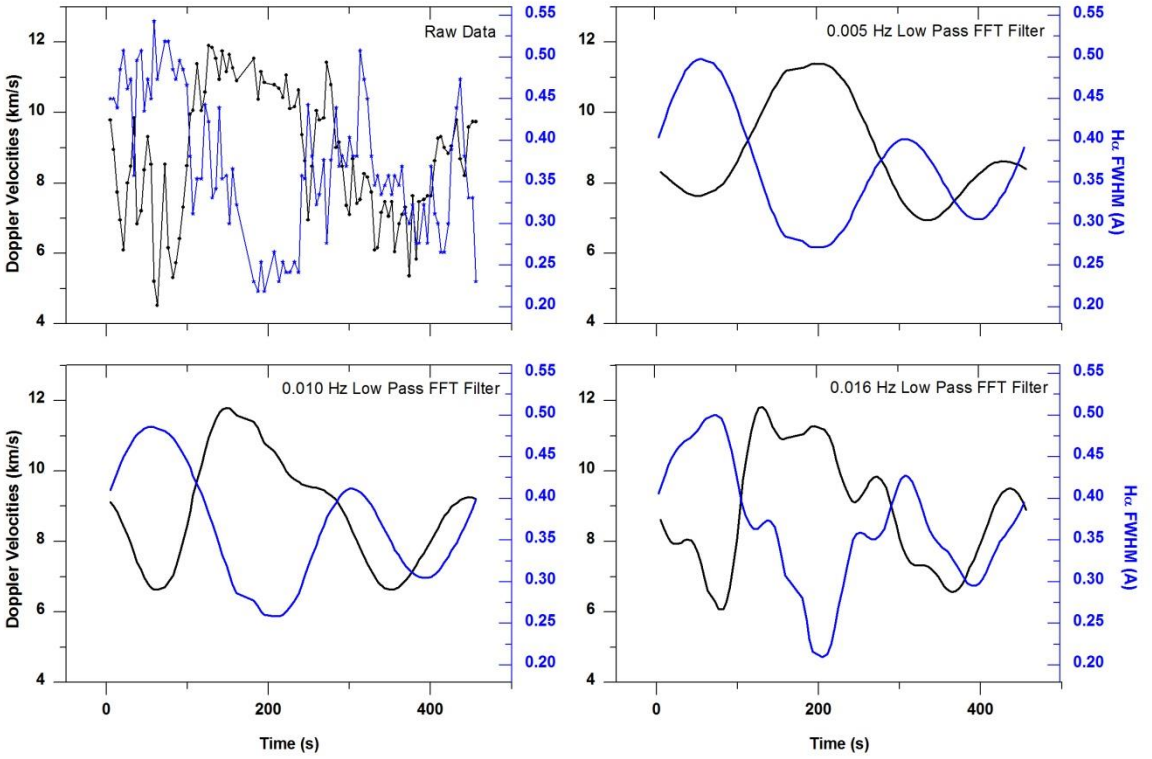

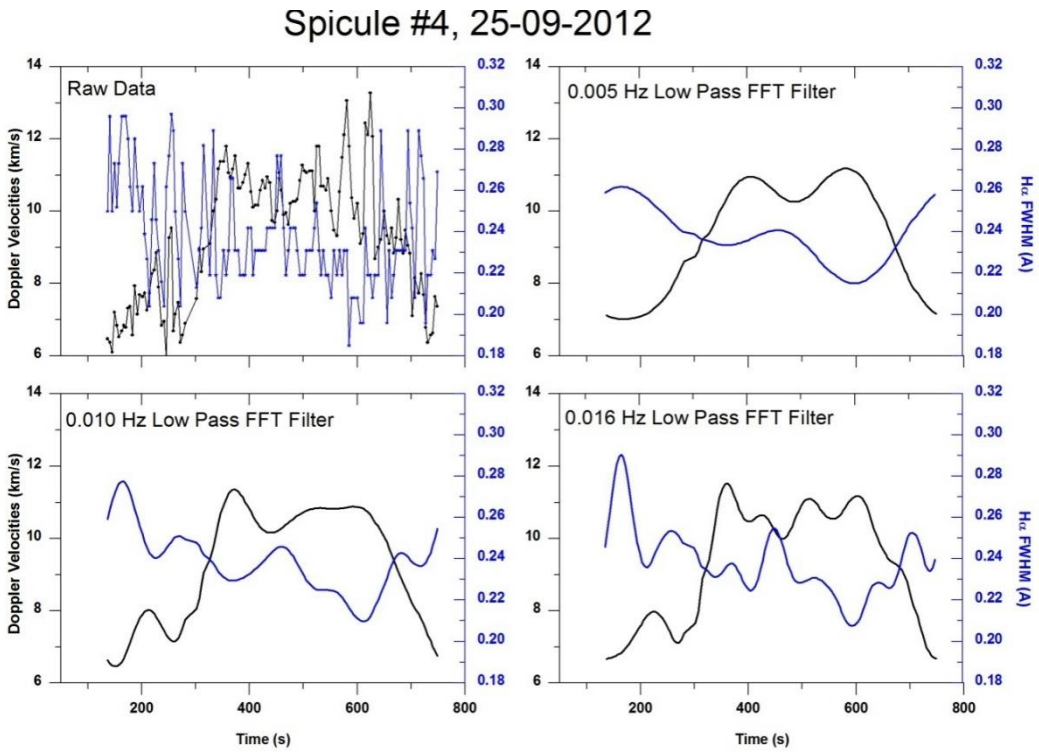

Acknowledgements: The work is supported by the Shota Rustaveli National Science Foundation grants FR/417/6-310/13 and DO/202/6-310/14.

References

H. Saleem, J. Vranjes, and S. Poedts, A&A, 2007, 471, 289-293
Kulijanishvili, V. I. & Zhugzhda, Iu. D., 1983, On the problem of spicular oscillations, Sol. Phys., 88, 35
De Pontieu, B., Erdelyi, R., & de Wijn, A. G., 2003, Intensity Oscillations in the Upper Transition Region above Active Region Plage, ApJ, 595, L63
Xia, L. D., Popescu, M. D., Doyle, J. G., &Giannikakis, J., 2005, Time series study of EUV spicules observed by SUMER/SoHO, A&A, 438, 1115
De Pontieu, Bart; Erdélyi, Robert; James, Stewart P., 2004, Natur., 430, 536D
De Pontieu B., et al., Science 318, 1574 (2007a).
De Pontieu B., et al., PASJ 59, S655 (2007b).
R. Erdelyi, V. Fedun, Science 318, 1572 (2007).
Ajabshirizadeh A., Tavabi E., Koutchmy S., 2008, New Astronomy, 13, 93
Zaqarashvili, T. V. and Skhirtladze, N., ApJ, 2008, 683, L91
Zaqarashvili, T.V.; Erdelvi, R.; 2009, Space Science Reviews, Volume 149, Issue 1-4, pp. 355-388
Murawski, K. and Zaqarashvili, T. V., 2010, Astron. Astrophys., 519, 8
Murawski, K., Srivastava, A. K., and Zaqarashvili, T. V., 2011, Astron. Astrophys., 535, A58, 9
Ebadi, H., Zaqarashvili, T. V. and Zhelyazkov, I., 2012, Astroph. Space Sci., 337, 33
Kukhianidze, V. T., Zaqarashvili, T. V., Khutsishvili, E. V. 2006, A&A, 449, L35-L38.
Zaqarashvili T.V., Khutsishvili E. V., KukhianidzeV. T., Ramishvili K, G., 2007, Astron. Astrophysics 474, 627.
Kulijanishvili V. I.: 1980, Dynamics of the spicules accoroting to spectral observations at various heights of the solar chromosphere, Solar phys., 66, 251-258
V.I. Kulijanishvili, G.M. Nikolsky, 1978, Solar Physics 59, 21
V.I. Kulijanishvili, Y.D. Zhugzhda, 1983 Solar Physics 88, 35
Khutsishvili, E. V. 1986, Sol. Phys., 106, 75.
Pereira, T. M. D., De Pontieu, B. and Carlsson, M., 2012, ApJ, 759, 18
Pereira, T. M. D., De Pontieu, B. and Carlsson, M., 2013, ApJ, 764, 69
Sekse, D. H., Rouppe van der Voort, L., and De Pontieu, B. and Scullion, E., 2013b, ApJ, 769, 44
Zhang, Y. Z., Shibata, K., Wang, J. X., Mao, X. J., Matsumoto, T., Liu, Y., and Su, J. T., 2012, ApJ, 750, 9
Yeon-Han Kim, Su-Chan Bong, Young-Deuk Park, Kyung-Suk, 2008, Journal of The Korean Astronomical Society, 41, 173
Judge, P. G., Tritschler, A., &Chye Low, B. 2011, ApJ, 730, L4
Leenaarts, J., Carlsson, M., & van der Voort, L. R. 2012, The Astrophysical Journal, 749, 136
E. Khutshishvili, V. Kulijanishvili, T. Kvernadze, T.V. Zaqarashvili, V. Kakhiani, D. Khutsishvili, M. Sikharulidze., 2014, Astrophysics and Space Science, 354, 259-266

Astronomy & Astrophysics (Caucasus) 2, (2016) (25-40)

WR and LBV stars

N. Kochiashvili[1,2], S. Beradze[1], I. Kochiashvili[1], R. Natsvlishvili[1], M.Vardosanidze[1,2]

1.E. KharadzeAbastumani Astrophysical Observatory at the Ilia State University, 3/5 Cholokashvili str., 0162 Tbilisi, Georgia
2. Samtskhe-Javakheti State University, Akhaltsike, Rustaveli Street #106, Georgia

Email: nino.kochiashvili@iliauni.edu.ge

Abstract

Evolutionary scenarios of massive stars were revised in recent decades, after finding "unusual", blue progenitor of SN 1987A and after detecting the more massive stars than the accepted 120 $M_{\odot}$ maximum limit of stellar masses. A very important relation exists between WR and LBV stars. They represent the earlier, pre-SN evolutionary states of massive stars. WR and LBV stars and "classic" evolutionary scheme of the relation between the different type massive stars are discussed in this article. There also exist the newest evolutionary scenarios for low metallicity massive stars, which give us a different picture of their post main-sequence evolution. There is a rather good tradition of observations and investigations of massive stars at Abastumani Astrophysical Observatory. The authors discuss the new findings on the fate of P Cygni, the LBV star. These results on the reddening of the star and about its next possible outburst in the near future were obtained on the basis of UBV long-term electrophotometric observations of P Cygni by Eugene Kharadze and Nino Magalashvili. The observations were held in 1951-1983 at Abastumani Observatory using 33-cm and 48-cm reflectors.

Key Words: massive stars, WRs, LBVs, evolution of massive stars, P Cygni, electrophotometric observations.

1. Introduction

Although a great majority of massive stars are prominent objects in the sky and in fact, the history of investigation of variable stars begins from so called "great eruptions" of the most known representatives of them – P Cygni and η Carinae, there has been a great deal of unsolved problems in this field until the latest decades. Astronomy is a fast-evolving branch of science what is particularly true for the last decades. Usually, very significant new discoveries are made on the basis of new, unexpected observational findings.

The investigation of all types of massive stars, especially of those, which are on the short-term transitional stage of evolution, is accomplished very intensely at preesnt. On the basis of the observations of massive stars, we can trace the evolution of galaxies throughout the whole history of the universe (Haiman and Loeb, 1997). A particular interest in the studies of massive stars has been seen since the explosion of so called type II supernova of SN 1987A. This event proved that indeed, the core collapse of a massive star causes a supernova event, but it was found that for this supernova, the "ancestor" star was the blue supergiant and not red one, as it was considered before. Not only red supergiants explode as supernovae, but sometimes blue ones as well.

Therefore, following this event, the theory of evolution of massive stars was revised. Especially interesting are the objects that are in the short-lived transitional phase of evolution and the so-called "supernova impostors" and also the objects the "real" supernovae may have a connection with. These are massive supergiant and hypergiant stars and so-called Luminous Blue Variables (or LBVs).

The following issue is the discussion of the described evolutionary process. Although all of the details are yet to workout, the story of how Type Ib, Type Ic, and Type II supernovae are produced is getting clearer. The three types are all closely related and all involve the collapse of a massive, evolved stellar core. Hence, collectively, Types Ib, Ic, and II are known as core-collapse supernovae (Carrol, Ostlie, 2007).

The next unexpected finding was the mass of one of the Wolf-Rayet (WR) stars - R136a1, in the star-forming region of Tarantula in the Large Magellanic Cloud. The mass of the star much more exceeds the upper “classic” stellar mass limit of 120 $M_{\odot}$. According the all new data, the value of its mass is approximately 290-300 $M_{\odot}$ (see for example Crowther, et al., 2010).

Now we are going to give a brief overview of above-mentioned WR and LBV stars.

2. Wolf-Rayet Stars

Wolf-Rayet stars are extremely massive stars. The first WRs were discovered by C. J. E. Wolf and G. Rayet while working at Paris Observatory in 1867. Using a visual-wavelength spectrometer to conduct a survey of stars in Cygnus, they observed three stars all within one degree of each other that exhibited unusually strong, very broad emission lines, rather than the absorption lines usually seen in other stars. Today, more than 220 WR stars are identified in the Milky Way Galaxy, although the total number of WRs in the Galaxy is estimated to be between 1000 and 2000 (Crowther, 2008). Wolf-Rayet (WR) stars are Population I stars, with luminosities of up to10^6 $L_{\odot}$, and effective temperatures of 30 000 K and higher, lying just above the upper main sequence in the H-R diagram. They are notable for their peculiar spectra, which combine the absorption lines of an OB star with strong, broad, high-ionization C, N, O, and He emission. They have been divided into three spectroscopic groups: the WC stars, sub-classified WC4-WC9, with strong C and O emission, and the WN stars, subclassified WN2-WN9, with strong N and He emission (Figure 1; Figure 2); there are a few which are classified as WO – with strong O emission. Although they are very rare, they play an important role in the chemical evolution of galaxies because of their very high mass loss. Because of their high luminosities and bright emission lines, WR stars are easily identified, even in relatively distant galaxies, so they are a useful tool to study the stellar and chemical evolution in a variety of galactic environments (Percy, 2007).

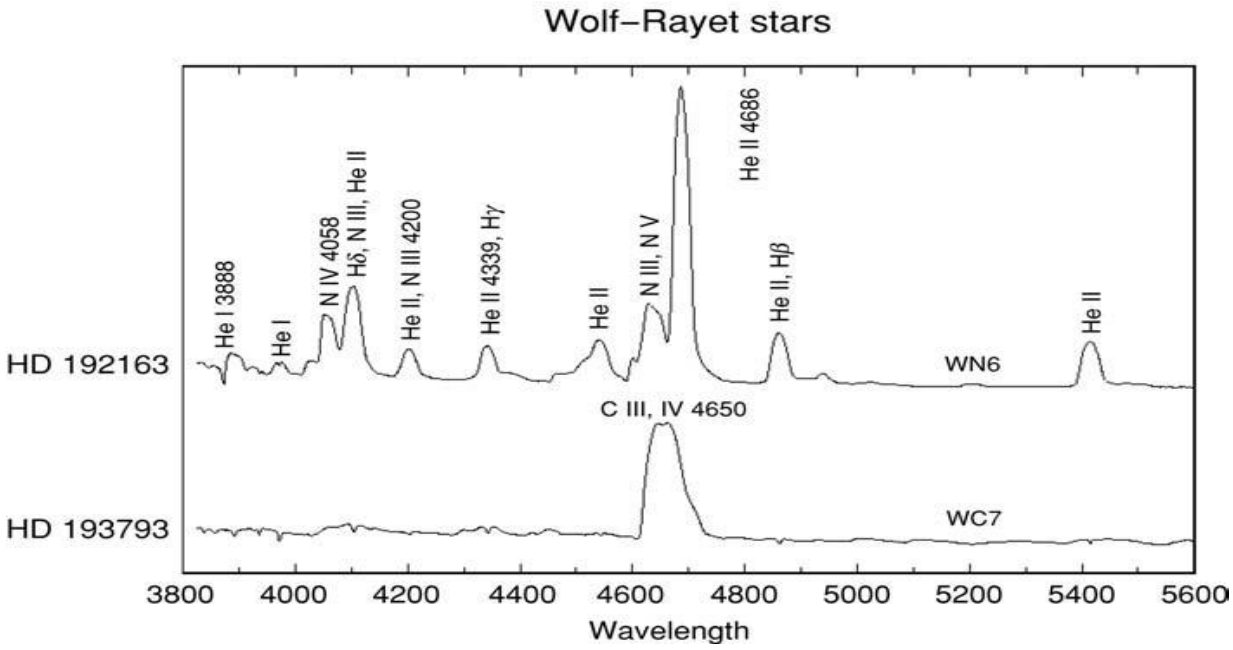

Figure 1. Spectra of two WR stars: HD 192163, which is of a WN type, and HD 193793, which is of a WC type. Note the dominance of the emission lines in each case.
(From Richard O. Gray, Percy, 2007)

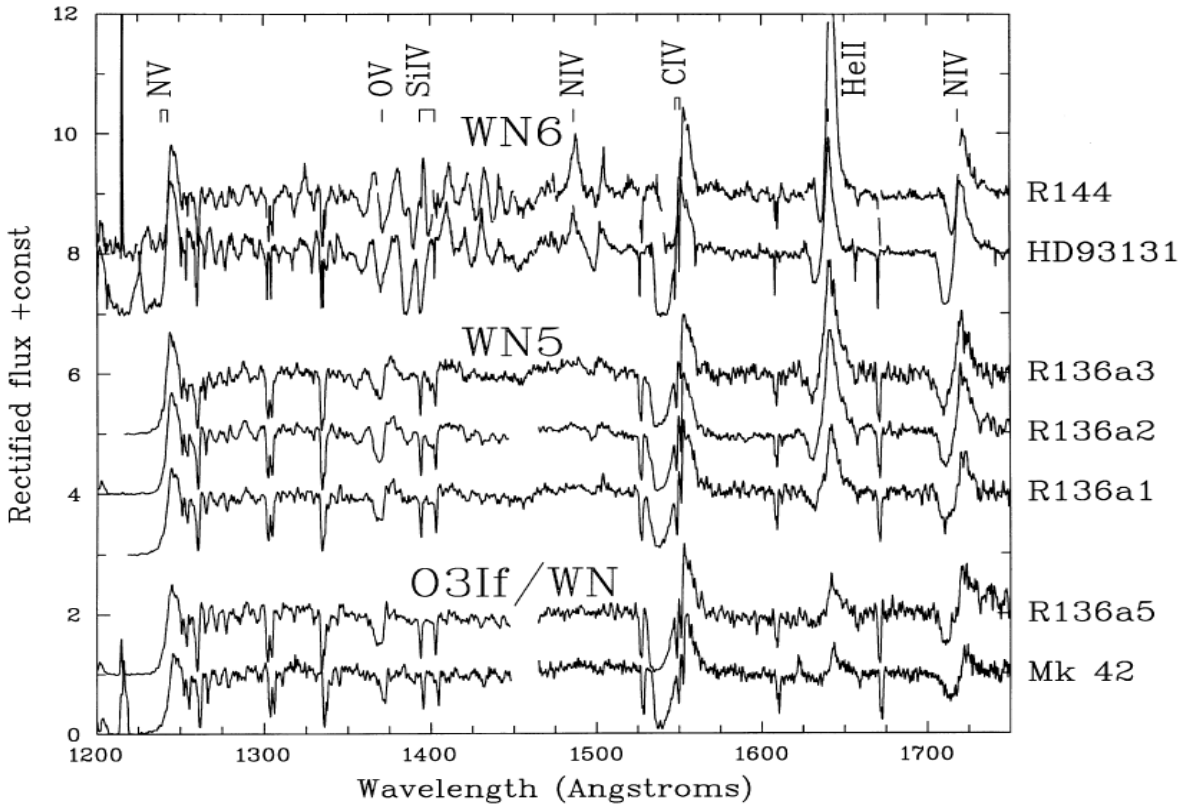

Figure 2. An ultraviolet spectral comparison between WN5h (R136a), WN6h (HD93131 and R144) and O3 If* /WN (R136a5 and Mk 42) stars (Crowther & Dessart, 1998).

WR stars have the following properties:
Terminal velocity (as derived from P Cygni profiles):

WN 500-3000 Km/sec
WC 800-3500 Km/sec
WO 4500 Km/sec

Temperatures and Luminosities:

WNL	T_{eff} = 30-35 kK	log(L/Lsun) = 5.9
WNE-s	T_{eff} = 40-90 kK	log(L/Lsun) = 5.5
WNE-w	T_{eff} = 40-90kK	log(L/Lsun) = 5.6

So, in addition to the strong emission lines, WR stars are very hot, with effective temperatures of 30,000 K to 90,000 K. WRs are also losing mass at rates in excess of 10^{-5} $M_{\odot}$/yr with wind speeds ranging from 800 km/sec to more than 3000 km/sec. In addition, there is strong evidence that many, and perhaps all, WR stars are rapidly rotating, with equatorial rotation speeds typically equaling to 300 km/sec.

Because of their high luminosities and bright emission lines, WR stars are **Miscellaneous variable stars (Percy, 2007)**

3. LBV stars

Non W-R stars, but other known hot and luminous variable stars, such as η Car, P Cyg, R71, R122, the S Doradus stars and the Hubble-Sandage variables, are clearly related to massive stars and undoubtedly represent an advanced evolutionary stage (Maeder, 1984), in 1984 P. Conti combined them as Luminous Blue Variables (Conti, 1984). LBVs are descendants of massive O stars, which are nearly to the end of the core hydrogen burning. They undergo episodic mass-loss and probably represent a transition between the most massive O star and the red supergiant and/or W-R stage (Massey, 2006). Extremely high luminosities of these stars place them near or above the Eddington limit. They are characterized by large variability of amplitudes and violent mass ejections. They have unusually high mass loss rates ranging from 10^{-6}-$10^{-3}M_{\odot}$/yr. P Cygni (34 Cyg,) is one of the most luminous stars of the Galaxy. It was classified as a Luminous Blue Variable following two major outbursts in 1600 and 1660.

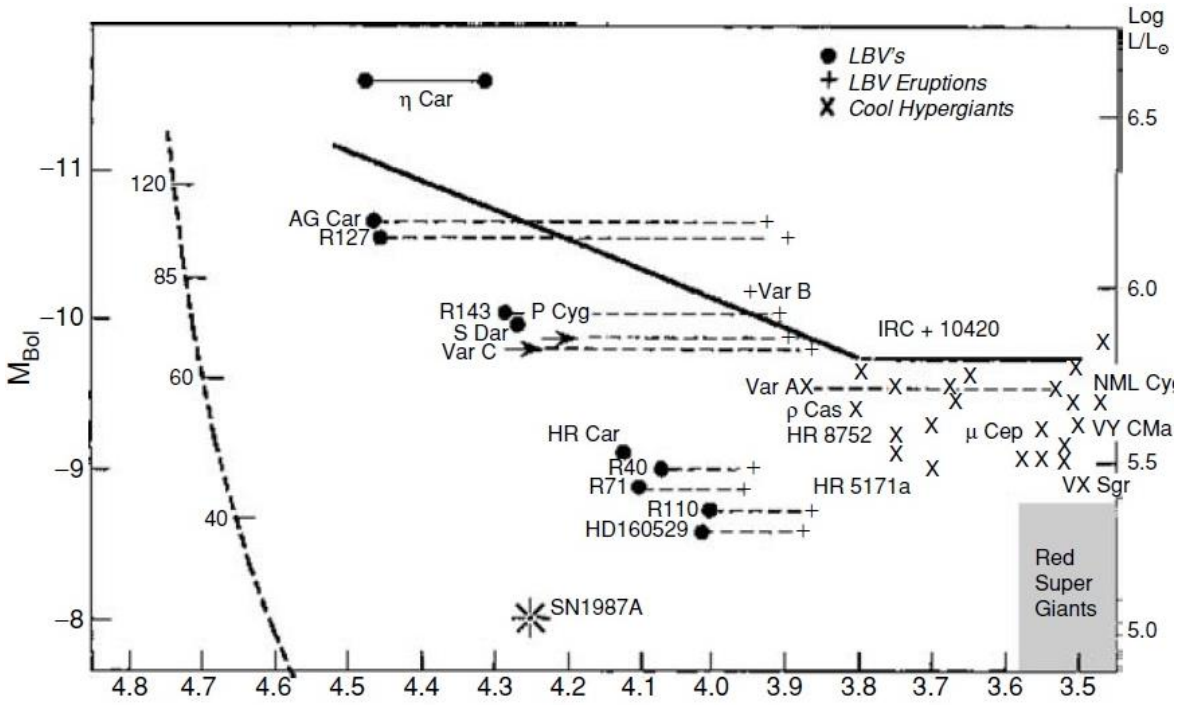

Figure 3. Location of hypergiants and WR stars on the H-R diagram. On the left is the upper main sequence, with the masses of the stars in solar units marked. The W-R stars lie in this region. Other blue, yellow, and red hypergiants are marked, including P Cygni, η Carinae, ρ Cassiopeiae, and the progenitor of SN1987A. The dashed lines represent the changes in the stars as they undergo major eruptions. The solid line is the empirical Humphreys-Davidson limit. (From R. M. Humphries et al. 2006, Percy, 2007)

The following three types of variability of Luminous Blue Variables are known: 1. Micro-variations with 0.1 mag. amplitude and comparatively small time-scale variations from days to weeks or months; 2. S Dor type variations or outbursts with amplitudes of 0.5 mag.; 3. Large sporadic outbursts with amplitude >2 mag. on a time-scale of 100 years.

LBVs are extraordinary because the fact that they can show different types of photometric and spectroscopic variations. The most famous examples for LBV major eruptions are the two 19th century eruption of η Car. This binary system contains a very massive LBV and a hotter and less luminous main sequence secondary star (Damineli, 1996) in a highly eccentric orbit of e≈ 0.9. The 1837-1858 Great Eruption created the bipolar Homunculus nebula, which contains 10-40 $M_\odot$ (Smith & Ferland 2007; Smith & Owocki 2006) and possibly more. Following the Great Eruption, a much less energetic Lesser Eruption took place between 1887 and 1895 and "only" 0.1-1 $M_\odot$ were ejected from the primary star. It was found that the Lesser Eruption of η Car started close to the periastron pass (Kashi & Soker 2010).

Figure 4. η Carina and its bipolar Homunculus nebula (N. Smith / J.A. Morse (U. Colorado) et al. / NASA).

There is a great deal of questions about the origin of the giant eruptions, their relation to normal LBV outbursts, and perhaps even to SNe. These eruptions are important. They may account for considerable mass loss and they indicate that some instability has been overlooked in stellar theory. However, it is important to distinguish them from the normal LBV/S Dor variability (Humphries et al. 2006). LBVs are stars in a transitional phase **the** massive stars may enter while evolving from main-sequence to Wolf-Rayet stars. The LBVs intrinsic photometric variability is based on the modulation of the stellar spectrum. In a few years, the spectrum shifts from OB to AF type and back. In their cool phase, LBVs are close to the Humphreys-Davidson (equivalent to Eddington/Omega-Gamma) limit. LBVs have a rather high mass loss rate, with stellar winds that are fast in the hot phase and slower in the cool phase of an LBV. These alternating wind velocities lead to the formation of LBV nebulae by wind-wind interactions. A nebula can also be formed in a spontaneous giant eruption, in which larger amounts of mass are ejected (Weis, 2015). If in its cool phase, a LBV star reaches certain temperature of approximately 9000-8000 K, it may undergo a great eruption (Figure 5).

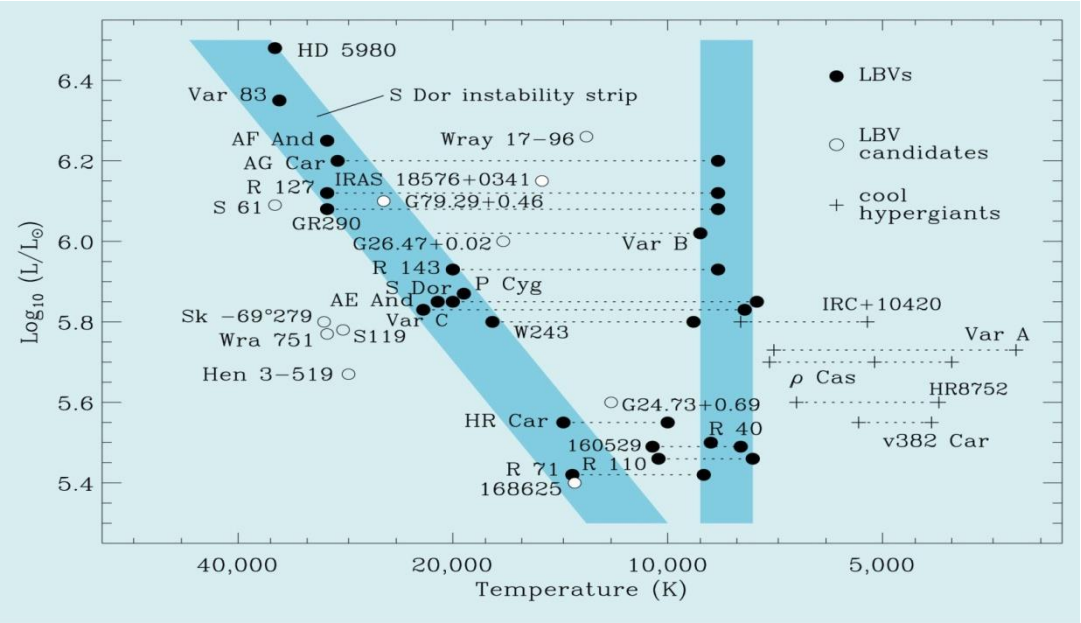

Figure 5. LBVs, and LBV candidates on the HR diagram. Two blue strips are so-called S Dor Instability strip and "constant temperature outburst phase" (Smith, Vink, & de Koter, 2004).

Whereas LBVs are all very massive stars of 85 $M_\odot$ or more, WRs can have progenitor masses as low as 20 $M_\odot$. Besides, WRs do not demonstrate the dramatic variability that is characteristic to LBVs.

4. New significant results regarding two LBVs- η Carinae and P Cygni

Now, we are going to consider two significant results concerning η Carinae and P Cygni. The first one was made on the basis of long-term observations of HST, while the second one was made on the basis of long-term UBV observations held at Abastumani Observatory.

American scientists (Megan Kiminki, Megan Reiter, Nathan Smith) have aligned eight epochs of HST imaging (both WFPC2 and ACS) of η Car's outer ejecta to the same distortion-corrected reference frame and measured the proper motions of 792 ejecta features, and many of them - for the first time. They achieved unprecedented time coverage, with each feature measured in up to 16 baselines for 21 years (1993-2014), as well as unprecedented velocity precision (few km/sec) and spatial resolution for these features. All 792 features measured in η Car's outer ejecta have transverse velocities pointing nearly directly away from the star. Their majority have proper motions of 300–600 km/sec, although some are as fast as 1500 km/sec. The fastest-moving material was found in the large feature, known as S ridge and in broadly jet-shaped N bow (Figure 6). Both date back to η Car's Great Eruption in the 1840s or to a few decades prior that date. Out of the 21-year-long data, the astronomers found no evidence of large-scale acceleration or deceleration of any of the outer ejecta: 94% of the knots were consistent with moving at constant velocity over that time. Under the assumption of constant velocity, they found that the material in and around the E and NNE condensations was ejected in the mid-1200s A.D., give or take 50–100 years. With the exception of three small knots to the far south of η Car and one to the northwest, the ejecta dating to the mid-1200s are all found to one side of the central star and are blueshifted.

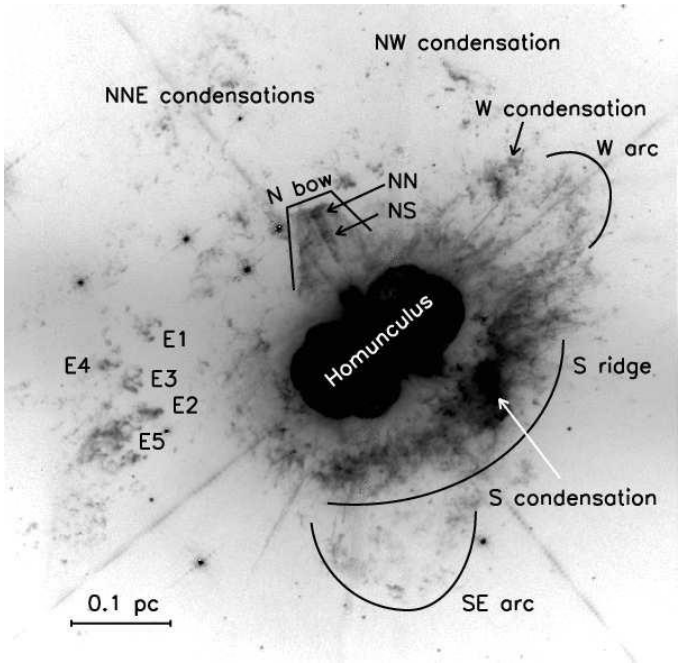

Figure 6. HST /WFPC2 image of ηCar in the F658N filter, which captures intrinsic and scattered [NII] λ6584 emission along with redshifted Hα emission (Morse 1999; Morse et al. 2001). Prominent features are labeled according to the convention of Walborn (1976) and Weis (2012) (according to Kiminki et al., 2016)

There has also been an evidence of a third, intermediate eruption that occurred in the sixteenth century. Ejecta dating to the mid-1500s are found in the SE arc, the W condensation, and in and around the NW condensation. From proper motions alone, we cannot rule out that this intermediate date peak is the result of newer ejecta from the Great Eruption hitting the older material from the 1200s. However, the radial velocities of these features place them in a different part of three-dimensional space from the thirteenth-century ejecta. The lack of X-ray emission over the SE arc and the features to the far north also indicates a lack of strong interaction between ejecta at those spots. In the total, with the distance-independent measurements, the American astronomers have demonstrated that η Car erupted at least once, likely twice, before its Great Eruption in the 1800s. Models for this still-enigmatic star must therefore explain the recurrence of these major mass-loss events, along with their several-hundred-year timescale and their various asymmetries.

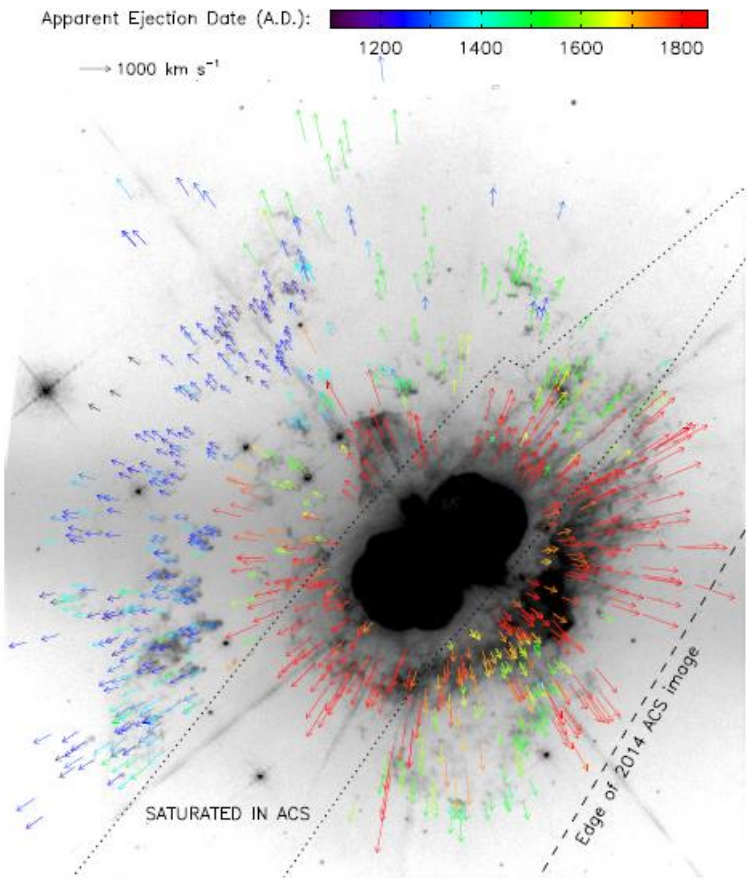

Figure 7. Vectors illustrating the observed proper motions of 792 features in the ejecta of η Car. The arrows are color-coded by the date of ejection from the central star, calculated assuming constant velocity. The region contaminated in the ACS images by bleeding from the highly saturated Homunculus is marked; features in this region were measured in WFPC2 data only (Kiminki et al., 2016)

.

Now, let us turn to the finding of Georgian astronomers (Nino Kochiashvili, Sopia Beradze, Ia Kochiashvili, Rezo Natsvlishvili, Manana Vardosanidze, who are the authors of this article) about P Cygni.

P Cygni was among the major observational targets at Abastumani Observatory in 1935-1983. We re-examined the data provided by Nikonov (1935-1937, V band, Nikonov, 1937) and by Magalashvili & Kharadze (1951-1983, UBV bands, Magalashvili & Kharadze, 1967), and there are also unpublished data of the star available. These data are especially significant for P Cygni investigators because they are filling the gap on the historical light curve of the star (Figure 8).

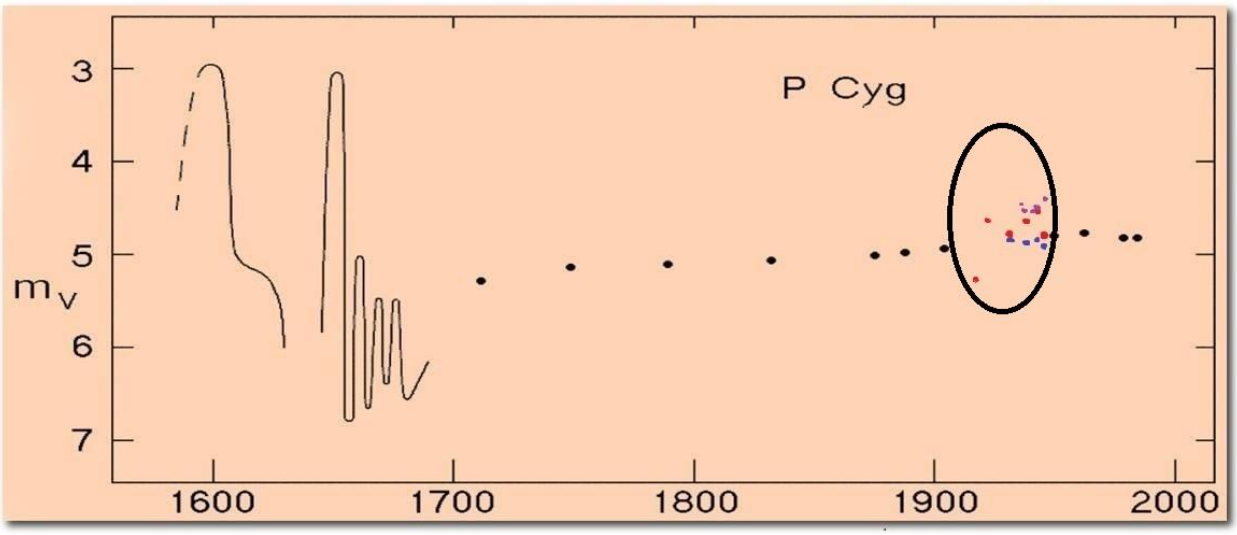

Figure 8. The light curve of P Cygni during 1600 - 2000 AD (by de Groot, 1988) with data by Nikonov, Kharadze and Magalashvili. Red points – V band, blue – B and purple – U (Beradze, et al., 2015).

UBV photoelectric observations of P Cyg were made using a 33-cm reflector. On the basis of these observations, Magalashvili and Kharadze made a conclusion that the behavior of the star was similar to W UMa variability, with the period of 0.500565 d and amplitude of 0.10-0.08 mag (Magalashvili and Kharadze, 1967). However, W UMa type variability was not confirmed. Kharadze and Magalashvili continued observing the star until 1983. After 1968 they used the same filters and the same photometer with a 48-cm Cassegrain telescope of Abastumani Observatory. These observations were not published by Kharadze and Magalashvili. We recalculated and revised UBV observations of P Cygni made by Nino Magalashvili and Eugene Kharadze in 1951-1983. According to these data, it seems that the star has different longer and shorter quasi-periodic flux variability.

We retrieved time series of P Cygni in two different ways: 1. Used 29 Cyg (HD 192640) as a comparison star, and 2. Used 36 Cyg (HD 193369). The following periods were identified:

1. (1480 ± 31) days; (736 ± 27) days.

2. (1123 ± 36) days; ~ 579 days and ≈128.7 days

Short quasi-period was also revealed of ~15-18 days. Long-period variability maybe due to the binarity of the star (Kochiashvili, et al., 2015).

Long-term photometric observations of P Cygni give the possibility to trace B-V and U-B colour variability of the star. It is accepted that P Cygni is gradually reddening. However, this behavior is very impressive in the observations of Kharadze-Magalashvili, because B-V value varies from 0.0 to 0.4 (two left parts in Figure 9). It means that the star seems to be the late A, early F spectral type, with temperature of 7500-9000 K. However, according to spectral observations of 2014 by Santerne (A. Santerne, 2014), temperature of P Cygni is T_{eff}=21000 K (T_{eff}=18200 K by Najarro, at al. See Najarro, at al, 1997).

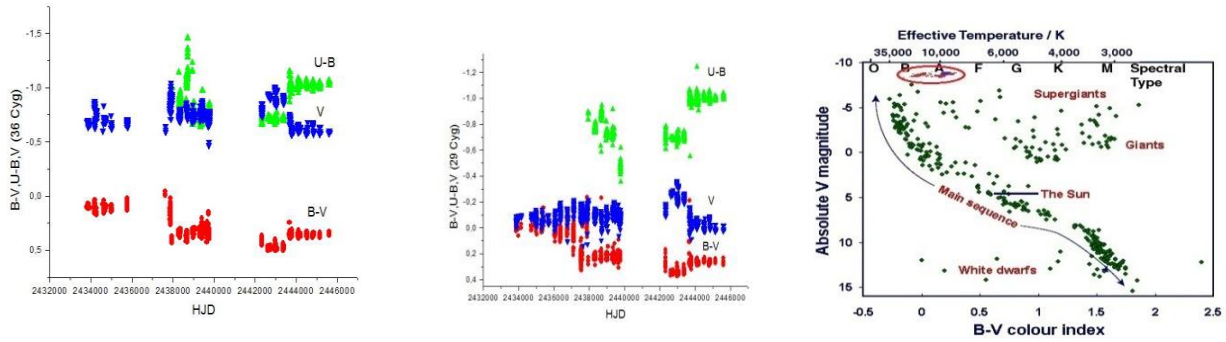

Figure 9. Colour behavior of P Cygni in 1951-1983. The star became redder by at least 0.4: B-V changed from 0.0 to 0.4 in 1951-1983 (Kochiashvili, et al., 2015).

After correcting for the reddening by 0.5 (Najarro, 2001), we have B-V values from -0.5 to -0.1 in 1951-1983. In the observations of 2014, the star's colour corresponded to the early B-spectral type (BI), and it seemed that the problem was resolved. However, B-V colour shift by approximately 0.55 in 1951-2014 is an observed fact (B-V varied in the range of 0.4-0.55 during the observational run of 2014).

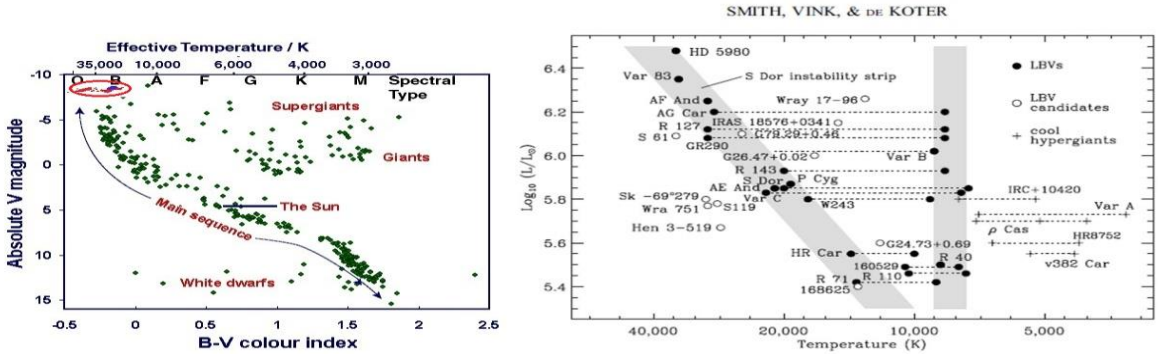

Figure 10. P Cygni on the HR diagram. It seems that it was an O-spectral type star in the first half of the 20th century (the left section of the figure, Kochiashvili, et al. 2015). If the colour behavior of P Cygni have the same character in future, then star will reach the "constant temperature outburst phase". The right section of the Figure (Smith et al., 2004).

The study of the brightness variations of P Cygni (according to different investigators of the star), between 1985 and 1992/2000 reveals different time-scales as follows: A long period of the order of 1540 or 4.2 years is identified as so-called Short S Doradus Phase (van Genderen, 2001). A shorter quasi-period of approximately 100 days can be identified quite frequently and is similar to the so called 100-days micro-variations also found in other, similar objects. There is a firm evidence of the presence of a stable period of 17.34 ± 0.1 days with amplitude of not greater than 0.1 mag. These variations are identified with so-called α Cygni-type micro-variations. However, their colour behaviour is variable: sometimes the star reddens when it brightens, and sometimes the star becomes bluer on such occasions. This is not entirely similar to the colour behaviour of the α Cygni type variations in other stars (van Genderen et al.1997), where the colour is always bluer in the light maxima.

We observed P Cygni in the period of July 23 - October 20, 2014 with a 48-cm Cassegrain telescope and standard B,V,R,I filters (see Beradze, et al. 2015; Kochiashvili, et al., 2015). HD 228793 was used as a comparison star. We found spectral observations of the star by Alexandre

Santerne with the HARPS-N spectrograph, attached to TNG (A. Santerne, 2014). The spectral and B,V,R,I observations of P Cygni of 2014 are presented in Figure 11.

a) b)

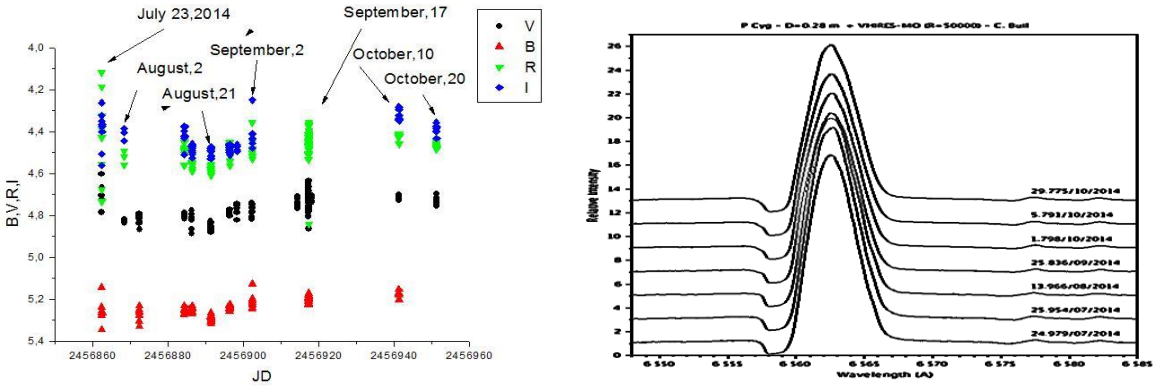

Figure 11. Observations of P Cygni in 2014: a) BVRI photometric observations accomplished in Abastumani;

b) observations of Hαaccomplished by using TNG. Here, we have the following EWs:

24.979/07/2014 - EW=64.1 Å; 29.954/07/2014 - EW=66.0 Å,
13.966/08/2014 - EW=62.7 Å; 25.856/09/2014 - EW=56.0 Å;
01.798/10/2014 - EW=54.0 Å; 05.791/10/2014 - EW=52.4 Å;
29.775/10/2014 - EW=53.7 Å.

We found out that during our observations, the star underwent light variations with the mean amplitude of approximately 0.1 magnitudes in all pass-bands and the period of this change was approximately 68 (67,8) days. There is also a relation between brightness and the Hα EW variability. Therefore, we think that the cause of this feature may be a variability rate of the stellar wind, which is very strong in this star. Changes in the rate of the stellar wind, on the other hand, may be caused by the pulsation of the star.

Main Results. According to the observed rate of colour change, it seems that the star may reach the place on the HR diagram, where it may undergo the next great eruption, or even supernova explosion in 80-120 years. So, we have a clear evidence of the evolutionary changes in P Cygni, which approximately one century ago, was most likely an O-spectral type star, while now, it is B1-2 instead.

5. Some aspects of massive stars evolution

In a scheme originally suggested by Peter Conti in 1976, which was subsequently modified, a general evolutionary path for massive stars has been outlined. In each case, the star ends its life with a supernova (SN) explosion (Caroll & Ostlie, 2007):

$$m > 85\ \mathcal{M}_{\odot}\text{: O} \longrightarrow \text{LBV} \longrightarrow \text{WN} \longrightarrow \text{WC} \longrightarrow \text{SN}$$

$$40 > m > 85\ \mathcal{M}_{\odot}\text{: O} \longrightarrow \text{WN} \longrightarrow \text{WC} \longrightarrow \text{SN}$$

$$25 > m > 40\ \mathcal{M}_{\odot}\text{: O} \longrightarrow \text{RSG} \longrightarrow \text{WN} \longrightarrow \text{WC} \longrightarrow \text{SN}$$

$$20 > m > 25\ \mathcal{M}_{\odot}\text{: O} \longrightarrow \text{RSG} \longrightarrow \text{WN} \longrightarrow \text{SN}$$

$$10 > m > 20\ \mathcal{M}_{\odot}\text{: OB} \longrightarrow \text{RSG} \longrightarrow \text{BSG} \longrightarrow \text{SN}.$$

This qualitative evolutionary scheme has been supported by the detailed numerical evolutionary models of a massive star formation. Evolutionary tracks for stars of solar composition ranging in mass from 9 $M_{\odot}$ to 120 $M_{\odot}$ are shown in Figure 12. These models of Georges Meynet and Andres Maeder include mass loss typical to massive stars. In addition, the models were computed with and without rotation; with rotation, the equatorial rotation speed is taken at 300 km/sec. Meynet and Maeder point out that rotation can have an appreciable effect on the stellar evolution, including driving internal mixing and enhancing mass loss (Caroll & Ostlie, 2007).

An evolutionary scenario of massive stars much depends on metallicity.

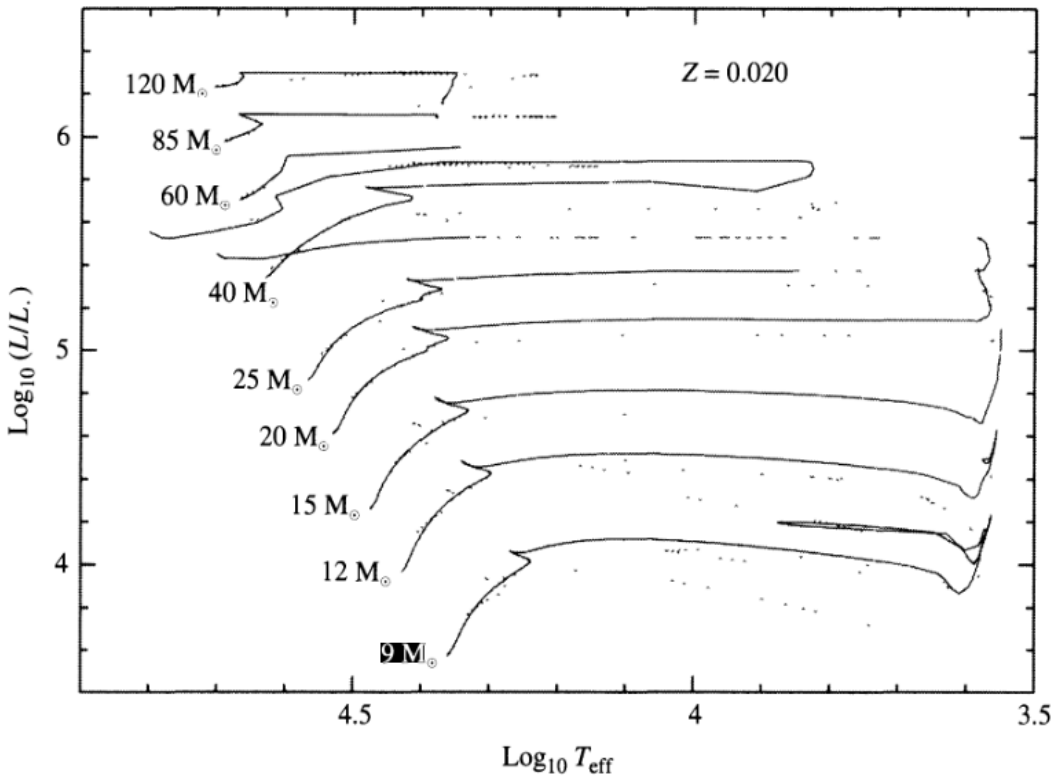

Figure 12.The evolution of massive stars with Z 0.02. The solid lines are evolutionary tracks computed with initial rotation velocities of 300 km/sec, and the dotted lines are evolutionary tracks for stars without rotation. Mass loss was included in the models and it significantly impacts the evolution of these stars (Meynet and Maeder, 2003).

Massive stars at very low metallicity (1/50 $Z_{\odot}$) evolve differently to those at solar Z (Meynet & Maeder 2002; Brott et al. 2011; Yoon et al. 2012; Yusof et al. 2013). Szecsi and co-authors have computed low-Z stellar evolutionary models in the mass range of 9-300 $M_{\odot}$ and with initial

rotational velocities between 0 and 600 km/sec (Szecsi et al. 2015). Figure 13 shows a representative sample of the computed tracks in HR diagram. The slow rotators (<200 km/sec) follow the normal evolutionary path, which proceeds redwards from the ZAMS. After core-hydrogen burning, these stars develop a distinct core-envelope structure (i.e. no enhanced mixing between the core and the surface), burn helium on the red-supergiant branch and would explode as Type IIP supernovae (Langer 2012; Yoon et al. 2012; Szecsi et al. 2015).

On the other hand, the fast rotators (>300 km/sec) evolve bluewards from the ZAMS, and undergo chemically-homogeneous evolution. In this case, the mixing timescale is significantly shorter than the main-sequence lifetime of these stars, so all the nuclear burning products are mixed throughout the star. These stars stay compact and hot, spending their post-main-sequence lifetimes as fast rotating helium stars and would, according to the collapsar scenario, explode as long-duration gamma-ray bursts (LGRBs) (Yoon & Langer 2005; Woosley & Heger 2006; Yoon et al. 2006; Brott et al. 2011; Szecsi et al. 2015).

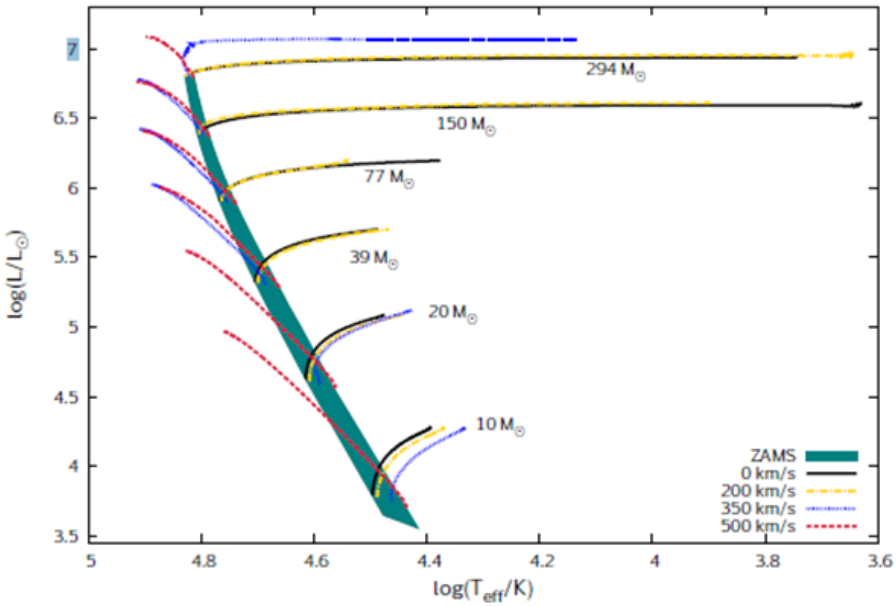

Figure 13.Evolutionary tracks in HR diagram during the core-hydrogen-burning phase for models with initial masses between 10-294 $M_{\odot}$ (see labels) and initial rotational velocities of 0, 200, 350 and 500 km/sec, with a composition of 1/50 $Z_{\odot}$ (Szecsi et al. 2015). Green shading identifies the zero-age main-sequence.

6. Conclusions

Modeling of stellar evolution is still subject to many uncertainties. However, we are now reaching an epoch, in which models and observations are going to be in agreement. Refining the uncertainties on both models and the observational data will be essential for the future progress (Eldridge, et al., 2015). We hope to get interesting results using our small size telescope for photometry of massive bright LBV and WR stars. Making this kind of photometry with small telescopes is advantageous now, because in fact, it is impossible to do this by using large modern observational observational facilities.

References

Beradze, S.; Kochiashvili, N.; Natsvlishvili, R.; Kochiashvili, I.; Janiashvili, E.; Urushadze, T.; Vardosanidze, M. P Cygni and its Observations at the Abastumani Observatory. Wolf-Rayet Stars: Proceedings of an International Workshop held in Potsdam, Germany, 1-5 June 2015. Edited by Wolf-Rainer Hamann, Andreas Sander, Helge Todt. Universitätsverlag Potsdam, p.353, 2015.

Brott, I., de Mink, S. E., Cantiello, M., et al. Rotating massive main-sequence stars. I. Grids of evolutionary models and isochrones. A&A, 530, A115, 2011.

Conti Peter S. Basic Observational Constrains on the Evolution of Massive Stars, International Astronomical Union Symposium No. 105, p. 233. 1984.

Caroll B.W.,Ostlie D.A. An Introduction of Modern Astrophysics. 2007.

Crowther, P. A.; Dessart, Luc. Quantitative spectroscopy of Wolf-Rayet stars in HD97950 and R136a - the cores of giant HII regions. MNRAS, Volume 296, Issue 3, pp. 622-642.

Crowther, Paul A., Properties of Wolf-Rayet Stars. Massive Stars as Cosmic Engines, Proceedings of the International Astronomical Union, IAU Symposium, Volume 250, p. 47-62, 2008.

Crowther, P. A.; Schnurr, O.; Hirschi, R.; Yusof, N.; Parker, R. J.; Goodwin, S. P.; Kassim, H. A. "The R136 star cluster hosts several stars whose individual masses greatly exceed the accepted 150 $M_{\odot}$ stellar mass limit". MNRAS, 408, p. 731, 2010.

Damineli, A.The 5.52 Year Cycle of Eta Carinae, ApJL, v.460, p.L49, 1996.

de Groot M., The most luminous stars in the universe. Ir. Astron. J., 18, 163, 1988.

Eldridge, J. J.; McClelland, L. A. S.; Xiao, L.; Stanway, E. R.; Bray, J. The importance of getting single-star and binary physics correct. Wolf-Rayet Stars: Proceedings of an International Workshop held in Potsdam, Germany, 1-5 June 2015. Edited by Wolf-Rainer Hamann, Andreas Sander, Helge Todt. Universitätsverlag Potsdam, p.177-182, 2015.

Haiman, Zoltán; Loeb, Abraham, Signatures of Stellar Reionization of the Universe. ApJ, Volume 483, Issue 1, pp. 21-37. 1997.

Humphries, R. M. et al. (2006), 'M33's Variable A - a hypergiant star more than 35 years in eruption', AJ, 131, 2105--13.

Kashi, Amit. An indication for the binarity of P Cygni from its 17th century eruption, MNRAS, Vol. 405, Issue 3, pp. 1924-1929. 2010.

Kiminki, M.; Reiter, M.; Smith, N. Ancient eruptions of η Carinae: a tale written in proper motions, MNRAS, Volume 463, Issue 1, p.845-857, 2016.

Kochiashvili, N.; Beradze, S.; Kochiashvili, I.; Natsvlishvili, R.; Vardosanidze, M. New Photometric Observations of P Cygni. Wolf-Rayet Stars: Proceedings of an International Workshop held in Potsdam, Germany, 1-5 June 2015. Edited by Wolf-Rainer Hamann, Andreas Sander, Helge Todt. Universitätsverlag Potsdam, p.360, 2015.

Langer, N. Presupernova Evolution of Massive Single and Binary Stars. ARA&A, 50, 107, 2012.

Maeder A. Observational Tests of the Stellar Evolution Theory. International Astronomical Union Symposium No. 105, held in Geneva, Switzerland, September 12-16, 1983. Editors, Andre Maeder, Alvio Renzini; Publisher, D. Reidel Publishing Company, Dordrecht, The Netherlands, Boston, MA, Hingham, MA. Sold and distributed in the U.S.A. and Canada by Kluwer Academic Publishers, 1984. LC # QB806 .O27 1984.ISBN # 90-277-1774-5.P.299, 1984.

Magalashvili N; Kharadze E: Periodicity of the Light Variation of P Cygni. IBVS, 210, 1, 1967.

Massey, Philip. The Discovery of a P Cygni Analog in M31. ApJ, v 238, pp. L93-L96. 2006.

Meynet, G. &Maeder, A.Stellar evolution with rotation. VIII. Models at Z = 10^{-5} and CNO yields for early galactic evolution.A&A, 390, 561, 2002.

Meynet, G.; Maeder, A. Stellar evolution with rotation. X. Wolf-Rayet star populations at solar metallicity. Astronomy and Astrophysics, v.404, p.975-990, 2003.
Morse J. A., 1999, in Morse J. A., Humphreys R. M., Damineli A., eds, Astronomical Society of the Pacific Conference Series Vol. 179, Eta Carinae at The Millennium. p. 13, 1999
Morse J. A., Kellogg J. R., Bally J., Davidson K., Balick B., Ebbets D., ApJ, 548, L207, 2001.
Najarro,F.; Hillier,D.J.; Stahl,O., A spectroscopic investigation of P Cygi. I. H and HeI lines. A&As, v.326, p. 1117-1134, 1997.
Najarro, F., Spectroscopy of P Cygni. P Cygni 2000: 400 Years of Progress 233: 133, 2001.
Percy J.R. Understanding Variable Stars. 2007.
Nikonov V.B. Photoelectric Observation of P Cygni. 1937, Bull. AbAO, 1, p. 35-38.
Santerne, A., 2014. http://www.spectro-aras.com/forum/viewtopic.php?f=17&t=996
Smith,N.; Vink,J., Koter,A., The Missing Luminous Blue Variables and the Bistability Jump. AJ, v.615, p. 475-484, 2004.
Smith, Nathan; Ferland, Gary J.The Structure of the Homunculus. II. Modeling the Physical Conditions in η Carinae's Molecular Shell. ApJ, Volume 655, Issue 2, pp. 911-919, 2007.
Smith, Nathan; Owocki, Stanley P.On the Role of Continuum-driven Eruptions in the Evolution of Very Massive Stars and Population III Stars. ApJ, Volume 645, Issue 1, pp. L45-L48, 2006.
Szécsi, D.; Langer, N.; Sanyal, D.; Evans, C. J.; Bestenlehner, J. M.; Raucq, F. Do rapidly-rotating massive stars at low metallicity form Wolf-Rayet stars? Wolf-Rayet Stars: Proceedings of an International Workshop held in Potsdam, Germany, 1-5 June 2015. Edited by Wolf-Rainer Hamann, Andreas Sander, Helge Todt. Universitätsverlag Potsdam, p.189-192, 2015.
vanGenderen A.M., Sterken C., de Groot M.J.H., New perceptions on the S Doradus phenomenon and the micro variations of five Luminous Blue Variables (LBVs), A & A Supplement series, Vol. 124, p. 517, 1997.
vanGenderen A.M., S Doradus variables in the Galaxy and the Magellanic Clouds, A&A, v. 366, p. 508. 2001.
Walborn N. R.,The complex outer shell of Eta Carinae. ApJ, 204, L17, 1976.
Weis K., in Davidson K., Humphreys R. M., eds, Astrophysics and Space Science Library Vol. 384, Astrophysics and Space Science Library. p. 171, 2012.
Weis, K. Family ties of WR to LBV nebulaeyielding clues for stellar evolution. Wolf-Rayet Stars: Proceedings of an International Workshop held in Potsdam, Germany, 1-5 June 2015. Edited by Wolf-Rainer Hamann, Andreas Sander, Helge Todt. Universitätsverlag Potsdam, p.p. 167-170, 2015.
Woosley, S. E.; Heger, A.The Progenitor Stars of Gamma-Ray Bursts.ApJ, Volume 637, Issue 2, pp. 914-921, 2006.
Yoon, S.-C., Dierks, A., & Langer, N. Evolution of massive Population III stars with rotation and magnetic fields. A&A, 542, A113, 2012.
Yoon, S.-C.& Langer, N. Evolution of rapidly rotating metal-poor massive stars towards gamma-ray bursts.A&A, 443, 643, 2005.
Yoon, S.-C., Langer, N., & Norman, C.Single star progenitors of long gamma-ray bursts. I. Model grids and redshift dependent GRB rate. A&A, 460, 199, 2006.
Yusof, N., Hirschi, R., Meynet, G., et al.,Evolution and fate of very massive stars. MNRAS, 433, 1114, 2013.

Astronomy & Astrophysics (Caucasus) 2, (2016) (41-46)

FIRST TEST OBSERVATIONS OF THE SELECTED ASTRONOMICAL OBJECTS USING POLARIZATION – HOLOGRAPHIC STOKES POLARIMETER

T. Kvernadze[1], G. Kurkhuli[1], B. Kilosanidze[2], G. Kakauridze[2], V. Kulijanishvili[1], E. Khutsishvili[1], O. Kvaratskhelia[1], D. Khutsishvili[1]

[1] E. Kharadze Abastumani Astrophysical Observatory at the Ilia State University, 3/5 Cholokashvili str., 0162 Tbilisi, Georgia
[2] Laboratory of Holographic recording and processing of Information, Institute of Cybernetics of Georgian Technical University

Email:solar-corona@yahoo.com

Received October 10, 2016; revised December 17, 2016

Abstract

We present an innovative polarization-holographic imaging Stokes polarimeter based on an integral polarization-holographic diffraction element, which allows accomplishing real time analysis of the polarization state of incoming light. An element decomposes the incoming light into diffraction orders, the intensities of which vary depending on the polarization state of the light source. After the CCD intensity measurements of the corresponding points or areas in the diffraction orders and further data reduction through the calibration parameters, we get the real-time Stokes images of the light source, which allows determining full polarization state of a point or extended space object for different spectral regions. The operating spectral range of the polarimeter is 500-1600 nm with diffraction efficiency equal to 20% at 532 nm, 16% at 635 nm and 2% at 1550 nm. The theoretical model of relations between measured intensities in different diffraction orders and Stokes parameters were used to calibrate the polarimeter. Experimental results show that the resulting errors are better than 10^{-2} and prove the great potential of such polarimeter for observations of various space objects including spectropolarimetric observations of the solar active formations like the solar spicules and prominences. The polarization-holographic imaging Stokes polarimeter is very compact, light-weight and suitable to be installed both on large or small ground-based and airborne telescopes.

Key words: Polarization-holographic, Polarization-sensitive materials, Stokes astropolarimeter

1. Introduction

The theory of polarization-holography was first proposed by in (Sh. Kakichashvili 1972 ,1989). This method allows creating a unique polarization-holographic element, which is capable of doing a full polarization state analysis of an incident light in real time and in a wide spectral range including near infrared. The element decomposes the incident light of any polarization state into the orthogonal circular and linear bases, forming diffraction orders.

The measurements of intensities of the diffraction orders determine all four Stokes parameters and the parameters of the corresponding polarization ellipse as a result: ellipticity, position angle and the direction of rotation, as well as the degree of polarization.

We developed a polarimetric device or polarization-holographic Stokes polarimeter on the basis of the kind of element, which has no mechanically moving or electronically tunable parts, but only one basic element connected to a couple of lenses and a photodetector (Figure 1). The polarimeter is compact, relatively cheap and light-weight being particularly important for the installation on

airborne or space telescopes. The speed of the operation of the polarimeter is limited only by computer processing. Besides, it gives the possibility of simultaneous investigation of polarization properties of the space objects in different spectral ranges.

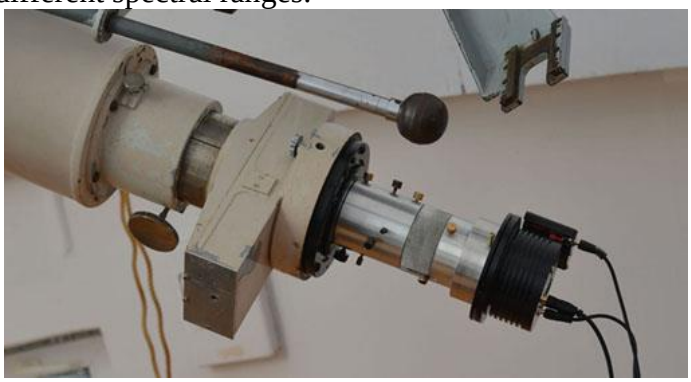

Figure 1. Polarization-holographic polarimeter equipped with Starlight Express Trius SX-36 CCD and mounted on the solar photosphere telescope at Abastumani Astrophysical Observatory (Georgia).

2. Method of Polarization-holography

The polarization-holographic element decomposes incident light into orthogonal circular and linear diffraction orders. As a result, we get two orthogonal circularly polarized beams with intensities I_{+c} and I_{-c}, two linearly polarized beams with position angle +45°, two linearly polarized beams with position angle +90° and with intensities I_{45} and I_{90}, correspondingly and none diffracted beam or zero order with a state of polarization identical to incoming beam and with intensity I_0.

The measurements of intensities of diffracted orders allow to determine all four Stokes parameters by means of the following relations developed by (Kakauridze and Kilosanidze 2007.,2009.,2011).

$$
\begin{aligned}
I_\lambda &= k_{+c,\lambda} I_{+c,\lambda} + k_{-c,\lambda} I_{-c,\lambda}, \\
Q_\lambda &= (k_{+c,\lambda} I_{+c,\lambda} + k_{-c,\lambda} I_{-c,\lambda}) - 2k_{90\lambda} I_{90} \\
U_\lambda &= 2k_{45,\lambda} I_{45} - (k_{+c,\lambda} I_{+c,\lambda} + k_{-c,\lambda} I_{-c,\lambda}), \\
V_\lambda &= (k_{+c,\lambda} I_{+c,\lambda} - k_{-c,\lambda} I_{-c,\lambda})
\end{aligned}
\qquad (1)
$$

Where *k* terms are coefficients associated with the absorption of a light in an element, diffraction efficiency of an element and the optoelectronic transformations done by the photodetectors. The values of these coefficients are determined experimentally during the calibration (Kilosanidze B., et al. 2015).

3. Calibration and Test Observations

The principal schema of the polarization-holographic Stokes polarimeter and configuration of diffraction orders are shown in Figure 2.

The polarimeter was mounted on a telescope or a spectrograph and aligned to get the focal plane located at the entrance diaphragm or slit of the polarimeter. The light passing through the diaphragm is transformed by the collimating lens into a parallel beam, which than passes an optional light filter and impacts a polarization-holographic element. The diffraction order beams are further collected by an objective lens and a polarization-holographic image is formed on the surface of a CCD camera. Currently we use the Starlight Express Trius SX-36 CCD camera with array of 36.3 x 24.2 mm or 4904 x 3280 pixels at 7.4 μm pixel size.

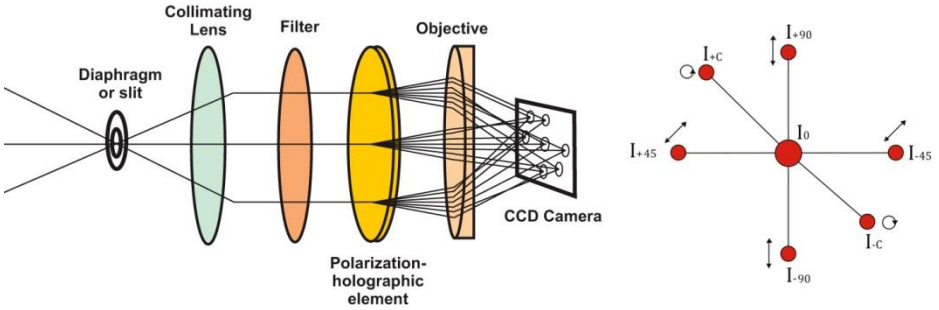

Figure 2. Principal schema of a polarization-holographic Stokes polarimeter (left) and configuration of diffraction orders (right)

For calibration of the polarimeter, the observations of Vega were carried out through the standard V filter. The polarimeter was mounted on a refractor with a 10-cm aperture and 1-m focal length. A polaroid was attached at the front of the telescope to compensate any instrumental polarization and rotated with a fixed angle usually equal or less than 45° to get a sequence of CCD images with known linear polarization and position angles. The CCD camera control, CCD image data acquisition, data processing and further aperture photometry of the 1st orders were performed using MaxIm DL Pro 5 software (Figure 3).

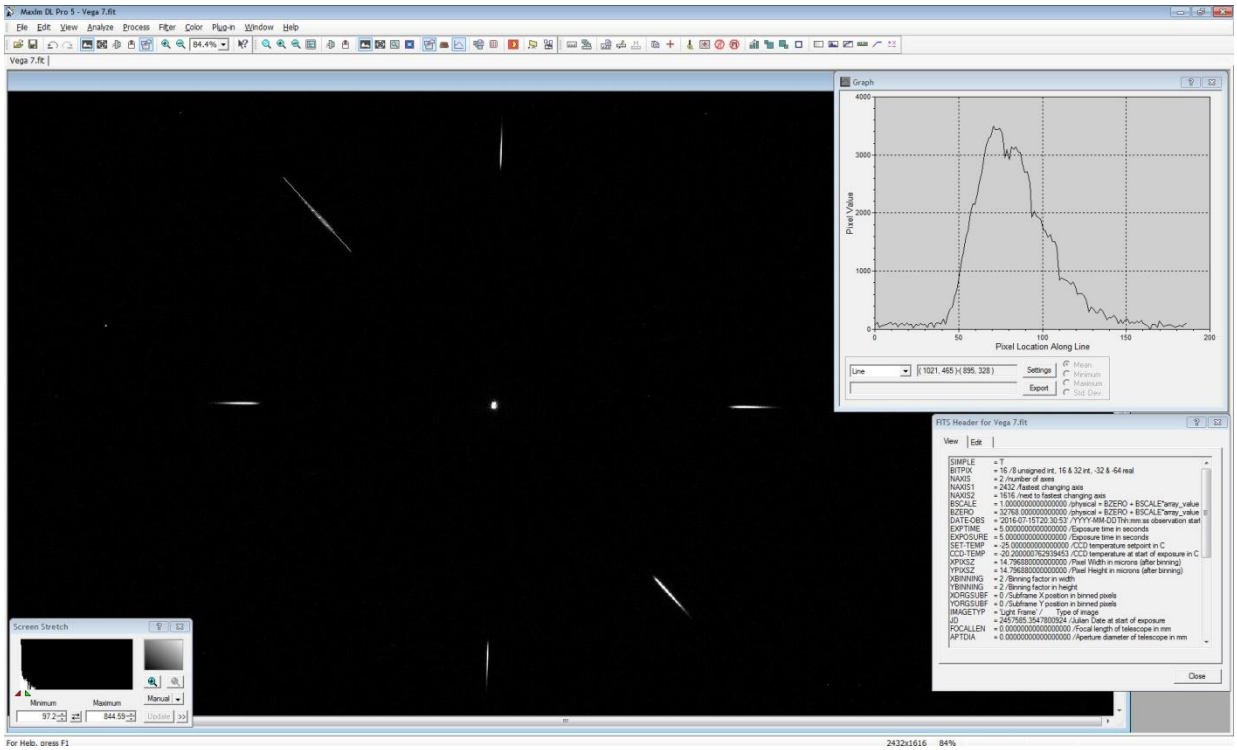

Figure 3. Starlight Express Trius SX-36 CCD polarization-holographic image of Vega

The measured intensities of I_0, I_{+c}, I_{-c}, I_{90} and I_{45} were used to estimate coefficients in relations (1). The normalized Stokes parameters were calculated for the same measurements. Table 1 shows the results of measurements and Figure 4 shows the variations of all Stokes parameters with position angles of the linearly polarized light.

Table 1. The deviations between the theoretical and the measured values of DOP and position angle

Position angle of a calibrating polaroid, degree	Degree of Polarization, %		Estimated position angle, grad.	Deviation between the theoretical and the measured position angles, grad.
	Theoretical	Measured		
315.0	100.0	100.9	315.15	-0.15
270.0	100.0	100.1	269.34	0.66
225.0	100.0	98.5	225.73	-0.73
180.0	100.0	100.0	180.35	-0.35
135.0	100.0	100.0	135.14	-0.14
90.0	100.0	100.7	89.34	0.66
45.0	100.0	100.0	45.46	-0.46
0.0	100.0	99.6	-0.56	0.56
	Mean value	100.0 %		0.0°
	Standard error	±0.7 %		±0.5°

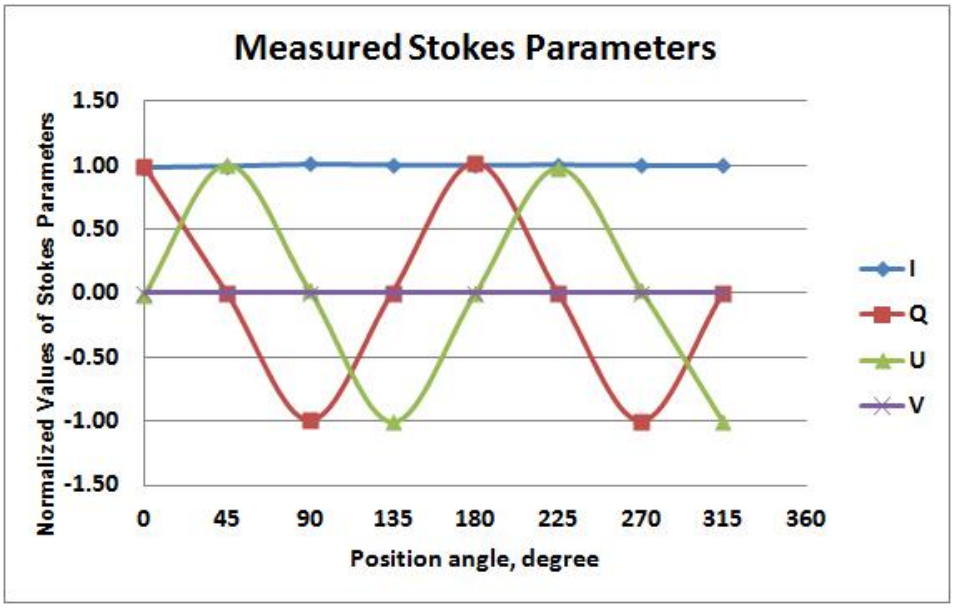

Figure 4. The results of calibration measurements: variation of normalized Stokes parameters with a position angle of linearly polarized light of Vega.

For determination of a spectral dispersion in the first orders, the observations of Vega were carried out with the same telescope as above. Several spectral lines were identified in the spectra of Vega and used to fit the spectral dispersion curve shown in Figure 5. The reciprocal spectral dispersion appeared to be equal to 724 ±6 Å/mm.

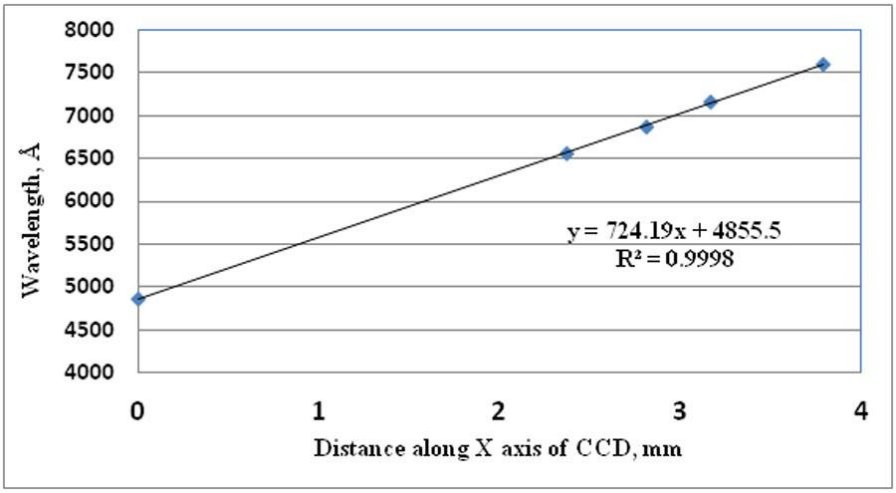

Figure 5. Spectral dispersion curve of Polarization-holographic orders determined by using observations of Vega

The test spectropolarimetric observations of the solar spicules in Hα line were carried out on September the 8th, 2016, using 53-cm Lyot coronagraph and its spectrograph, which has a reciprocal spectral dispersion of 0.96 Å/mm.

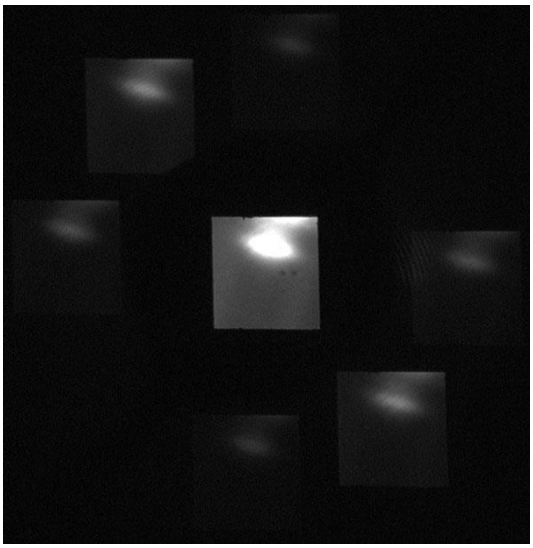

Figure 6. Polarization-holographic image of the solar spicule spectra near Hα taken with a spectrograph of the 53-cm coronagraph of Abastumani Astrophysical Observatory (Georgia). The direction of spectral dispersion is aligned along X axis of the image declined by 25 degrees. The spectrograph slit is aligned parallel to the solar limb.

4. Data Reduction and Results

The CCD images of the spicules were reduced with the standard dark subtraction, flat fielding and background subtraction procedures. The diffraction orders' sub-images were scanned along the spectral dispersion direction with scanning line of an identical length. The scanning line was shifted along Y axis of the images for 21 pixels with a 1-pixel step to cover the whole image of the spicules. The corresponding intensity profiles for each diffraction order were aligned to Hα line peak. The integration and smoothing algorithms were applied for the intensity profiles to increase the S/N ratio.

Special spectropolarimetric calibration observations of the solar photosphere were carried out in a Hα absorption line immediately following the observations of the spicules with identical setup of the telescope and the polarimeter. The polaroid was placed in front of the spectrograph slit and rotated by 45 degrees to obtain linear polarization light beam with different phase angles. The image processing and data retrieval procedures were the same as for the spicule images. The Hα line minimums were used to calculate the calibration parameters.

The intensity profiles of the spicules were transformed to the Stokes profiles using the calibration data. The resulting normalized Stokes profiles are depicted in Figure 7.

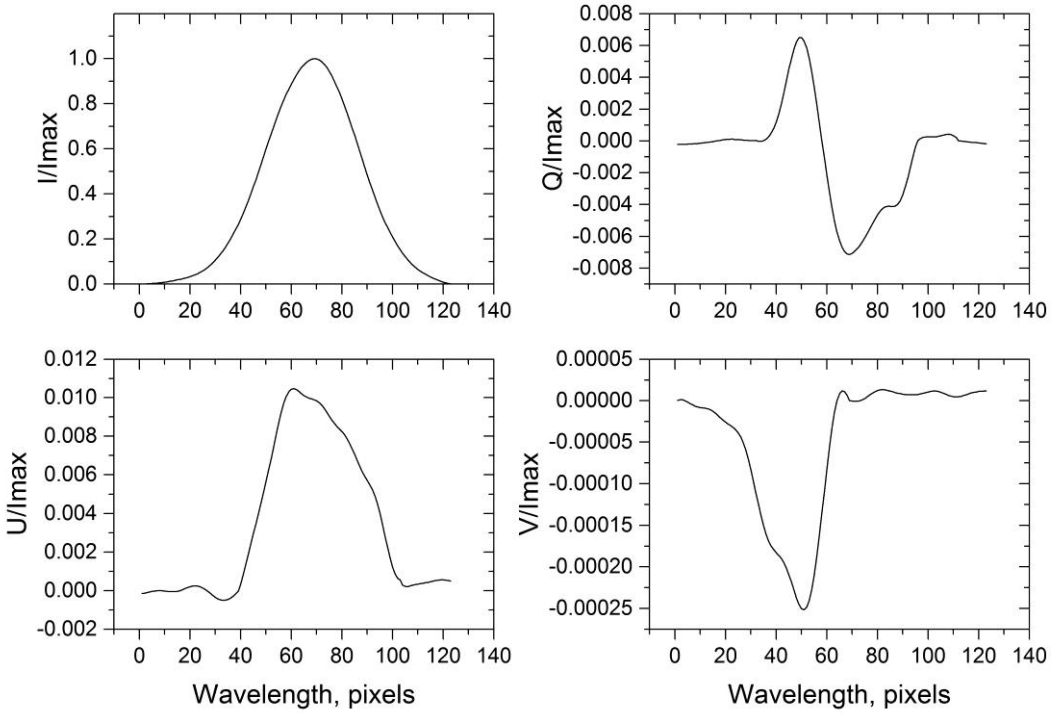

Figure 7. Observed Stokes profiles of Hα in the solar spicule observed on the 8th of September, 2016. Stokes parameters *I, Q, U* and *V* are normalized to I_{max} value.

There are several features in the Stokes profiles in Figure 7, which seem unusual and need to be emphasized: i) change of sign in Q/I_{max} profile, which might be caused by the unresolved components of the spicule, which have different Doppler velocities and orientation of magnetic fields, ii) circular polarization profile V/I_{max} shows peculiar shape with a suppressed red positive component.

5. Conclusions

We present the theoretical basis, development, design and the results of laboratory and observational tests of the innovative real-time polarization-holographic imaging Stokes polarimeter.

The first prototype of the polarimeter was built according to the developed principal schema and specially designed and recorded polarization-holographic element. Experimental results show that the resulting errors are better than 10^{-2} and prove the great potential of such a polarimeter in observations of various space objects including spectropolarimetric observations of the solar active formations, like the solar spicules and prominences are. The polarization-holographic imaging Stokes polarimeter is very compact, light-weight and suitable to be installed both on large or small ground-based and airborne telescopes. In addition, it is extremely important to continue the further investigations to improve its efficiency.

Acknowledgement

The authors gratefully acknowledge the support by the Shota Rustaveli National Science Foundation of Georgia (Grant No. AR/209/6-120-14).

References

Kakauridze, G. and Kilosanidze, B. 2011. Proc. SPIE, 7957, 7957-28.
Kakichashvili, Sh. 1972. J. Opt. Spectrosc. 33 (2), 324.
Kakichashvili, Sh. 1989. Polarization holography, Nauka, Leningrad, USSR.
Kilosanidze, B. and Kakauridze, G. 2007, Appl. Opt. 46(7), 1040-1049.
Kilosanidze, B. and Kakauridze, G. 2009. Proc. SPIE, 7358.
Kilosanidze, B., Kakauridze, G., Kvernadze, T. and Kurkhuli, G. 2015, SPIE 9652.

Astronomy & Astrophysics (Caucasus) 2, (2016) (47-58)

LINE TRANSPORT IN TURBULENT ATMOSPHERE

A. Nikoghossian

NAS RA V. Ambartsumian Byurakan Astrophysical Observatory
Byurakan 0213, Aragatsotn province, Armenia, E-mail: nikoghoss@yahoo.com

Received October 24, 2016; revised December 1, 2016

Abstract

We consider the spectral line transfer in turbulent atmospheres with a spatially correlated velocity field. Both the finite and semi-infinite media are treated. In finding the observed intensities we first deal with the problem for determining the mean intensity of radiation emerging from the medium for a fixed value of turbulent velocity at its boundary. New approach proposed in solving this problem is based on invariant imbedding technique which yields the solution of the proper problems for a family of media of different optical thicknesses and allows tackling different kinds of inhomogeneous problems. The dependence of the line profile, integral intensity and the line width on the mean correlation length and average value of the hydrodynamic velocity is studied. It is shown that the transition from a micro-turbulent regime to a macro-turbulent one occurs within a comparatively narrow range of variation in the correlation length. The diffuse reflection of the line radiation from a one-dimensional semi-infinite turbulent atmosphere is examined. In addition to the observed spectral line profile, statistical averages describing the diffusion process in the atmosphere (mean number of scattering events, average time spent by a diffusing photon in the medium) are determined. The dependence of these quantities on the average hydrodynamic velocity and correlation coefficient is studied.

Key words: Radiative transfer, line formation, turbulent atmosphere, correlation length

1. Introduction

Turbulence is known as one of the most widespread phenomena in the universe taking place on all macroscopic scales – from twinkling of starlight and distortion of images of terrestrial objects, from occurrence in planetary and stellar interiors and atmospheres to galactic and even meta-galactic scales. In latter case turbulence provides the chaotic environment in which the galaxies and clusters of galaxies are formed. From the laboratory scale to that of clusters of galaxies span of scale is of order of 10^{25}. Some theories suggest that turbulent fluxes are surmised in appearing perturbations in the form of vortexes, which give rise rotation phenomena in the universe. Finally, it is proposed that turbulence is responsible for the present form of the universe.

In studying turbulence in astrophysical context, one generally encounters two kinds of problems. One of them is construction of an adequate model for describing the observed picture of chaotic movements in the radiating medium. The problem is rather complex since the nature and manifestations of such movements may differ drastically dependent on the values of Reynold's number. Applying the developed model one encounters the second problem that is finding the feature of the spectrum expected to observe. The satisfactory agreement of results of the developed radiative transfer theory with observational data allows us to hope to estimate eddy sizes and some other characteristics of the radiating turbulent medium.

Historically, the non-thermal mechanism due to hydrodynamic motions was invoked in order to achieve satisfactory agreement between the theoretical and observed profiles and equivalent widths of spectral lines formed in stellar atmospheres, although no directly observable proofs existed for the hydrodynamic nature (in the customary sense) of this phenomenon. However, the phenomenon of granulation, which is directly observable in the sun's photosphere, as well as motion on different

scales in solar prominences, suggests that this kind of phenomenon is to be expected in other stars as well. This arises the question of how random variations in the velocity field within a radiating atmosphere affect the observed spectra. The present study covers some of the most important aspects of this problem.

2. The problem of meso-turbulence

As it is known, the hydrodynamic characteristic of turbulent motions is the correlation coefficient along the direction of propagation of a ray. It depends significantly on the type of turbulence and is determined by the degree of correlation between the variations in the velocity field at different points in the medium. The characteristic parameter which describes the correlation on the average is correlation length Λ. In the two limiting cases of $\Lambda \to 0$ and $\Lambda \to \infty$, the problem of spectral line formation is greatly simplified, so these cases have been most often invoked by astrophysicists in the course of interpreting the observational spectra. For values of smaller than the photon mean free path, random variations in the hydrodynamic velocity at nearby points of the medium are essentially independent of one another. In the limit of $\Lambda \to 0$, the velocities of the motions are independent on an atomic level so that in calculating the profile of an observed line only the Doppler shifted absorption coefficient in the line is averaged over the velocity. This limiting case corresponds to micro-turbulence. In the opposite limiting case of $\Lambda \to \infty$, known as macro-turbulence, the hydrodynamic velocities at all points vary in unison, so that the mean profile of the spectrum line is a superposition of profiles that are shifted by different amounts, as happens when the radiating object is rotating.

Evidently, the micro- and macro-turbulence models are only approximations and do not provide a clear idea on the effect of turbulent motions in the case of arbitrary sizes for the turbulence cells. This intermediate case, often referred to as meso-turbulence (Gray, 1978), has been examined by many authors. Here we mention only a few papers by French and German theorists during the 1970's and 1980's, when this topic underwent a rapid development. An early paper by Traving (1964) (see also Humdt, 1973) dealt with a discrete model problem in which absorption by atoms was replaced by exponential absorption on the part of solid, independently moving turbulence cell with finite, but fixed dimensions. This approach was developed further (Frish, 1975; Frish H. & Frish U., 1976) under the assumption that the sizes of the cells can vary randomly, with the interface points distributed in space according to the Poisson law (the so-called Kubo-Anderson process (Bharucha-Reid, 1960)). With some simplifying assumptions, a closed expression was obtained for the statistical mean profile of a spectral line under LTE. A fundamentally different method has been developed (Gail &Sedlmayr, 1974; Schmid-Burgk, 1975) as a continuum analog of the problem. It reduces to considering Uhlenbeck-Ornstein process (Gail et al., 1975) with a Gaussian velocity distribution. The result is Fokker-Planck type equations for the joint distribution function of the velocities and the radiated intensity in the line. These equations are rather complicated and are solved numerically. In fact, both of the above approaches are approximate and are not consistent with one another.

3. Invariant imbedding. LTE atmosphere

Now we briefly reproduce the approach proposed by the author (Nikoghossian, 2007a) which uses the method of invariant imbedding. Consider a one-dimensional atmosphere of finite optical thickness τ_0 measured at the center of a spectral line in the absence of hydrodynamic motions. We shall assume that the medium contains energy sources of power $B(\tau)\varpi(x)$, where, $\omega(x)$ is the profile of the absorption coefficient and β is the ratio of the absorption coefficient in the continuum to that at the line center. The quantity $B(\tau)$ plays the role of a source function and is related to the Planck function. We shall assume that a steady state, homogeneous and isotropic turbulence has developed in the atmosphere so that the hydrodynamic velocity vector $\boldsymbol{v}$ is a random function that depends on the depth, while the mean characteristics of the velocity field are independent of the depth

in the atmosphere (Batchelor, 1970). In addition, let us suppose that the probability law according to which the velocity takes one or another value is also independent of the depth. Finally, we assume that the variations in velocity inside the medium are correlated with one another. We are interested in the mean intensity of radiation, $\langle I(\tau_0, x)\rangle$, emerging from the boundary $\tau = \tau_0$ (Fig. 1)

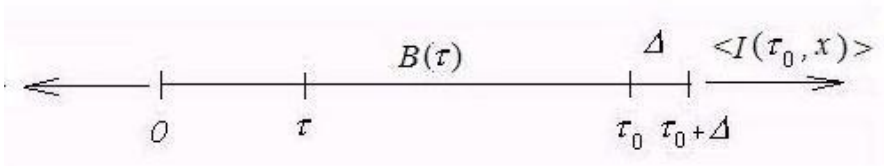

Fig.1. The schematic picture of radiating one-dimensional turbulent atmosphere

We start with introducing function $\langle I(\tau_0, x, u)\rangle$ standing for the mean intensity of the radiation emerging from theatmosphere with frequency *x* under condition that the hydrodynamic velocity at the boundary of the medium is equal to *u*, the latter being measured in units of thermal velocity. Effect of the radiation on the velocity field will be neglected. We denote by $G(u,u',\rho(l))\,\mathrm{d}u$ the probability that if the value of velocity at the optical depth τ' is u', then at the depth τ it will lie within the interval *u*, *u* + d*u*. Because of the uniformity of the process, the correlation coefficient ρ depends only on the distance between the points, $l = |\tau - \tau'|$. In the simplest case of spectral lines under LTE, one can use the rules of addition for statistical mean intensities developed in (Ambartsumian, 1941, 1944; Sobolev, 1958) to write for the mean intensity resulting from augmentation of the initial turbulent atmosphere of thickness τ_0 by the small layer Δ possessing the same properties

$$\langle I(\tau_0+\Delta, x, u)\rangle = \mathrm{e}^{-\varpi(x-u)\Delta}\int_{-\infty}^{\infty} G(u,u',\rho(\Delta))\langle I(\tau_0, x, u')\rangle\,\mathrm{d}u' + B(\tau_0)\left[1-\mathrm{e}^{-\varpi(x-u)\Delta}\right]. \quad (1)$$

This equation is crucial for deriving the equations for the random function $\langle I(\tau_0, x, u)\rangle$. Its solution allows to determine the unknown value of the statistical mean intensity $\langle I(\tau_0, x)\rangle$ from:

$$\langle I(\tau_0, x)\rangle = \int_{-\infty}^{\infty} P(u)\langle I(\tau_0, x, u)\rangle\,\mathrm{d}u\,, \quad (2)$$

where *P*(*u*) is the distribution law of turbulent velocities.

One may specify the law governing the variations in the non-thermal velocity at different depths by assuming that the process is Markovian and consider a Gaussian distribution in the plane. Then

$$G(u,u',\rho) = \frac{1}{u_t\sqrt{\pi(1-\rho^2)}}\exp\left(-\frac{(u-\rho u')^2}{u_t^2(1-\rho^2)}\right), \quad (3)$$

where $u_t = \sqrt{\pi}\langle u_{\mathrm{turb}}\rangle$ and $\langle u_{\mathrm{turb}}\rangle$ is the mean hydrodynamic velocity in units of thermal velocity. As it was proved in (Nikoghossian, 2007), there is the bilinear expansion

$$G(u,u',\rho) = \frac{1}{\alpha_0(u')}\sum_{k=0}^{\infty}\rho^k\alpha_k(u)\alpha_k(u'), \quad (4)$$

where

$$\alpha_k(u) = \left(2^k \pi u_t^2 k!\right)^{-1/2} \mathrm{e}^{-\left(\frac{u}{u_t}\right)^2} H_k\left(\frac{u}{u_t}\right), \tag{5}$$

and $H_k(u)$ are Hermite polynomials. Note that the functions $\alpha_k(u)$ represent an orthonormal set of functions with weight $\alpha_0(u)^{-1}$. For a uniform Markov process the correlation coefficient varies exponentially with the distance between the depths being $\rho(l) = \exp\left(-l/\Lambda\right)$, where $l = |\tau - \tau'|$ and Λ is the mean correlation length. In fact, if we consider three depth such that $\tau_1 > \tau_2 > \tau_3$ and take $l_1 = |\tau_1 - \tau_2|$ and $l_2 = |\tau_2 - \tau_3|$, then, using the expansion of the function *G* (see Nikoghossian, 2007), it is easy to show that

$$G\left(u,u',\rho\left(l_1+l_2\right)\right) = \int_{-\infty}^{\infty} G\left(u,u'',\rho\left(l_2\right)\right) G\left(u'',u',\rho\left(l_1\right)\right) du'' . \tag{6}$$

This equation is essentially the Kolmogorov-Chapman relation for diffusion Markov processes and expresses the multiplicative property of the transition probability for the process (in this case, the conditional velocity distribution function). Of two ways proposed in (Wigner, 1959) to find $\left\langle I\left(\tau_0,x,u\right)\right\rangle$ we adopt reducing the problem to the integral equation

$$\left\langle I\left(\tau_0,x,u\right)\right\rangle = \int_{-\infty}^{\infty} \varpi\left(x-u'\right)\mathrm{d}u' \int_0^{\tau_0} K\left(\tau_0 - t,u,u'\right)\left[B(t) - \left\langle I\left(t,x,u'\right)\right\rangle\right]\mathrm{d}t , \tag{7}$$

where

$$K\left(\tau,u,u'\right) = \sum_{n=0}^{\infty} \frac{\alpha_n(u)\alpha_n(u')}{\alpha_0(u)} \mathrm{e}^{-\frac{n}{\Lambda}\tau} . \tag{8}$$

In two limiting cases of macro and micro-turbulence we arrive at known results. Indeed, if $\Lambda \to \infty$, and $K\left(\tau,u,u'\right) \to \delta\left(u-u'\right)$, Eq. (7) yields after some simple algebra

$$\left\langle I\left(\tau_0,x,u\right)\right\rangle = \int_0^{\tau_0} B(t)\,\mathrm{e}^{-\varpi(x-u)(\tau_0-t)}\varpi\left(x-u\right)\mathrm{d}t , \tag{9}$$

and keeping in mind that $P(u) = \alpha_0(u)$, we finally obtain

$$\left\langle I\left(\tau_0,x\right)\right\rangle = \int_{-\infty}^{\infty} \alpha_0(u)\left\langle I\left(\tau_0,x,u\right)\right\rangle \mathrm{d}u . \tag{10}$$

In the opposite case of $\Lambda \to 0$ and $K\left(\tau_0,u,u'\right) \to \alpha_0(u)$ so that $\left\langle I\left(\tau_0,x,u\right)\right\rangle$ does not depend on *u* and coincides with the requisite quantity $\left\langle I\left(\tau_0,x\right)\right\rangle$. Finally, we obtain

$$\left\langle I\left(\tau_0,x\right)\right\rangle = \int_0^{\tau_0} B(t)\,\mathrm{e}^{-\gamma(x)(\tau_0-t)}\gamma(x)\mathrm{d}t , \tag{11}$$

where

$$\gamma(x) = \int_{-\infty}^{\infty} \alpha_0(u)\varpi\left(x-u\right)\mathrm{d}u . \tag{12}$$

Solution of Eq. (7) for intermediate values of Λ allows to study the dependence of the line profile, integral intensity, and width on the mean correlation length and the average value of the non-thermal velocity

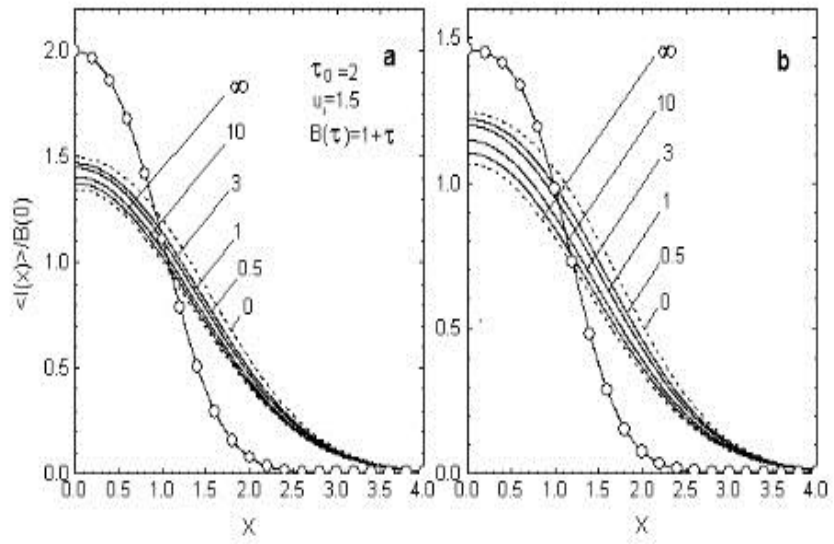

Fig.2. The effect of the mean hydrodynamic velocity and mean correlation length on the profiles of a spectral line formed at the boundaries τ_0 (a) and 0 (b) of a turbulent atmosphere of optical thickness $\tau_0 = 2$ with non-uniformly distributed primary energy sources. The curves with circles represent the line profiles in the absence of turbulence.

The effect of turbulent motions on the form of the spectral line profile is shown in Fig. 2. We see that that the turbulence in the atmosphere broadens the line profile for any sizes of eddies while the extent of this effect differs in passing from micro- to macro-turbulence. The comparison of two limiting regimes implies that the observed profiles for micro-turbulence are brighter as compared to those in the opposite limiting case, so that macro-turbulence favors thermalization of radiation in the medium much better than the other regimes of turbulence. We conclude also that this effect is more

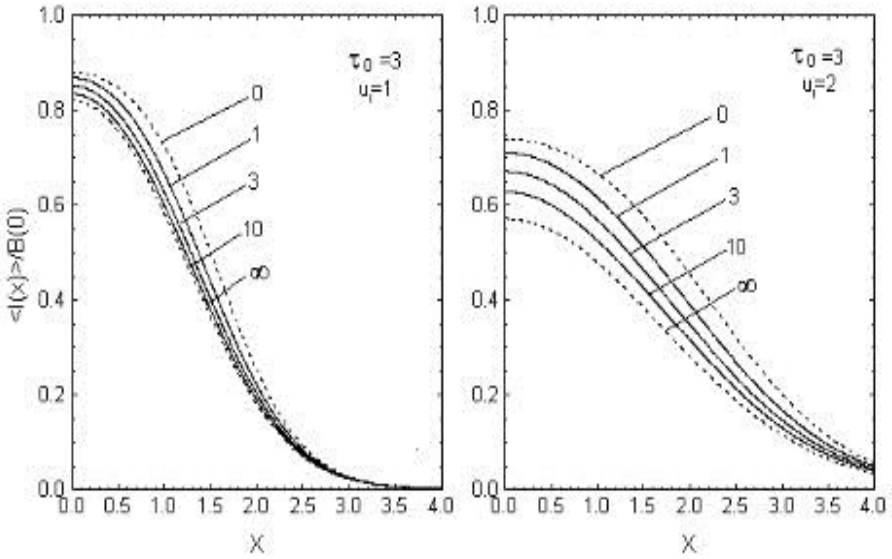

pronounced at the boundary $\tau = 0$, where the produced energy is less.

Fig.3. Profiles of spectral lines formed in a turbulent homogeneous atmosphere of optical thickness $\tau_0 = 3$ for different values of the mean hydrodynamic velocity.

Fig.3 shows that the width of the bundle of profiles depends essentially on the mean value of hydrodynamic velocity. In other words, the difference between macro- and micro-turbulent regimes is the more essential, the higher the turbulent velocity.

Solution of the spectral line formation problem for intermediate regime of meso-turbulence gives an idea of transition between different regimes of turbulence dependent on correlation length, i.e., on the size of eddies. Fig.4 demonstrates this transition for integral intensities in the case of inhomogeneous atmosphere of optical thickness $\tau_0 = 1$ and different value of hydrodynamic velocity. The left and right panels exhibit this effect for boundaries $\tau = \tau_0$ and $\tau = 0$, We see that there is fairly narrow range of correlation lengths variations $\left(-0.5 \le \log\Lambda \le 0.5\right)$ where the meso-turbulence takes place. The similar result can be obtained in considering this effect for FWHM of lines (Nikoghossian 2007a).

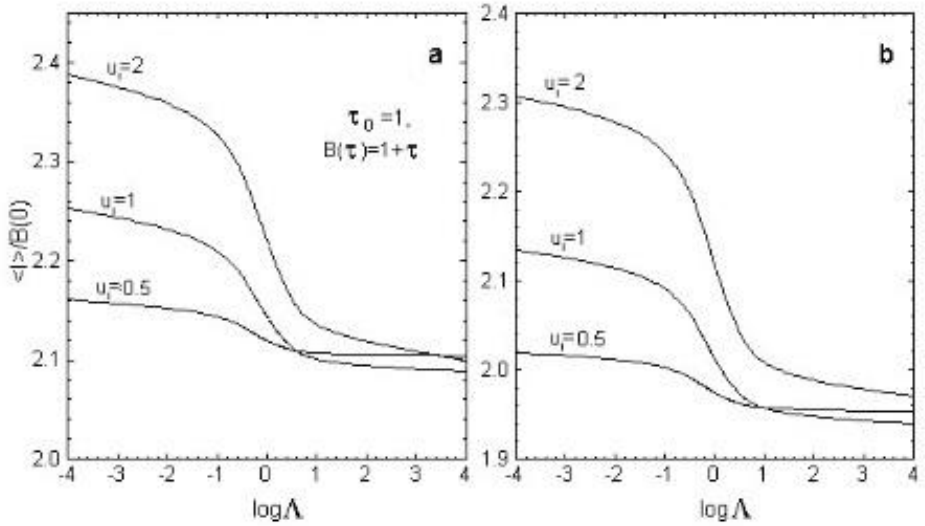

Fig.4 . The integral intensities of spectral lines formed at the boundaries τ_0 (left panel) and 0 (right panel) of a turbulent atmosphere of optical thickness $\tau_0 = 1$ for energy sources varying linearly with depth $B(\tau) = 1 + \tau$.

4. Invariant imbedding. NLTE lines.

The next important point is to find out the influence of scattering processes in turbulent NLTE media on the observed profiles of spectral lines. Taking multiple scattering effects into account makes the radiative transfer problem more complicated due to appearance of reflected beams. An additional difficulty arises in the case of a turbulent atmosphere: a diffusing photon can, in general, encounter one and the same layer with different values of the hydrodynamic velocity (Frisch, 1975; Magnan 1975). This can happen, for example, in a rarefied medium with a high optical thickness with comparatively high hydrodynamic velocities. This phenomenon is sometimes neglected, and this makes it somewhat easier to solve the problem. It is however, obvious that the validity of this approximation should be checked in every specific case. We assume also that the value of the non-thermal velocity at a given point in the atmosphere does not change during the time taken by atom for re-radiation of the absorbed photon. Our goal in this section is to determine how and over what ranges the different characteristics of radiative diffusion (mean number of scattering events, average time of a photon travel in the medium) vary during the transition between the two limiting regimes of macro- and micro-turbulence.

As in section 3, we consider a one-dimensional absorbing and scattering turbulent atmosphere of finite optical thickness τ_0 . Now we suppose that it is source-free and is illuminated from outside from the site of boundary τ_0 . We are interested in the averaged properties of reflection and transmission of the medium, or, in other words, in the profiles of lines observed at both boundaries of it. Here,

again, we use the invariant imbedding technique and first we find the required optical properties of turbulent atmosphere for fixed value of hydrodynamic velocity at boundary τ_0. The used method allows treating any kind of non-homogeneities regarding the depth variation of parameters specifying properties of the elementary event of scattering (the scattering coefficient and frequency redistribution law denoted here by λ and $\mathbf{\Gamma}$, respectively) as well as the properties of turbulent motions like the correlation length, mean thermodynamic velocity and so on.

For convenience, we use the vector-matrix notations and introduce matrices $\mathbf{R}$ and $\mathbf{Q}$ to denote the reflectance and transmittance of the medium illuminated from the site of boundary τ_0 for the fixed boundary value of hydrodynamic velocity *u*. The elements of these matrices evidently are the frequencies of incident and correspondingly reflected and transmitted photons.

Invariant imbedding technique leads to the following matrix differential equations

$$\frac{d\mathbf{R}}{d\tau_0} = \mathbf{\Phi}_\Lambda \mathbf{R}(u,\tau_0) - \left[\mathbf{m}(u)\mathbf{R}(u,\tau_0) + \mathbf{R}(u,\tau_0)\mathbf{m}(u)\right] + \mathbf{n}(u) + \mathbf{R}(u,\tau_0)\mathbf{n}(u)\mathbf{R}(u,\tau_0), \tag{13}$$

$$\frac{d\mathbf{Q}}{d\tau_0} = \mathbf{\Phi}_\Lambda \mathbf{Q}(u,\tau_0) - \mathbf{Q}(u,\tau_0)\left[\mathbf{m}(u) - \mathbf{n}(u)\mathbf{R}(u,\tau_0)\right], \tag{14}$$

with initial condition $\mathbf{R}(u,0) = 0$ and $\mathbf{Q}(u,0) = \mathbf{I}$.

Here $\mathbf{\Phi}_\Lambda = \left.\frac{\partial \mathbf{G}}{\partial l}\right|_{l=0}$, $\mathbf{n}(u) = \frac{\lambda}{2}\mathbf{\Gamma}(u)$, $\mathbf{m}(u) = \boldsymbol{\omega}(u) - \mathbf{n}(u)$, $\boldsymbol{\omega}(u) = \boldsymbol{\alpha}(u) + \beta$. $\mathbf{\Gamma}(u)$ is the frequency redistribution matrix, the elements of which are frequencies of incident and scattered photons being displaced by *u*. The diagonal matrix $\boldsymbol{\alpha}(u)$ is the line absorption profile with frequency displaced by *u*. In the case of macro-turbulence $\Lambda \to \infty$ for any *l*, and $\mathbf{\Phi}_\Lambda = 0$, $G(u,u',\rho(l)) = \delta(u-u')$

$$\langle \mathbf{R}(\tau_0) \rangle = \int_{-\infty}^{\infty} \mathbf{R}(u,\tau_0)\alpha_0(u)\,du. \qquad \langle \mathbf{Q}(\tau_0) \rangle = \int_{-\infty}^{\infty} \mathbf{Q}(u,\tau_0)\alpha_0(u)\,du. \tag{15}$$

Finally, in limiting case of micro-turbulence $\Lambda = 0$ and $G(u,u',\rho(l)) = \alpha_0(u')$ so that

$$\frac{d\langle \mathbf{R} \rangle}{d\tau_0} = -\left[\langle \mathbf{m} \rangle \langle \mathbf{R}(\tau_0) \rangle + \langle \mathbf{R}(\tau_0) \rangle \langle \mathbf{m} \rangle\right] + \langle \mathbf{n} \rangle + \langle \mathbf{R}(\tau_0) \rangle \langle \mathbf{n} \rangle \langle \mathbf{R}(\tau_0) \rangle, \tag{16}$$

$$\frac{d\langle \mathbf{Q} \rangle}{d\tau_0} = -\langle \mathbf{Q}(\tau_0) \rangle \left[\langle \mathbf{m} \rangle - \langle \mathbf{n} \rangle \langle \mathbf{R}(\tau_0) \rangle\right], \tag{17}$$

with $\langle \mathbf{R}(0) \rangle = 0$ $\langle \mathbf{Q} \rangle(0) = \mathbf{I}$. Under $\langle \mathbf{m} \rangle$ and $\langle \mathbf{n} \rangle$ we mean these quantities averaged over all boundary values of non-thermal velocity.

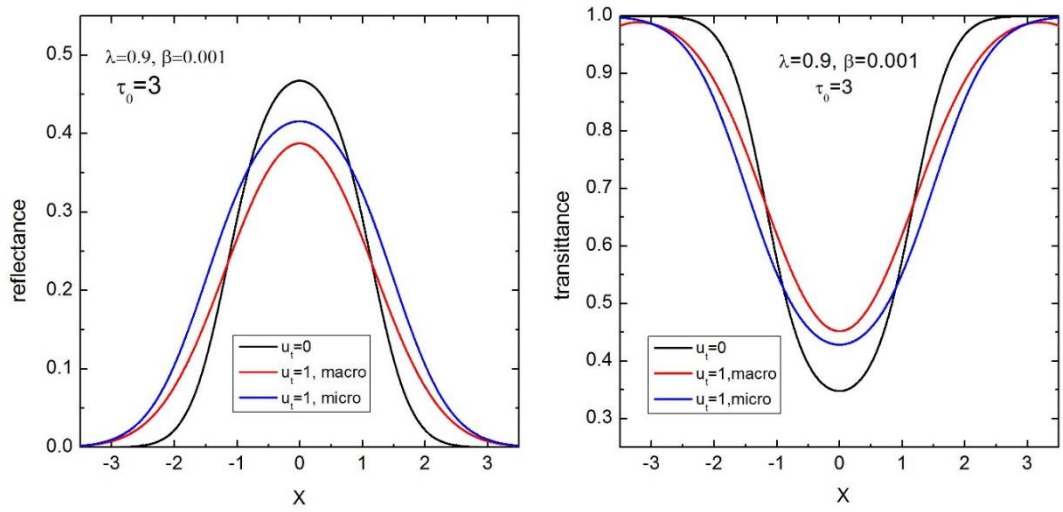

Fig.5. Reflection and transmission coefficients of an absorbing and scattering atmosphere of optical thickness $\tau_0 = 3$ in the absence of turbulence, as well as in the cases of the developed macro- and micro-turbulence

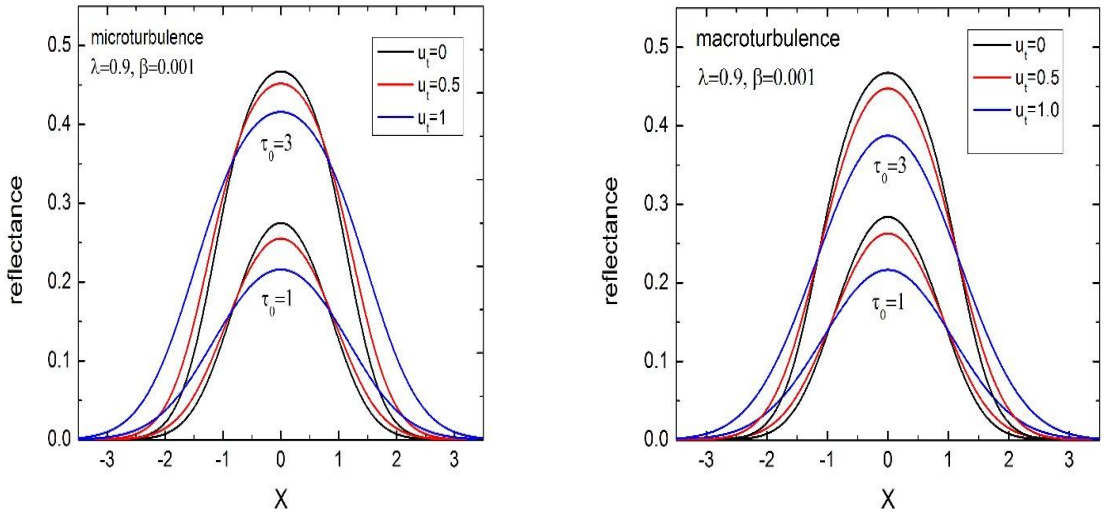

Fig.6. Reflection coefficients of atmospheres of different thicknesses in the case of micro- (left) and macro-turbulence (right) for indicated values of the mean hydrodynamic velocity

Some typical examples of numerical solution of presented matrix equations for complete redistribution over frequencies are shown in Figs. 5-7. It is seen that in both limiting cases the turbulence leads to broadening of profiles of the observed spectral lines. However, as in the LTE case, this effect is more significant for micro-turbulence. In both regimes the reflected and transmitted profiles exceed those for macro-turbulence within practically entire frequency range (Fig.5). This implies that the micro-turbulent atmosphere is relatively more reflective, i.e. brighter and opaque.

Fig.6 illustrates the dependence of the reflection lines profiles on the mean value of hydrodynamic velocity and optical thickness. It is seen that the dissimilarity between the line profiles in two limiting regimes of turbulence is greater the higher the hydrodynamic velocity and opacity of the atmosphere. A typical example of the reflection lines profiles observed at $\tau = \tau_0$ when one of parameters specifying the elementary event of scattering λ varies with depth in the medium as $\lambda(\tau) = 1/(1 + ae^{\tau})$ covering the range approximately from 1 to 0.33 is shown in Fig.7.

We are confined by presenting only the profiles formed at $\tau = \tau_0$, where the scattering ability of the atmosphere is smallest. Besides the effects described above, we observe a large discrepancy between two regimes of turbulence, especially discernible in the center of the lines.

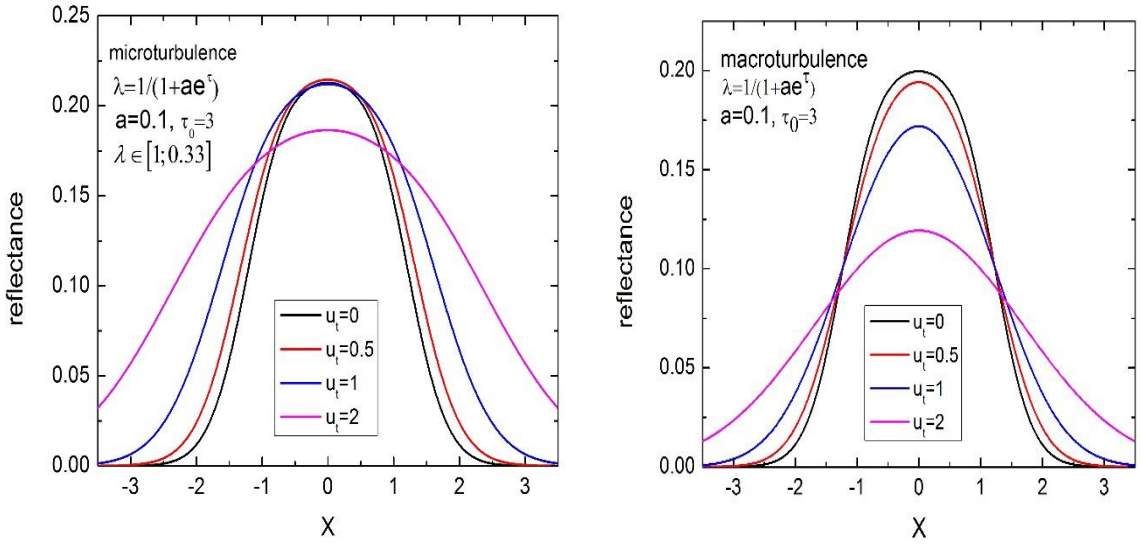

Fig.7. Reflection coefficients of atmospheres of optical thickness $\tau_0 = 3$ in the case of micro- (left panel) and macro-turbulence (right panel) for variable scattering coefficient.

5. Semi-infinite absorbing and scattering turbulent atmosphere

To gain further insight of the role of eddy-sizes, we present here some results obtained in considering the problem of diffuse reflection from a turbulent semi-infinite atmosphere (Nikoghossian 2007b).

Fig. 8 shows profiles of a spectral line formed by diffuse reflection from micro- and macro-turbulent semi-infinite atmospheres for different values of the mean hydrodynamic velocity u_t. We arrive at the known result of a constant equivalent width for the macro-turbulent regime. On the other hand, as the left graph shows, in the micro-turbulent regime the intensity at the line center remains essentially constant, while the half width and equivalent width of the line increase rapidly as the mean hydrodynamic velocity increases. The behavior of the line profiles does not change qualitatively for other values of the scattering coefficient λ. It confirms the abovementioned conclusion on the more reflective ability of the micro-turbulent atmosphere.

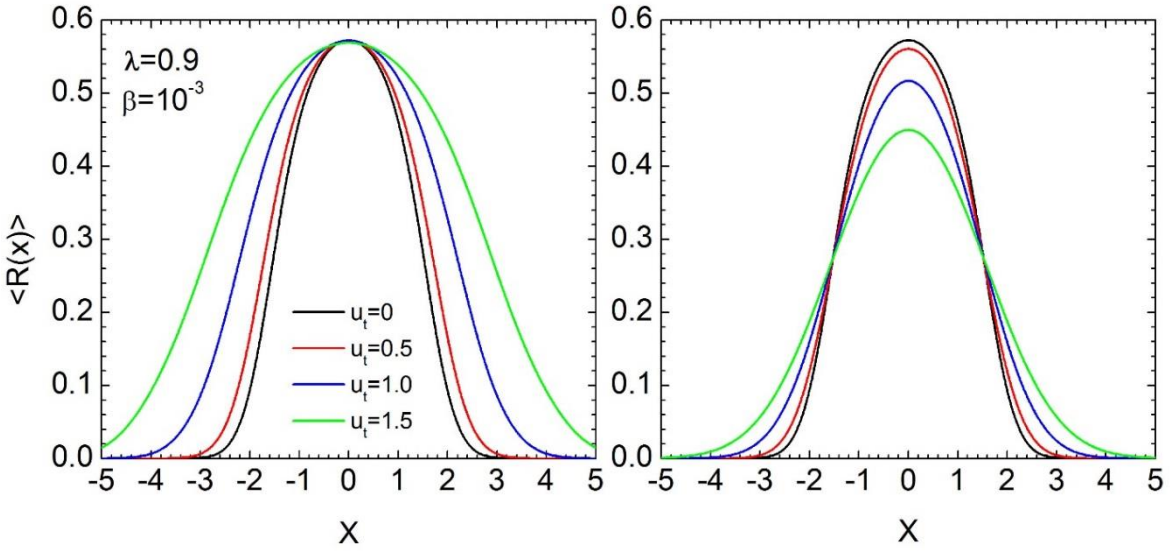

Fig. 8. Profiles of lines formed during reflection from semi-infinite micro-turbulent (left) and macro-turbulent (right) atmospheres. The central intensity of a line formed by reflection from a micro-turbulent atmosphere essentially remains unchanged as the average non-thermal velocity increases. In the macro-turbulent regime, the equivalent width of the line does not change.

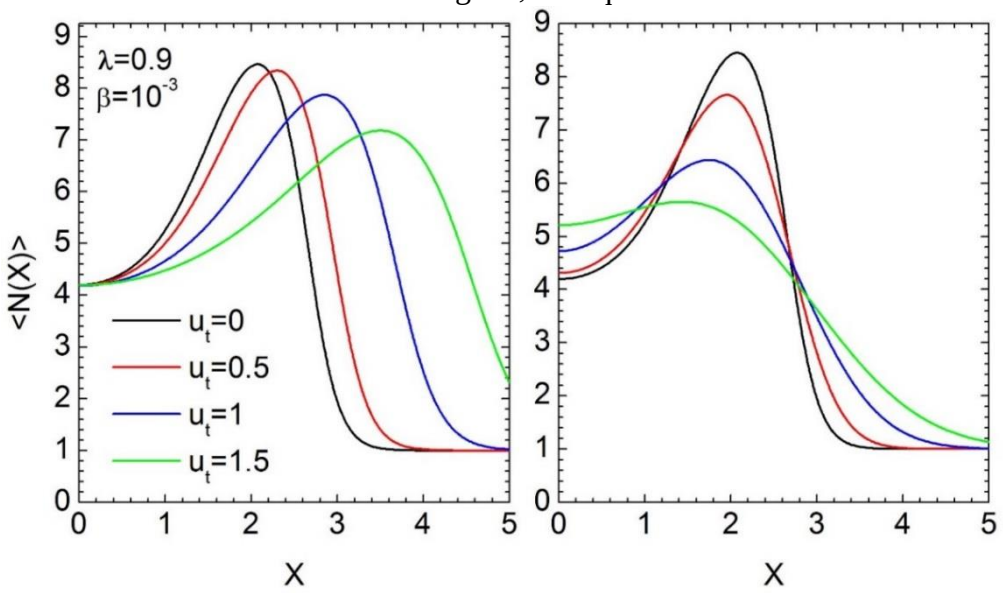

Fig. 9. Mean number of scattering events underwent by a photon during diffusion in an atmosphere with micro- (left) and macro-turbulence (right). True absorption in the continuum is also treated as scattering.

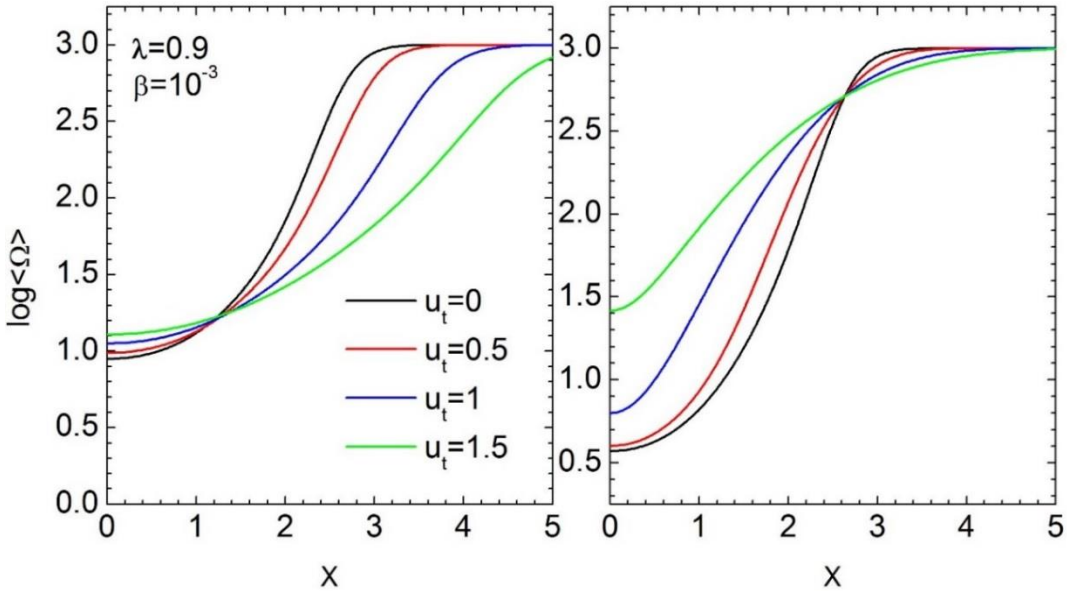

Fig. 10. Average time of the line photons travel in semi-infinite micro- (left) and macro-turbulent (right) atmospheres

One of important characteristics of radiation diffusion in any absorbing and scattering media is the mean number of scattering events $\langle N(x)\rangle$ underwent by a photon during the diffusion process before it undergoes true absorption and is thermalized in the medium or escapes it. We denote by $\langle \Omega(x)\rangle$ the average time spent in diffusing in the atmosphere (we neglect the time spent by an atom in an excited state). $\langle \Omega(x)\rangle$ is dimensionless and is measured in units of $1/nk_{\nu_0}c$, where n is the number of absorbing atoms per unit volume and k_{ν_0} is the absorption coefficient per atom at the line

center. In both the macro- and micro-turbulent regimes, these quantities can be found using the methods we have described in (Nikoghossian, 1984; 1986).

Figs. 9,10 illustrate the frequency behavior of the statistical mean values of $\langle N(x) \rangle$ and $\langle \Omega(x) \rangle$ obtained in (Nikoghossian 2007b) for different values of the mean hydrodynamic velocity. As a comparison these quantities are plotted for the case of no turbulence in the atmosphere. The different behavior of $\langle N(x) \rangle$ in these two regimes is discernible. Like the line profile, the mean number of scattering events at the central frequencies in the micro-turbulent atmosphere is similar to that in the absence of turbulence. At the same time, photons in the line wings are scattered more frequently in a turbulent atmosphere, although they spend less time in scattering there. Photons behave roughly the same way in the line wings in the macro-turbulent regime. At the central frequencies however, the number of scattering events and time of travelling in the medium are greater in this case than without turbulence. In addition, Figs. 8-10 show that in the far wings the size of the turbulent elements does not matter. On the other hand, we can see that the presence of turbulent motions has no effect on the asymptotic behavior of these statistical means. Physically this is understandable, since in the far wings both the number of scattering events and the photon diffusion time are not determined by the emergence from the atmosphere, but by true absorption in it. In particular, this time is greatest and equal to β^{-1}. It allows to judge the validity in given case of our earlier assumption of an invariant non-thermal velocity in the neighborhood of a given point at which a photon is repeatedly scattered.

6. Conclusions

We saw that the invariant imbedding technique in combination with the new approach based on preliminarily finding of the emerging intensity for a fixed boundary value of non-thermal velocity allows revealing the effect of turbulent motions on the line transport in both LTE and NLTE-atmosphere for arbitrary value of the correlation length. As it was expected, the turbulence broadens the line profiles, however, this occurs differently in the limiting cases of micro- and macro-turbulence. The greater observed line intensities, the less the mean correlation length, i.e. the emission lines formed in the presence of micro-turbulence are brighter as compared to those formed in macro-turbulent media. The absorbing and scattering micro-turbulent media are more reflective and opaque in the case of an atmosphere of finite optical thickness. This difference is more important, the higher the mean value of the hydrodynamic velocity and the greater the optical thickness. Transition from micro- to macro-turbulence occurs in the narrow range of Λ variations, predominantly in the vicinity of $\Lambda = 1$, i.e., when the eddy-sizes are of the order of the free mean path of the photons travel. The process of the photons diffusion in the medium also takes place differently depending on correlation coefficient. The photons in the line wings formed in the micro-turbulent atmosphere scatter much more than those in the presence of macro-turbulence, though the former spend less time in the medium.

It is important that the proposed approach yields a solution to the problem for a family of inhomogeneous atmospheres with different optical thicknesses, which, in its turn, makes it easy to determine the radiation field inside the turbulent medium. The approach can be generalized in various ways, in particular, it can be applied without significant changes to the case where the correlation length depends on position within the atmosphere.

References

Ambartsumian V.A., 1941, Uch. Zap. LGU, No.11,

Ambartsumian V.A., 1944, Dokl. Akad. Nauk SSSR, **43**, 106.

Batchelor G., 1970, The theory of homogeneous turbulence, Cambridge, Cambridge University Press.

Bharucha-Reid A.T., 1960, Elements of the theory of Markov processes and their applications, New York, McGraw-Hill.

Frish H., 1975, Astron. Astrophys., **40**, 267-276.

Frish H. & Frish U., 1976, Mon. Not. Roy. Astron. Soc., **175**, 157-175.

Gail H.P. & Sedlmayr E., 1974, Astron. Astrophys., **36**, 17-25.
Gail H.P., Sedlmayr E. &Traving G., 1975, Astron. Astrophys., **44**, 421-429.
Gray D.F., 1978, Sol. Phys., **59**, 193-236.
Hundt E., 1973, Astron. Astrophys., **29**, 17-21.
Magnan C., 1975, J. Quant. Spectrosc. Radiat. Transfer **15**, 979.
Nikoghossian A.G., 1984, Astrophysics, **21**, 527-537.
Nikoghossian A.G., 1986, Astrophysics, **24**, 89-99.
Nikoghossian A.G., 2007a, Astrophysics, **50**, 175-186.
Nikoghossian A.G., 2007b, Astrophysics, **50**, 391-403.
Schmid-Burgk J., Astron. Astrophys., **32**, 73-78.
Sobolev V.V., 1958, Izv. AN ArmSSR, **11**, 39.
Traving G., 1964, Z. Astrophys., **60**, 167-175.
Wigner E., 1959, Group Theory, New York, Academic Press.

Astronomy & Astrophysics (Caucasus) 2, (2016) (59-73)

MONITORING OF SOLAR ACTIVITY IN RADIO FREQUENCY RANGE

N. Ograpishvili, D. Maghradze, Sh. Makandarashvili, D. Japaridze

E. Kharadze Abastumani Astrophysical Observatory at the Ilia State University, 3/5 Cholokashvili str., 0162 Tbilisi, Georgia

Email: natela.oghrapishvili@iliauni.edu.ge

Abstract

This article is a study of the long-term observations of solar radio bursts, sunspots and chromospheric flares observed at Abastumani Astrophysical Observatory. The Hα filtergrams were obtained by using a chromosphere-photosphere telescope with the aid of an interference polarization filter and the radio bursts were obtained by using the radio telescope at the frequency of 210 MHz (λ=1.43m).

I. It was found that there is a correlation between the amplitudes of the radio bursts, the number of spots and theregions of the spots.
II. The main purpose of this work is to detect radio signals associated with flares. In most cases, the area of flare and its intensity reached their maxima almost simultaneously. As for the peak energy release, mostly, it reached its maximum at almost the same time or slightly earlier in the meter radio wavelength band than in the Hα line. The sequence of events in the optical and radiobands during the flares was obtained by using the method of epoch superposition.

Key words: Radio emission,radio bursts, sunspots, chromospheric flare

1. Introduction

Research of the solar activity is one of the most important problems of astrophysics. It is known that changes of solar activity level affect many different processes occurring in the Earth's atmosphere, causing ionosphere disturbances, geomagnetic storms, Aurora Polaris, disturbances of radio communication conditions and other events. Solar activity influence spreads in the lower layers of the Earth's atmosphere – the stratosphere and even in the troposphere layers, where the Earth's weather and climate form. These changes are among the most complex reasons initiating the climate condition fluctuations on the Earth. In order to predict conditions in different layers of the Earth's atmosphere and interplanetary space, first of all, it is necessary to provide forecast of solar activity events forming these conditions. In this sense, forecasting the characteristics of the solar activity level changing is a very interesting problem for Solar and Earth physicists, as well as for all researchers investigating theSun-Earth problems.

The studies of the solar radio emission play an important role in the research of the processes taking place in the sun. The comparisons of the radio frequency and optical data make a valuable contribution to our understanding of the physical processes taking place in the sun's atmosphere, and make it possible to study the processes taking place in the different layers of the solar atmosphere.

The advantage of radio observations is high resolution in the upper layers of the corona, since the propagation velocity of radio waves obviously depends on the density of the surrounding medium. This is especially true for the 210 MHz emission band, which corresponds to 1.43 m.

The comparison of data obtained in different spectral bands is an important method for studying various events in the sun's atmosphere. In the visible range, which contains a large portion of the sun's radiation, the variability of flares is very small. Our knowledge of solar activity has expanded

much as a result of improvements in and coordination of optical and radio frequency observations (Innes D. E., Kameron R. H., et al., 2011, Korolev O. S., et al., 1970, Korolev O. S., 1975 1976, Shibasaki K., Alissandrakis C. E., and Pohjolainen S., 2011).

Emissions at different wavelengths are produced at different depths of the solar atmosphere. Therefore, through changing the wavelength, it is possible to study the different depths of the sun's atmosphere. Our attention is drawn to the fact that the solar radio emission appears in two forms, "quiescent" and "sporadic."Their distinctive features are well known (Zucca P., Carley E. P., et al., 2012., Korolev O. S 1976, Makandarashvili Sh.S., 1962). As a rule, they are localized in active regions of the solar disk.

Flares are considered the main feature of the solar activity and are therefore, a major object of the study. The intensity ofsporadic radio emission at meter wavelengths can exceed the emission from the quiet sun by several thousand times(Hey J. S., 1946).

The radio emission from the quiet sun is thermal emission from the solar atmosphere. The power of this emission is estimated by using the temperature of the sun's corona. Radio emission from the perturbed sun is however, related to the features of the sun's surface layers (Pawsey J. L. and Bracewll R. N, 1955).It was found that thenoise bursts are associated with the large groups of spots in the photosphere, especially those located in the central part of the solar disk (Pawsey J. L., Payne-Scott R., and McCready L. L., 1946).

The probability of the radio emission increases when the area of the entire group is greater, as well as when the area of the largest spot in this group increases (Pawsey J. L. and Bracewll R. N, 1955).

Flares, like the background emission, have a high degree of polarization, up to 100% with a magnetic field that shows up either in the source region of the radio emission or as the radio waves propagate in the corona (Ryle M. and Vonberg D. D., 1948).

The duration of the noise bursts can range from a few hours to several days over a wide range of frequencies (50-300 MHz) (Chernov G. P., 1997). As a whole, it is this phenomenon observed at meter wavelengths, which leads to an increased levelof noise emission.

The relation of noise bursts to other solar features, such as flares, has been discussed in various ways. Someauthors assume that all chromospheric flares precede or take place at the same time as the noise storms (Dodson H. W., 1958).

Others believe that noise bursts are observed only when strong, second- or third-order chromospheric flares are observed on the sun (Fokker A. D., 1965), Ryle M. and Vonberg D. D., 1948, Shibasaki K., Alissandrakis C. E., and Pohjolainen S., 2011).

Dodson (DodsonH. W., 1958) and Dodson and Hedeman, (Dodson H. W. and Hedeman E. R., 1958, 1960)discovered that the flares coincide with or precede radio storms at 200 MHz (150 cm). These flares may have a complicated structure and some have been referred to as "multiple bursts." The characteristic feature of the flares associated with the radio bursts is a smoother rise to their maximum than for most of the other flares.

De Feiter, et al (De Feiter L. D., Fokker A. D., and Roosen J., 1959) point out that strong flares are usually accompanied by radio bursts at decimeter and/or meter wavelengths. Only an insignificant part of the less important flares produce distinctive radio signals. A correlation has been obtained through the identification of the recorded flares and the use of diagrams and spectrograms for these sources. Observations were made to detect the radio blackout and identify the features of a flare.

Swarup, et al. (Swarup G., Stone P. H., and Maxwell A., 1960) found that 60% of the fast (type III) radio bursts are coincident in time with solar flares. The coupled bursts usually occur between the onset and the maximum of a flare. It was also found that 25% of all solar flares are obviously related to fast bursts. Almost all slow bursts (type II) and continuous phenomena (type IV) are also associated with flares, but there is no distinct relationship between the radio storm bursts (type I) and the flares.

Radio emission from solar flares will require many unique diagnostic instruments to explain the energy release, plasma heating, particle acceleration, and transport of particles in the magnetized plasma (Bastian T. S., Benz A. O., and Gary D. E., 1998).

Based on radio, x-ray and magnetic field measurements of a solar active region in 1992 (including high resolution radio, x-ray, magnetographic and Hα observations), Vourlidas, et al., (1997) attribute the excess of the o-mode emission to the magnetic field configuration and the temperature inhomogeneities across the spot.

Krucker, et al. (Krucker S., Benz A. O., Bastian T. S., and Acton L. W., 1997) suggested that solar flares and SXR/radio phenomena have some common features.

Shibasaki, et al. (Shibasaki K., Alissandrakis C. E., and Pohjolainen S., 2011) have suggested that the solar radio emission provides valuable information about the structure and dynamics of the solar atmosphere above a temperature minimum. They have examined new observational and theoretical data on the quiet sun and active regions over the entire radio wavelength range from millimeters to dekameters. They tried to provide a maximally complete picture of the quiet sun and active regions with the aid of the radio regions. In fact, the radio range can give us as much information as the rest of the spectrum of the solar atmosphere.

A comparison of the radio fluxes at 10.7 cm with the number of solar spots for solar cycles 19-21 has shown that the values of the radio flux are related to the magnetic field associated with sunspots. Data on the radio flux at 10.7 cm and its relationship to the number of sunspots and other parameters were given for each of these cycles. These data showed that the radio flux at 10.7 cm appears to be stochastic for cycle 19 and chaotic for cycles 20 and 21 (Greenkorn R. A., 2012).

2. Observational data and method of measurement

2.1. Solar radio observations at meter wavelengths (λ=1.43 m, ν=210 MHz) have been made at Abastumani Astrophysical Observatory since 1957 using a solar radio telescope. We have used observational data from 1957-2008 that contain 5 solar cycles (maxima during 1957-1958,1969-1970, 1980-1981, 1990-1991, and 2000-2001).

The data are presented in the form of time dependences of intensity. Universal time and intensity in units of 10^{-22} W/m^{-2}Hz are plotted on the abscissa and ordinate, respectively. The internal noise is less than 0.01 times the signal from the quiet sun. When solar radio emission is recorded, the galactic background is subtracted. When a large burst of solar radiation with its intensity many times greater than the level for the quiet sun occurs, the sensitivity of the radiometer varies greatly.

Extensive data collected in recent years clearly indicate that there is a close relationship between the radio bursts and the sunspots or groups of spots. The groups of spots accompanying the solar radio bursts are often of E or F types (according to the conventional classification of sunspots). It has also been found that a spot or group of spots with the opposite polarity may be the source of a radio burst.

Some characteristics of radio bursts, such as their duration and intensity, are closely related to the 11-year solar activity cycle. These all vary with the changes in solar activity.

Here we pay particular attention to three cases from the set of data, which demonstrate a close relationship between the occurrence of radio bursts and the sun's activity cycle; we have compared these with optical observations.

Fig. 1 shows a plot of solar radio emission and an image of sunspots on December 24, 1973. This figure corresponds to the first type of radio emission [8], i.e., a radio burst produced in the active

regions of the sun and observed optically. On this day, the Wolf sunspot number reached 260, and the area of the sunspots was as high as $1.500 \cdot 10^{-3}$ of the solar hemisphere.

Fig. 2 shows a plot of the solar radio emission and an image of sunspots by July 27, 1981. The sunspots were observed with the photosphere-chromosphere telescope at Abastumani Astrophysical Observatory. The Wolfnumber was 170 and the overall area of the sunspots was $3.35 \cdot 10^{-3}$ in the units mentioned above.

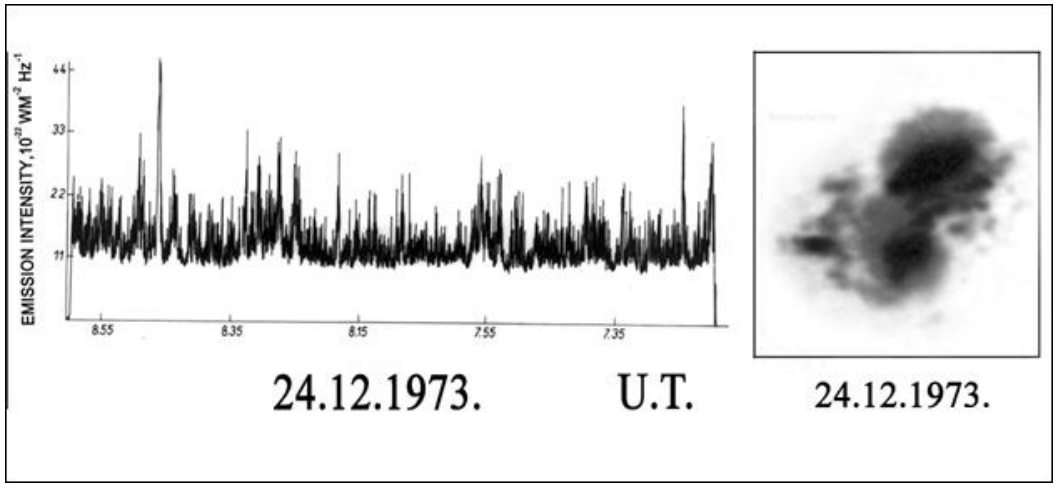

Fig. 1. A plot of the solar radio emission data obtained on December 24, 1973. The observation times are given on the abscissa (Universal time) and the intensity of the radio emission is plotted on the ordinate (in 10^{-22} W/m^{-2}/Hz. An image of sunspots on that date is shown on the right.

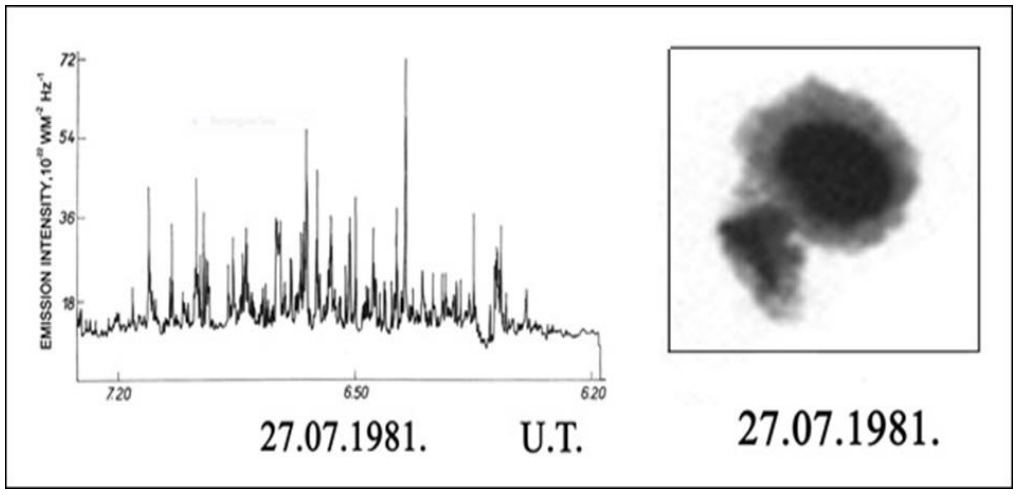

Fig.2. Solar radio emission and a picture of sunspots on July 27, 1981

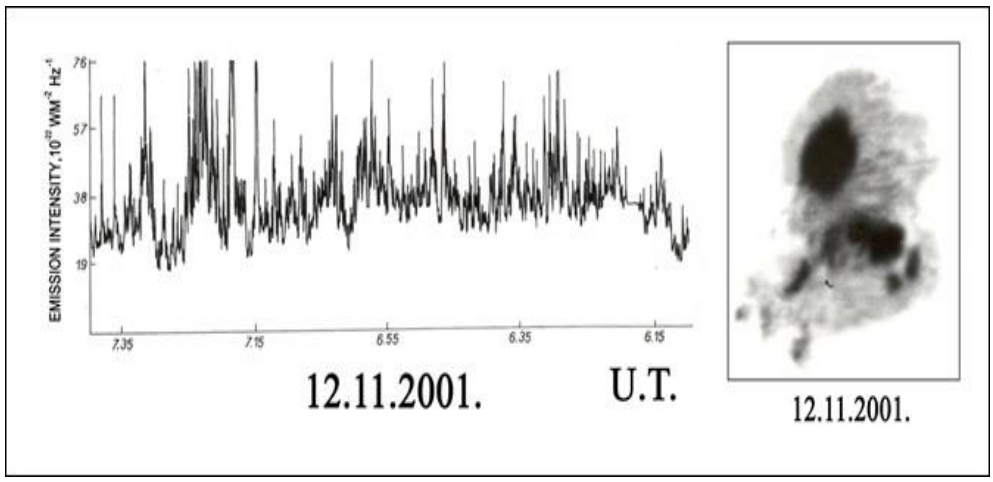

Fig. 3. Solar radio emission and a picture of sunspots on November 12, 2001

Fig. 3 shows a plot of the solar radio emission and an image of sunspots by November 12, 2001. The plots hows that this was a very intense radio burst and it fluctuated over 20-100x10^{-22} W/m^{-2}/Hz. On this day, an especially large group of sunspots was recorded on the eastern edge of the sun near the north pole.

2.2. In the present paper, we describe the plots of the development of chromospheric flares observed at Abastumani Astrophysical Observatory in 1973 using the chromosphere-photosphere telescope with an Hα-line interference-polarization optical filter with a passband of 0.5 E.

We studied the varying area and intensity of the flares, and when the energy release approached a maximum at the radio frequency, in the Hα line as well.

We have chosen 16 flares, mostly of scale 1*n*. The data are listed in Table 1. The longitudes are given in the heliocentric (λ) and Carrington (*L*) systems. The power of the flares was estimated on a four point scale: *f* faint, 1 normal, 2 powerful, and 3 most powerful. In the comments, *A* indicates an eruptive protuberance with a base at a heliocentric distance of at least 90°; *B*, an observed flare, which is the conclusion of a stronger one; *C*, a flare that was not visible ten minutes earlier, when there were no observations prior to the onset of the flare; *D* is a bright point; and *E* is two or more bright points (flaring simultaneously),φ is the latitude, λ is the longitude, and $L = L_0 + \lambda$ (with L_0 being the latitude of the central meridian of the sun).

In the following figures, the abscissa is time, the left ordinate is the intensity of the flares relative to the unperturbed chromosphere, and the right ordinate is the area of the flares in millionths of the solar disk area. If a flare consisted of several centers, then the intensities are given for eachcenter. However, the centers of the flares are difficult to distinguish by area, so we show theplots of the variation in the overall area for all the centers together. Each figure includes a photograph of the flare at the time of its maximum.

Table 1. Parameters of 16 observed flares

№	Date	Observation time			Location			Power	Remarks
		start	end	max	Φ	λ	L_0		to flares
1	19.06	$08^h\,03^m$	$08^h\,36^m$	$08^h\,17^m$	-02	-83	044	1n	D
2	06.07	07 28	07 45	07 32	-08	+14	280	1n	D
3	07.07	05 16	05 41	05 17	-06	+25	278	1n	B
4	07.07	06 09	06 43	06 13	+12	+23	276	1n	C
5	09.07	05 02	06 50	05 15	+11	+49	272	1n	D
6	10.07	07 00	07 09	07 04	+12	+64	277	1n	E

7	31.08	07 51	08 05	07 58	-17 -51 191	1n	D
8	02.09	05 35	06 35	05 41	-17 -56160	1n	C
9	11.09	06 55	07 20	07 01	-12 +58155	2n	B
10	11.09	07 58	08 27	08 04	-12 +41138	1n	B
11	27.09	11 07	11 38	11 11	-16 -48195	2n	B
12	29.09	04 07	05 06	04 50	+16 -57163	2n	B
13	26.11	07 04	07 13	07 06	-08 -15160	1n	D
14	16.12	05 35	06 20	05 50	-18 -88182	1n	A
15	23.12	07 51	08 15	07 58	-16 +36214	1n	A
16	24.12	10 36	10 59	10 46	-16 +51214	1n	C

On this chart, we can see the data from our observations.
A - Eruptional protuberance with its basis having the heliocentric distance of at least 90°.
B - Observable flare is the termination of a stronger one.
C- Flare was not visible ten minutes earlier when there was no observation prior to the beginning of the flare.
D- Bright spot.
E – Two or more bright spots (when lighten up simultaneously.)

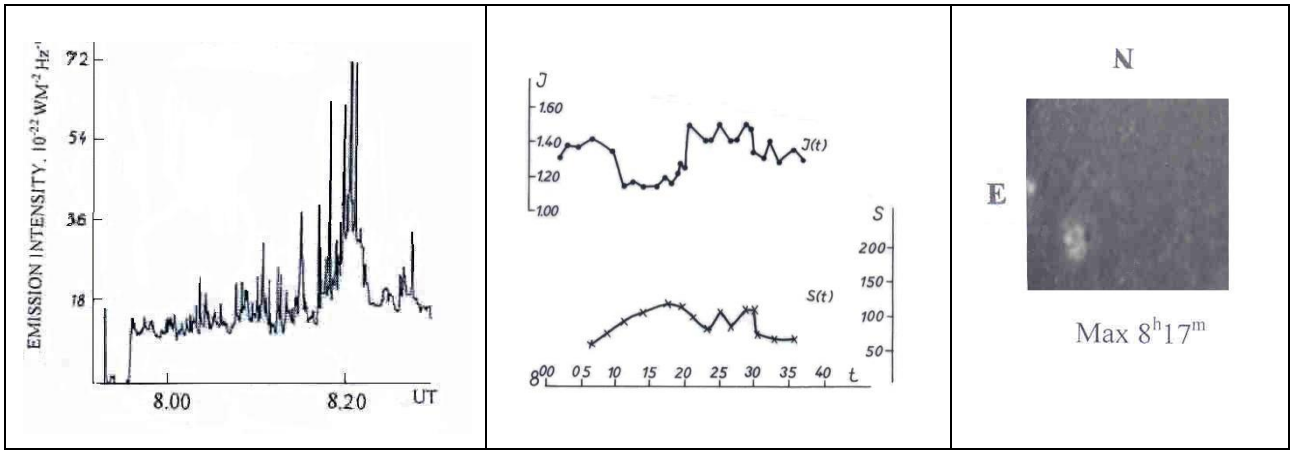

Figure 1. Observations of a flare № 1. In the figure on the left, we can see a change in the radio flow. The diagram in the center shows the intensity and area of the flare. The photo on the right is the observation of Hα line.

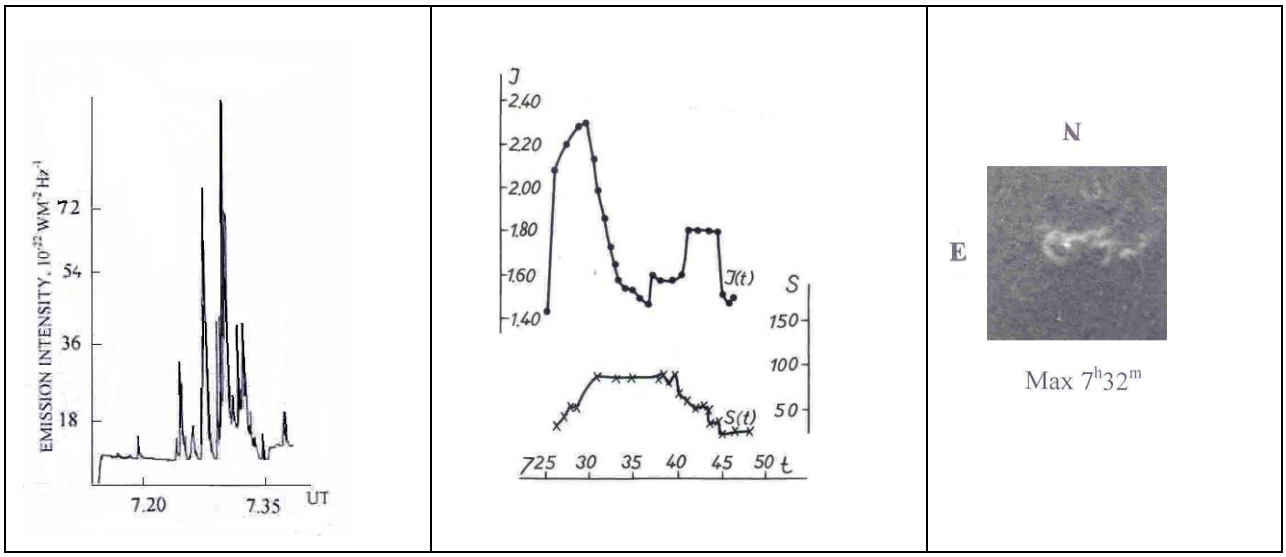

Figure 2. Observations of a flare № 2. In the figure on the left, we can see a change in the radio flow. The diagram in the center shows the intensity and area of the flare. The photo on the right is the observation of Hα line.

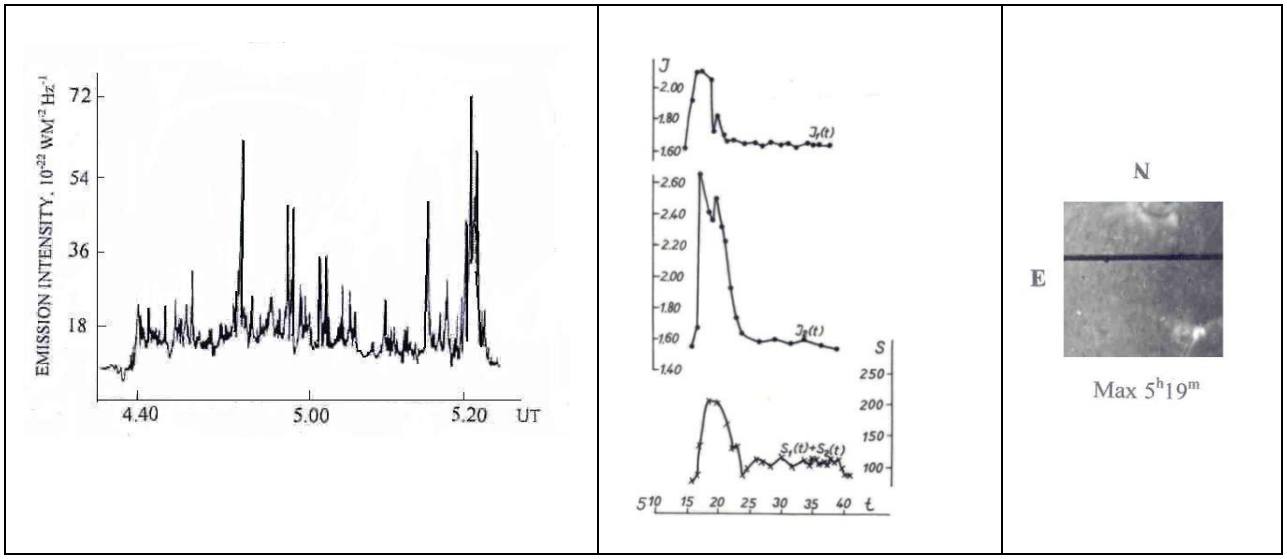

Figure 3. Observations of a flare № 3. In the figure on the left, we can see a change in the radio flow. The diagram in the center shows the intensity and area of the flare. The photo on the right is the observation of Hα line.

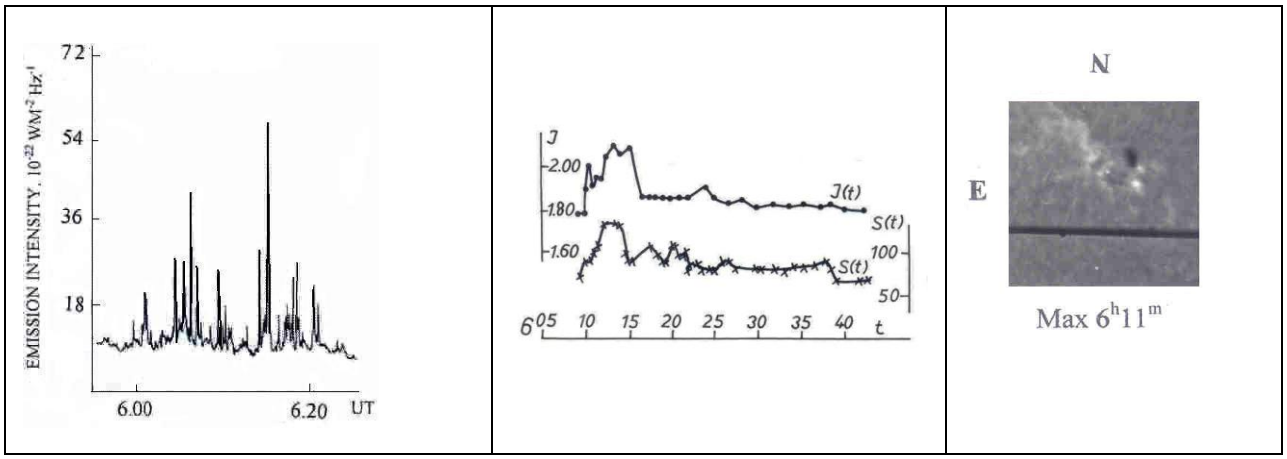

Figure 4. Observations of a flare № 4. In the figure on the left, we can see a change in the radio flow. The diagram in the center shows the intensity and area of the flare. The photo on the right is the observation of Hα line.

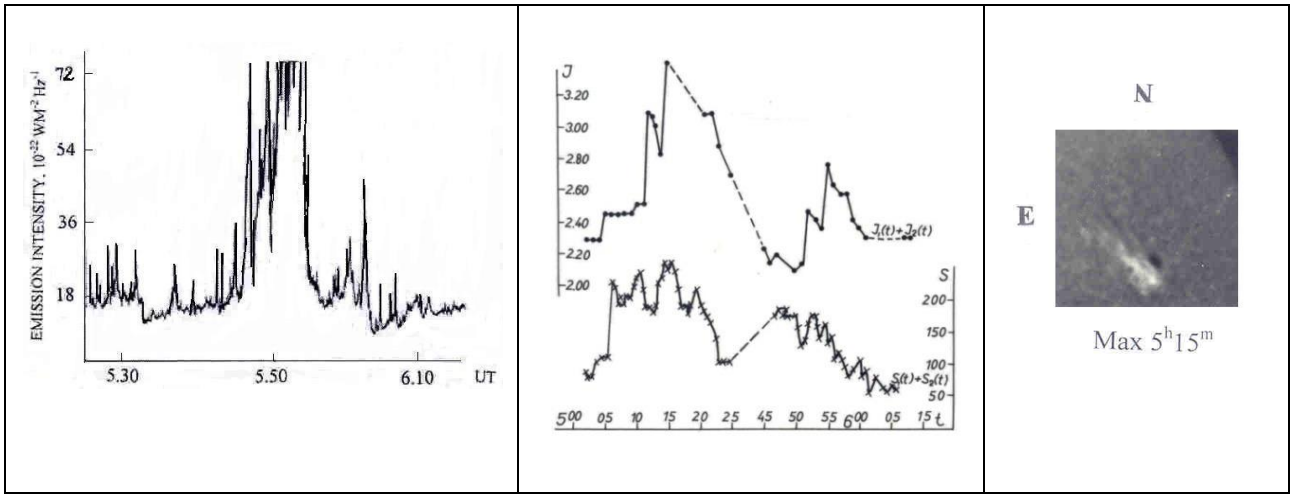

Figure 5. Observations of a flare № 5. In the figure on the left, we can see a change in the radio flow. The diagram in the center shows the intensity and area of the flare. The photo on the right is the observation of Hα line.

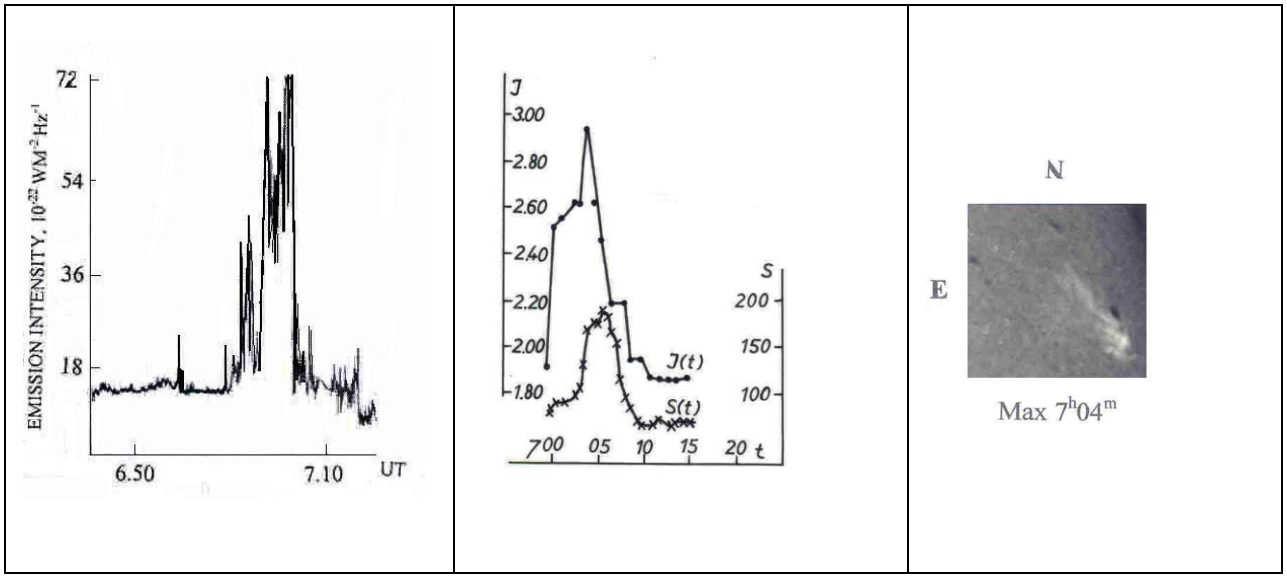

Figure 6. Observations of a flare № 6. In the figure on the left, we can see a change in the radio flow. The diagram in the center shows the intensity and area of the flare. The photo on the right is the observation of Hα line.

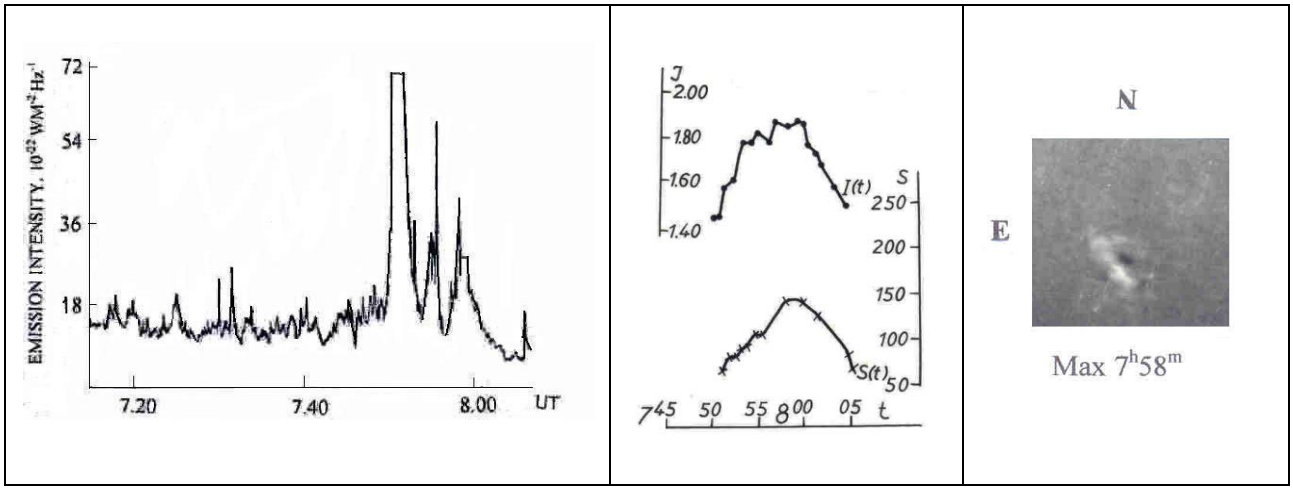

Figure 7. Observations of a flare № 7. In the figure on the left, we can see a change in the radio flow. The diagram in the center shows the intensity and area of the flare. The photo on the right is the observation of Hα line.

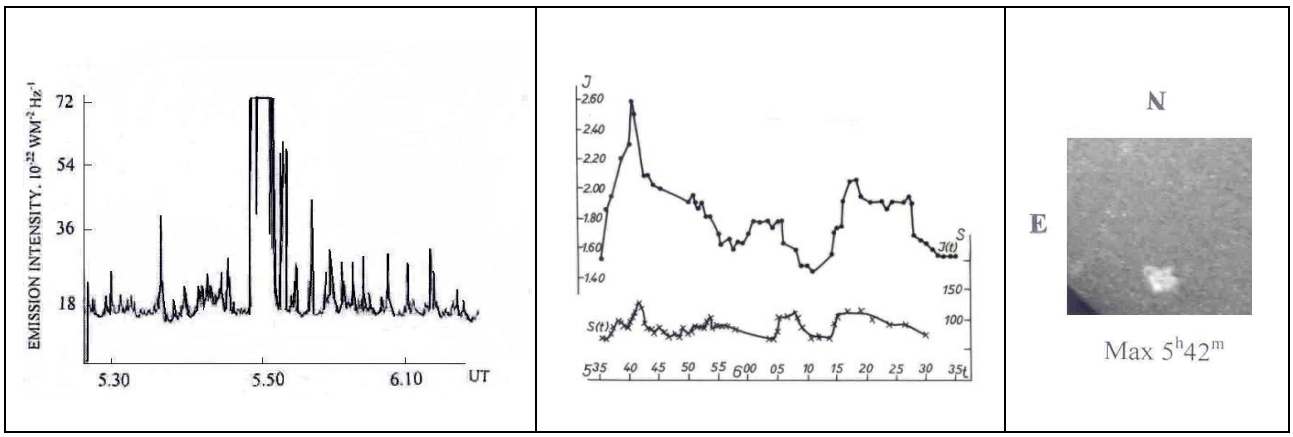

Figure 8. Observations of a flare №8. In the figure on the left, we can see a change in the radio flow. The diagram in the center shows the intensity and area of the flare. The photo on the right is the observation of Hα line.

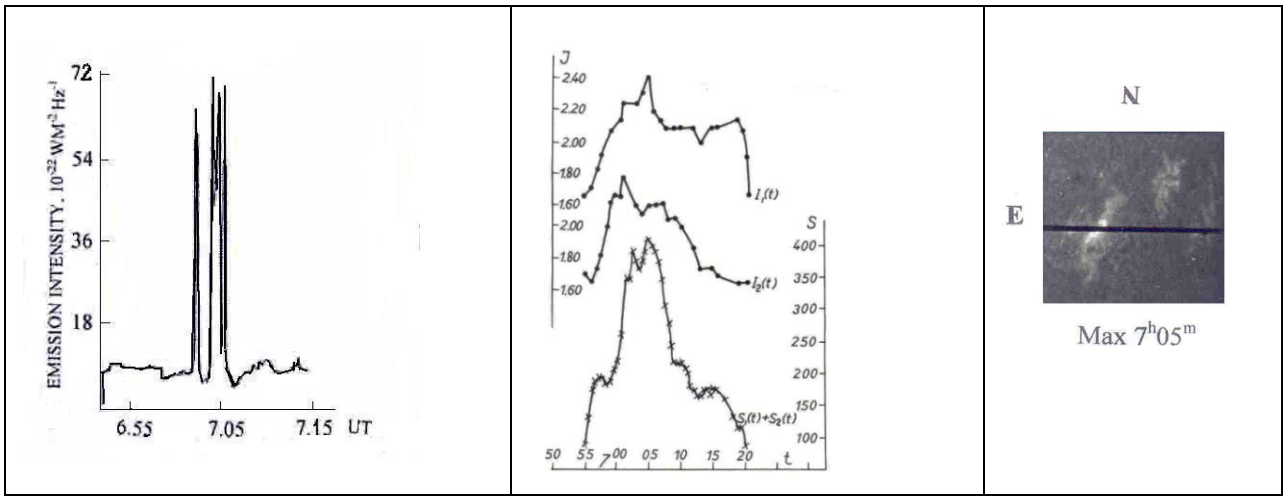

Figure 9. Observations of a flare № 9. In the figure on the left, we can see a change in the radio flow. The diagram in the center shows the intensity and area of the flare. The photo on the right is the observation of Hα line.

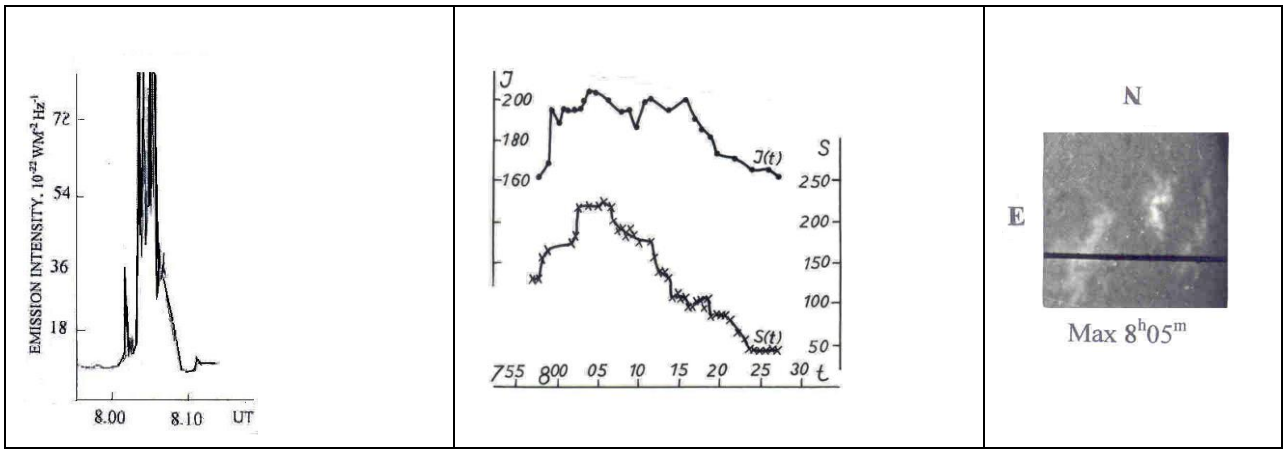

Figure 10. Observations of a flare № 10. In the figure on the left, we can see a change in the radio flow. The diagram in the center shows the intensity and area of the flare. The photo on the right is the observation of Hα line.

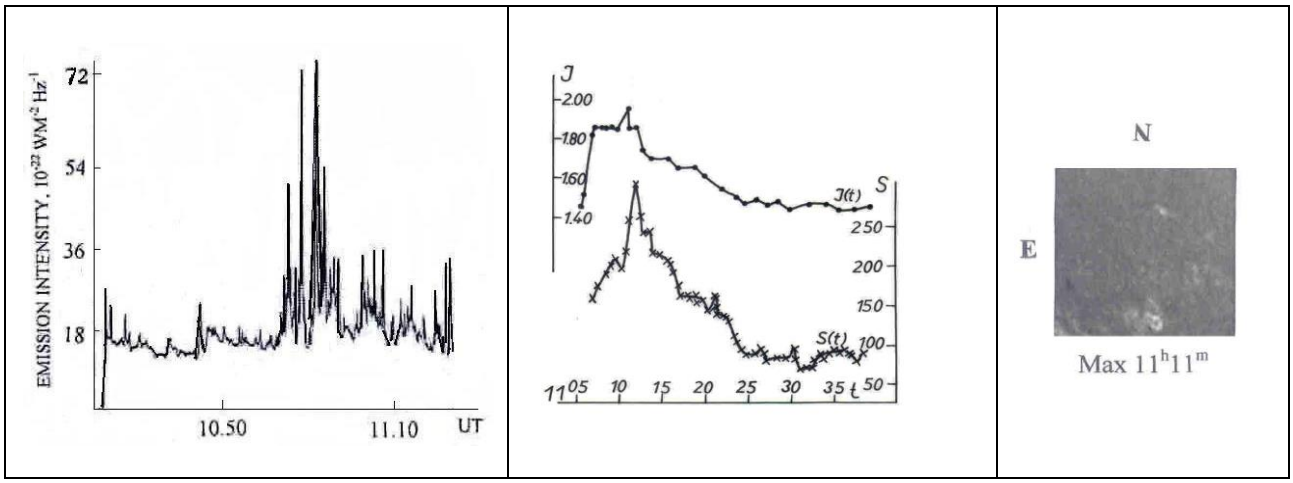

Figure 11. Observations of a flare № 11. In the figure on the left, we can see a change in the radio flow. The diagram in the center shows the intensity and area of the flare. The photo on the right is the observation of Hα line.

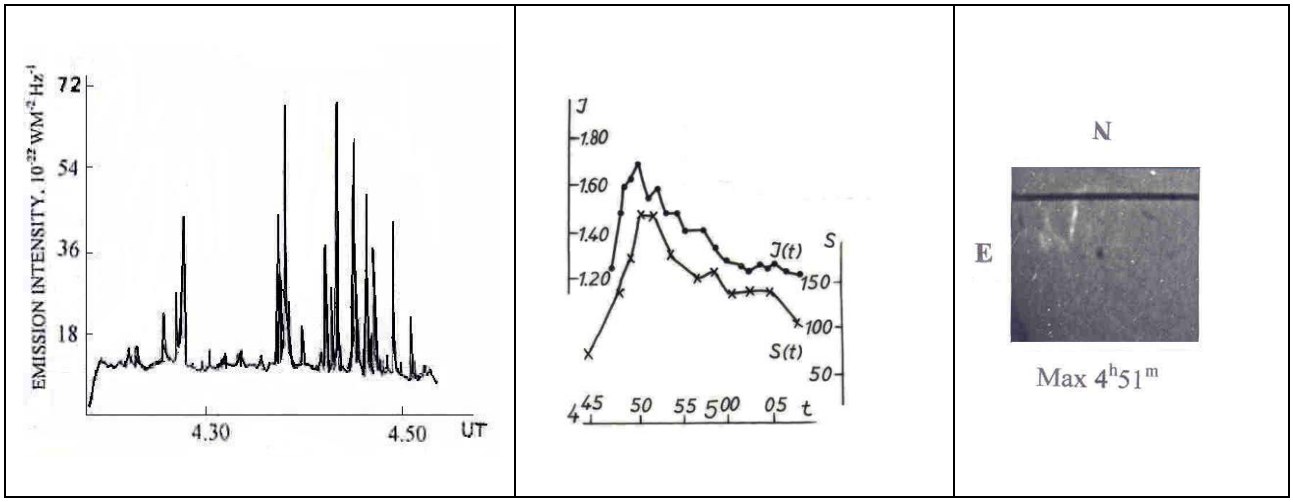

Figure 12. Observations of a flare № 12. In the figure on the left, we can see a change in the radio flow. The diagram in the center shows the intensity and area of the flare. The photo on the right is the observation of Hα line.

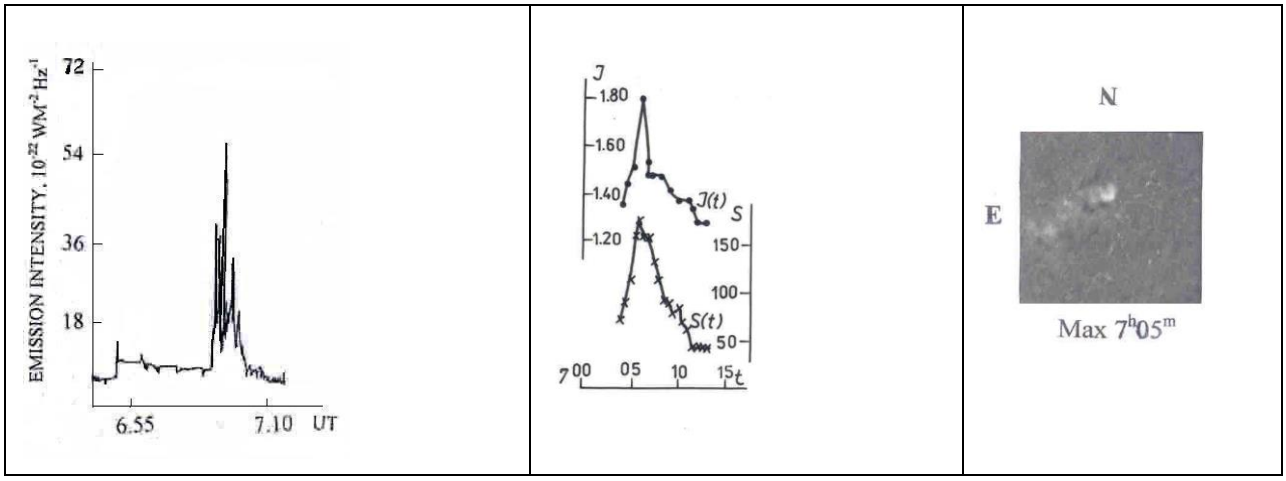

Figure 13. Observations of a flare № 13. In the figure on the left, we can see a change in the radio flow. The diagram in the center shows the intensity and area of the flare. The photo on the right is the observation of Hα line.

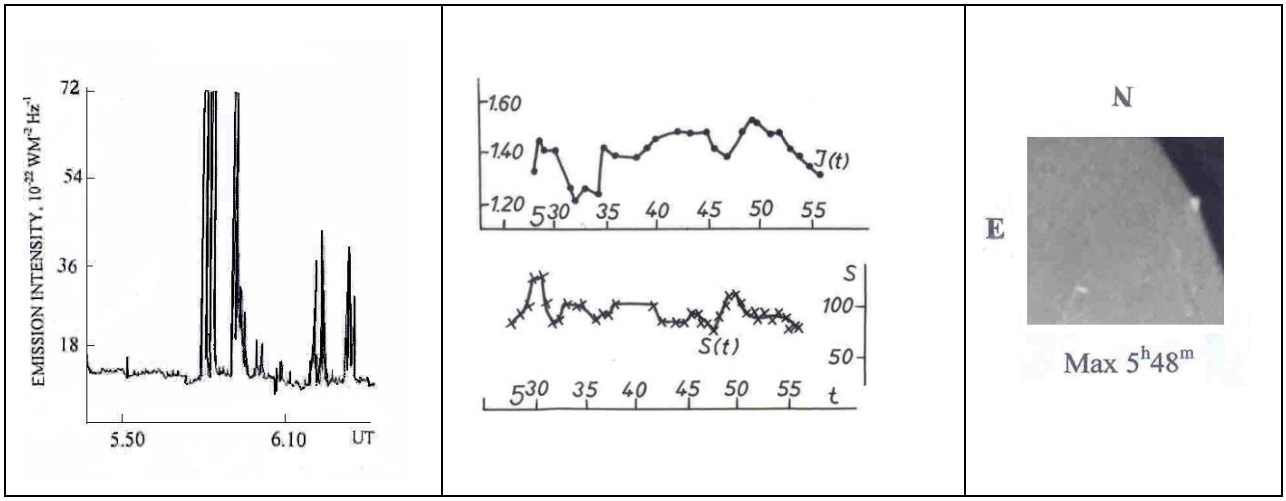

Figure 14. Observations of a flare № 14. In the figure on the left, we can see a change in the radio flow. The diagram in the center shows the intensity and area of the flare. On the right photo there is an observation in Hα line.

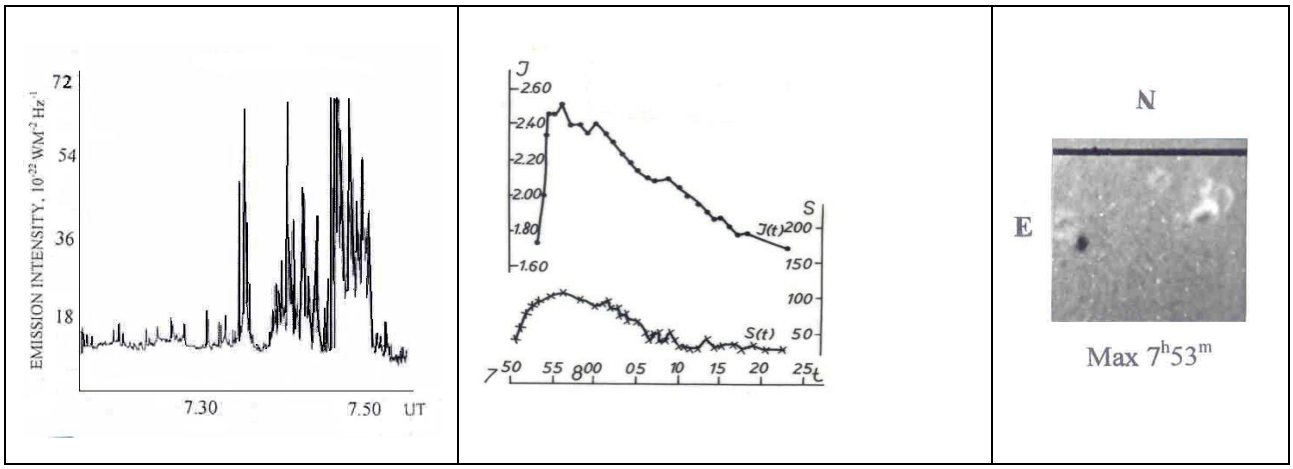

Figure 15. Observations of a flare № 15. In the figure on the left, we can see a change in the radio flow. The diagram in the center shows the intensity and area of the flare. The photo on the right is the observation of Hα line.

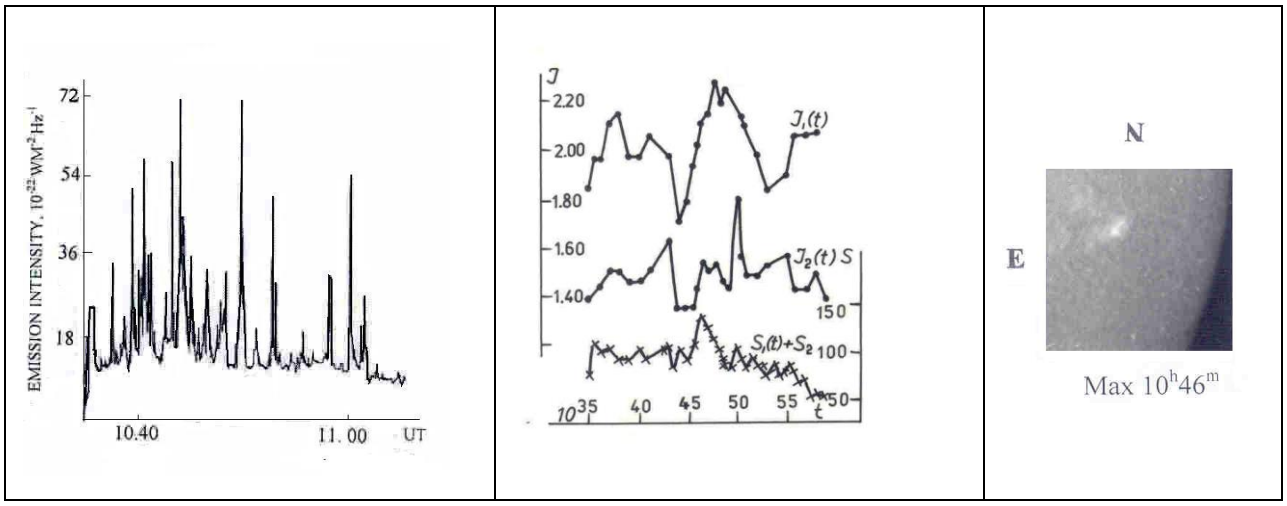

Figure 16. Observations of a flare № 16. In the figure on the left, we can see a change in the radio flow. The diagram in the center shows the intensity and area of the flare. The photo on the right is the observation of Hα line.

A detailed study of 16 chromospheric flares and the corresponding traces of 210 MHz radio emission have shown that the Hα emission of some of the flares is accompanied by a rise in the emission at 210 MHz within ½ hour from the onset or end of the flare.

By using the method of epoch superposition, it is possible to determine the sequence of events during the flare. We have selected 4 time points within a flare: (1) the onset of the flare in Hα; (2) the time of the maximum of the flare in Hα; (3) the precursor of a noise storm (a burst or group of bursts that almost always precede the main noise storm); and (4) the maximum of the noise storm. The time of the Hα flare peak was taken as the time origin. This time was subtracted from the time of the other three events for each flare to produce Table 2. On finding the average value for each column and the error in this average, we obtained a sequence of events in the optical and radio ranges during the flare (shown in Fig. 17).

TABLE 2. Time Intervals Between the Emission Peaks of Flares in Hα and other Events

Onset of flare	Precursor of noise storm	Maximum of noise storm	Onset of flare	Precursor of noise storm	Maximum of noise storm
-2	-12	0	-5	-4	-1
-3	-1	4	1	-12	1
-3	0	2	-3	-15	-3
-4	-5	-5	-4	0	1
-4	-4	1	-3	--	2
-6	-10	-6	-5	-12	0
-7	-5	9	-3	-6	0
-9	1	3			

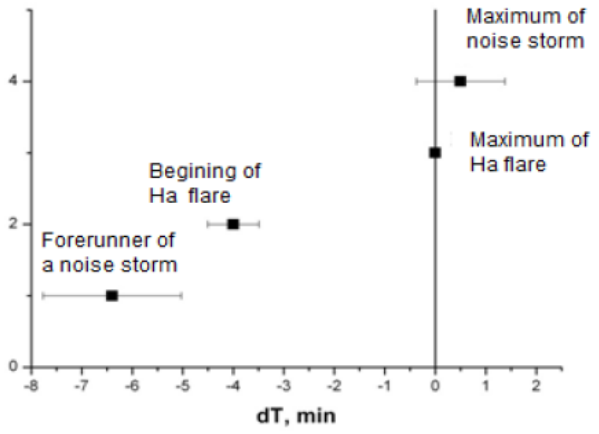

Figure 17. Events sequence in flare. Scale Y – conventional; horizontal lines – root-mean-square deviation from mean value

3. Discussion and results

Many researchers (Korolev O. S., et al., 1970, Zucca P., Carley E. P., et al., 2012) have obtained similar results in different frequency bands based on the interference and polarization observations. The variation in the continuum components of radio bursts is closely related to the area occupied by the sunspot group. Solar radio fla Beginning of t time, however, have a rigid relationship to oscillations in the magnetic field strength of s

A comparison of the radio flux at 10.7 cm with the number of sunspots for solar cycles 19-21 shows that the radio flux depends on the magnetic field associated with the sunspots. The radio flux at 10.7 cm and its relationship to the number of sunspots and other parameters has been reported for each of these cycles. These data show that the radio flux at 10.7 cm seems to be stochastic for cycle 19 and chaotic for cycles 20 and 21 (Greenkorn R. A., 2012, Greenkorn R. A., 2009).

The solar radio emission provides valuable information on the structure and dynamics of the sun's atmosphere above the temperature minimum. In an effort to provide maximum details in the picture of the quiet sun and active regionswith the aid of the radio regions, the researchers have examined new observational and theoretical results on the quiet sun and active regions over the entire range of the radio waves from millimeter to decameter wavelengths. In fact, the radio frequencies can provide us with as much information as the rest of the spectrum of the solar atmosphere.

Further refinement and improvements for the mechanism of noise bursts will require optical observations of chromospheric flares and spots with magnetographs. the observations of this kind will make it possible to determine the magnetic field strength of the large spots, as well as the variation in their area over time intervals in hours (Kies C., Rezaei R., and Schmidt W., 2014, Schad T. A. and Penn M. J., 2010, Zharkov S., Zharkova V. V., and Ipson S. S., 2005, Solov'ev A. and Kirichek E., 2014, Kallunki J. and Uunila M., 2014 Kallunki J., Lavonen N., Järvelä E., and Uunila M., 2012).

The major conclusions of Benz et al.(Benz A. O., Perret H., Saint-Hilaire P., and Zlobec P., 2006) suggest that the overall duration, peak flux and radiated energy at radio frequencies correlate with the energy released by a flare (measured in the x-ray range). They discussed the possible mechanisms for heating after the main phase of the flare, and these were compared with the observational data. Kossobokov, et al. (Kossobokov V., Le Moul J.L., and Courtillot V., 2012) examined 32355 class C2 and higher (C2+) flares from the GOES catalog. The amplitudes of the extreme flares increased when the average flux decreased. They calculated the average energy flux indices for an interval from 7 to 365 days.

Li and Fleishman (Li Y. and Fleishman G. D., 2009) have calculated the incoherent radio emission in terms of two stochastic MHD heating models. Their analysis clearly shows that the radio emission from the heating sites (1) is intense enough to be observed by the currently available radio instrumentation and (2) has spectra and light curves that differ distinctly in these two models. In particular, they proposed that some of the narrow-band microwave and decimeter bursts may be a consequence of stochastic heating in solar flares.

Based on the theory of electromagnetic radiation, equations have been derived to calculate the most intense frequencies in the spectrum of the solar radio emission. The observed frequency of the bands and the intervals between them were consistent with the calculations to high accuracy. The equality of the band frequencies indicates that they a reproduced by interference associated with the propagation of radio waves in plasma, rather than by a mechanism for the generation of the radiation in the main source of the burst (Yurovsky Yu.F., 2011).

Total, we have analyzed sixteen scale *n* (normal) flares in detail for the purpose of studying their motions, intensity and development.

The development of some of the flares is accompanied by the motions in the form of streams, ejection and elongations. These motions are similar to those in the protuberances, which appear after the solar spots.

The development of most of the flares was accompanied mainly by a more or less uniform expansion and subsequent contraction during the extinction of flare. The intensity at the flare maximum is greater when it expands more rapidly. The maximum intensities and areas of the flares do not always coincide in time.

4. Conclusions

Based on the analysis of the observational data, we have found that in most cases, the radio bursts are produced in a group of spots with a complicated structure and during the growth of large spots. In addition, the maxima of radio flares and the peak magnetic flux of the large groups of sunspots coincide within a day. On the other hand, a strong magnetic flux in a group of spots is a precursor of a strong chromospheric flare.

This analysis of the experimental data shows that the maximum duration of radio noise is 7-10 days and the flares appear earlier and disappear later than the elevated radiation background.

In most cases (ten times out of sixteen), the area of the flare reached its maximum at the same time as intensity.

In two cases, the area of the flare did not change significantly over the entire duration of the flare, and only in a few cases, the area of the flare reached its maximum just before or after the intensity peak.

In six of sixteen cases, the maximum energy releases in the meter radio range and in Hα line, they were almost simultaneous; in five cases, the radio peak occurred earlier, and in four cases, the radio peak occurred later than in Hα line.

Observations of this type are very important for the study of the fundamental problems of the solar-terrestrial associations.

In particular, they can be used for long-term weather predictions. Recording noise storms and radio bursts of different types and comparing these with optical observations can expand our knowledge of the physical processes taking place on the sun and be of a help to interpret the theoretical models correctly.

Acknowledgement

The authors gratefully acknowledge to Dr. NatalyNikolaenaStepanianof Crimean Astrophysical Observatory for her useful remarks.

This work was supported by Shota Rustaveli National Science Foundation (SRNSF), grant number FR/21 71 88/16, Project Title: "The Solar Coronal Holes and Their connection to Solar Low Atmospheric Magnetic Structures".

References

BastianT. S. Benz., A. O., and GaryD. E., Ann. Rev. Astron. Astrophys. 1998.**36**. 131.
BenzA. O., PerretH., Saint-HilaireP., and ZlobecP., Adv. Space Res. 2006.**38**. 951.
Chernov G. P., Astron. Lett. 1997.**23**. 949.
De Feiter. L. D, FokkerA. D., and RoosenJ., Nature, 1959.**184**, 805.
DodsonH. W., Proc. Inst. Radio Eng. 1958.**46**. 149.
Dodson H. W. and HedemanE. R., Astrophys. J. 1958. **128**. 636.
Dodson H. W. and HedemanE. R., Astronom. J. 1960. **65**, 51.
Fokker A. D., in: Solar System Radio Astronomy (1965), p. 171.
Greenkorn R. A., Solar Phys. 2009.**255**. 301.
GreenkornR. A., Solar Phys. 2012. **280**. 205.
Hey J. S., Nature. 1946. **157**. 47.
Innes. D. E., Kameron R. H., et al., ,Astron. Astrophys. 2011, **431**, p. 4 .
Kallunki J., Lavonen N., Järvelä E., and Uunila M., Baltic Astron. 2012.**21**.255.
Kallunki J. and Uunila M., International J. Astron. Astrophys. 2014. **4**. 649.
Kies C., Rezaei R., and Schmidt W., Astron. Astrophys. 2014. **565**. ID: A52. 10.
Korolev O. S., et al., in: Proc. of the Meeting of Sci. Commit. for Complex Problems in Radio Astronomy (1970), 83.
Korolev O. S., Astron. zh. 1975.**52**.1247. (Soviet Astronomy 1976.**19**. 747).
Korolev O. S., The Physics of Solar Activity [in Russian], Nauka, Moscow (1976), p. 192.
KossobokovV., Le MouлlJ.L., and CourtillotV., Solar Phys. 2012.**276**. 383.
KruckerS., BenzA. O., BastianT. S., and ActonL. W., Astrophys. J. 1997.**488**. 499.
Li Y.and FleishmanG. D., Astrophys. J. 2009. **701**. L52.
Makandarashvili.Sh., Byull.Abast.Astrofiz.Observ 1962.**29**. 47.
Pawsey J. LPayne-Scott., R., and McCready L. L., Nature 1946.**157**.158.
Pawsey J. L. and Bracewll R. N., in: Radio Astronomy, Clarendon Press, Oxford (1955), ch. 5.
Ryle M. and Vonberg D. D., Proc. Roy.Soc. 1948.**193**, 98**.**
Schad T. A. and Penn M. J., Solar Phys. 2010.**262**.19.
Shibasaki K., Alissandrakis C. E., and Pohjolainen S., Solar Phys. 2011.**273**. 309
Solov'ev A. and Kirichek E., Astrophys. Space Sci. 2014. **352**. 23.
Swarup.G., StoneP. H., and MaxwellA., Astrophys. J. 1960.**131**, 725.
VourlidasA., BastianT. S., and. AschwandenM. J, Astrophys. J. 1997.**489**. 403.
YurovskyYu. F., Bull. Crimean Astrophys.Obs. 2011.**107.** 84.
Zharkov S., Zharkova V. V., and Ipson S. S., Solar Phys. 2005. **228**. 377.
Zucca P., Carley E. P., et al., Solar Phys. 2012. **280**.591.

Astronomy & Astrophysics (Caucasus) 2, (2016) (74-80)

WIGNER COEFFICIENTS OF COSMOLOGICAL GROUP SO (2.1)

B. A. Rajabov

N. Tusi Shamakhi Astrophysics Observatory, National Academy of Sciences of Azerbaijan, AZ2243, Shamakhi, Azerbaijan,

Email:balaali.rajabov@mail.ru

Abstract

The article examines representations of the group SO (2,1), which has important applications in cosmology, elementary particle theory and mathematical physics. Irreducible unitary representations of the principal continuous and supplementary,as well as discrete serieswere obtained. The Wigner coefficients of these representationswere computed and their explicit expressions using the bilateral serieswere represented. The results will be used to study the particles with spins in the world of anti-de Sitter space.

Key words: Representation of Lie group, de Sitter space, Wigner coefficients, group SO(2,1), principal continuousseries, supplementary series, discrete series.

Received October 19, 2016; revised December 19, 2016

1.Introduction

Representations of group $SO(2,1)$appear in various problems of theoretical and mathematical physics (Alhaidari, A.D. 2002), in particular, as a group of motions in general theory of relativity (Gaetano V. and Patrizia V. 2002) and in dual models of hadron reactions (Verdiev I.A. 1974). On the other hand, group$SO(2,1)$is the normal divisor of a non-homogenous group$ISO(2,1)$- the group of motions in the three dimensional pseudo-Euclidean space, which is the stationary subgroup of a surface of transitivity, namely the cone of the group of de Sitter $SO(3,2)$.

Group$SU(1,1)$of second order pseudo-unitary matrices and group$SL(2,R)$of real second order unimodular matrices are universal covering groups for group $SO(2,1)$and are locally isomorphic to it. Representations of groups $SU(1,1)$and$SL(2,R)$were studied in (Gelfand I.M., Graev M.I.. Vilenkin H.Y. 1962., Vilenkin N.Y. 1965)using methods of integral geometry and invariant bilinear forms. In this paper, we present the description of the theory of representations of group $SO(2,1)$using generalized functions and the method of invariant bilinear forms.

1. IRREDUCIBLE UNITARY REPRESENTATIONS

Group $SO(2,1)$is a connected component unit of the group of motions in the 3-dimensional pseudo-Euclidean space retaining invariant the following quadratic form:

$$[k,k] = k_0^2 - k_1^2 - k_2^2.$$

It is three-parametrical, similar to group $SO(3)$of rotations of 3-dimensional Euclidean space.We introduce the following system of coordinates on the upper field of ahyperboloid$[k,k] = 1, k_0 > 0$:

$$[k,k] = (\cosh\alpha, \sinh\alpha \sin\varphi, \sinh\alpha \cos\varphi).$$

Since the upper field of the hyperboloid $[k,k] = 1, k_0 > 0$, is a transitive surface selecting $k = (1,0,0)$as a fixed point of group $SO(2,1)$, one can get the following simplification:

$$g = r(\varphi_1)h(\alpha)r(\varphi_2), \quad g \in SO(2,1), \qquad (1)$$

Where$r(\cdot)$ the rotations on the plane(k_1, k_2) and$h(\alpha)$ is the hyperbolic rotations on the plane(k_0, k_2).

The representation of group$SO(2,1)$will be constructed in the space$\mathcal{F}^{\sigma}$of infinitely differentiable homogeneous functions defined on the upper field of a cone without the vertex, $[k,k]=0, k_0>0$ and the degree of homogeneityσ:

$$F(ak)=a^{\sigma}F(k), \quad a>0, \qquad (2)$$

$$T(g)F(k)=F(g^{-1}k), \ \ g\in SO(2,1) \qquad (3)$$

Introduce the following system of coordinates on the cone $[k,k]=0, k_0>0$:

$$k=\omega(1,\sin\varphi,\cos\varphi), \quad \omega>0, \quad 0\le\varphi<2\pi. \qquad (4)$$

Then by applying (2)-(4), one can establish an isomorphism between the space $\mathcal{F}^{\sigma}$and the space of infinitely differentiable functions on circleS^1:

$$F(k)=\omega^{\sigma}f(\varphi); \qquad f(\varphi)=F(k)|_{\omega=1} \qquad (5)$$

We use the same notation $\mathcal{F}^{\sigma}$ for the space of infinitely differentiable functions on the circle. The usual Fourier expansion is used for the canonical expansion:

$$f(\varphi)=\sum_{m=-\infty}^{+\infty} f_m e^{im\varphi} \qquad (6)$$

It is obvious that a restriction of the representation (3) to the subgroup of rotations on the plane (k_1,k_2) is an additive group on the circle:

$$T\big(r(\varphi_1)\big)f(\varphi)=f(\varphi-\varphi_1) \qquad (7)$$

The restriction of the representation (3) to the subgroup of hyperbolic rotations on the plane $(k_0,k_2)$is given by the following formula:

$$T\big(h(\alpha)\big)f(\varphi)=\omega_{\alpha}^{\sigma}\, f(\varphi_{\alpha}), \qquad (8)$$

Where

$$\cos\varphi_{\alpha}=\frac{-\sinh\alpha+\cosh\alpha\cos\varphi}{\omega_{\alpha}}. \qquad (9)$$

Irreducible unitary representations of continuous principal series are obtained by introducing the following scalar product in $\mathcal{F}^{\sigma}$:

$$\big(f^{(1)},f^{(2)}\big)=\frac{1}{2\pi}\int_0^{2\pi}\overline{f^{(1)}(\varphi)}\,f^{(2)}(\varphi)d\varphi \qquad (10)$$

Where the sign “bar” denotes the complex conjugate. Since the circle is a compact space here in the sequel we use, as widely accepted, the measure normalized to one. It follows from (9), that measure $d\varphi$at the hyperbolic rotations(8) is transformed as:$d\varphi_{\alpha}=\frac{d\varphi}{\omega_{\alpha}}$. (11)

Obviously it is invariant for rotations(7). It is also obvious that functions $e^{im\varphi}$forms an orthonormal canonical basis with respect to the scalar product (10).

It follows from (7)-(9) and (11) that the scalar product (10) is invariant if the degree of homogeneity $\sigma$is as follows:

$$\sigma=-\frac{1}{2}+i\rho, \qquad -\infty<\rho<+\infty. \qquad (12)$$

Unitary and irreducibility of other series of representations in this space are studied by constructing invariant Hermit-bilinear functionals:

$$\big(f^{(1)},f^{(2)}\big)=\frac{1}{4\pi^2}\int_0^{2\pi}\int_0^{2\pi}K(\varphi_1,\varphi_2)\overline{f^{(1)}(\varphi_1)}\,f^{(2)}(\varphi_2)d\varphi_1 d\varphi_2 \qquad (13)$$

Here$K(\varphi_1,\varphi_2)$is a generalized function over the space $\mathcal{F}^{\sigma}\otimes\mathcal{F}^{\sigma}$.

The invariance condition as well as formulas (7)-(8) and (11) imply that $K(\varphi_1,\varphi_2)$ is a function, which:

• depends on the difference of variables$(\varphi_1-\varphi_2)$;

• satisfies the following equation:

$$K(\varphi_{1\alpha},\varphi_{2\alpha})=\omega_{\alpha}^{\overline{\sigma}+1}(\varphi_1)\omega_{\alpha}^{\sigma+1}(\varphi_2)K(\varphi_1,\varphi_2) \qquad (14)$$

Where $\omega_\alpha(\cdot)$is defined in(9). One can show that the solution to the equation (14) exists only when $\overline{\sigma} = \sigma$and this solution is:

$$K(\varphi_1, \varphi_2) = c[1 - \cos(\varphi_1 - \varphi_2)]^{-\sigma-1} \qquad (15)$$

Here$c$ is an arbitrary constant.

Thus, the invariant Hermit-bilinear form in space $\mathcal{F}^\sigma \otimes \mathcal{F}^\sigma$can be expressed as:

$$\left(f^{(1)}, f^{(2)}\right) = \frac{c}{4\pi^2} \int_0^{2\pi} \int_0^{2\pi} \frac{\overline{f^{(1)}(\varphi_1)} f^{(2)}(\varphi_2)}{[1 - \cos(\varphi_1 - \varphi_2)]^{\sigma+1}} d\varphi_1 d\varphi_2, \qquad (16)$$

Where$\sigma$is a real number.

In order to find canonical expression (16) and to study non-degeneracy and irreducibility of representations, it is necessary to find the Fourier expansion for the interior of this integral representation. Since this expansion will be used to study equivalency of representations and its Wigner coefficients, we consider complex values of σ.

2.FOURIER EXPANSION OF THE FUNCTION$(1 - \cos\psi)^\lambda$

We will formulate the Fourier-expansion of function$(1 - \cos\psi)^\lambda$,where$\lambda \in \mathbb{C}$ is a complex number:

$$(1 - \cos\psi)^\lambda = \sum_{m=-\infty}^{+\infty} a_m e^{im\psi}. \qquad (17)$$

$$a_m = \frac{1}{2\pi} \int_0^{2\pi} (1 - \cos\psi)^\lambda e^{im\psi}\, d\psi \qquad (18)$$

Applying Taylor series to$(1 - \cos\psi)^\lambda$ and using the Gauss formula for hypergeometric function of the unit variable (Slater L.J. 1966., Bateman, G., Erdélyi A., 1973), one can get the following expression for coefficients a_m:

$$a_m = \frac{2^\lambda \Gamma(\lambda + 1/2)}{\sqrt{\pi}\Gamma(m + \lambda + 1)} (-\lambda)_m \qquad (19)$$

In these formulas, we used the notation $(-\lambda)_m$for the Pochhammer symbol (Bateman, G., ErdélyiA., 1973). Thus the expansion (17) has the form:

$$(1 - \cos\psi)^\lambda = \frac{2^\lambda \Gamma(\lambda + 1/2)}{\sqrt{\pi}} \sum_{m=-\infty}^{+\infty} \frac{(-\lambda)_m}{\Gamma(m + \lambda + 1)} e^{im\psi}. \qquad (20)$$

It can be seen from here that the integral (18) converges when $Re\lambda > -1/2$. This integral can be considered in the sense of regularized values (GelfandI.M., Shilov G.E.1959) when $Re\lambda < -1/2$.

3.SUPPLEMENTARY AND DISCRETE SERIES OF REPRESENTATIONS

It follows from (20) that in order to provide regularization of the form (16) it is sufficient to choose the arbitrary constant c as:

$$c = \frac{1}{\Gamma(-\sigma - 1/2)}$$

Since for this form$\lambda = -\sigma - 1$. In conclusion, for the invariant Hermit-bilinear form in space $\mathcal{F}^\sigma \otimes \mathcal{F}^\sigma$we have the following integral representation:

$$\left(f^{(1)}, f^{(2)}\right) = \frac{1}{4\pi^2\Gamma(-\sigma - 1/2)} \int_0^{2\pi} \int_0^{2\pi} \frac{\overline{f^{(1)}(\varphi_1)} f^{(2)}(\varphi_2)}{[1 - \cos(\varphi_1 - \varphi_2)]^{\sigma+1}} d\varphi_1 d\varphi_2 \qquad (21)$$

Recall that here $\sigma$is a real number.

By applying (6) and (20),one can get the canonical form of the functional (21):

$$\left(f^{(1)}, f^{(2)}\right) = \frac{2^{-\sigma-1}}{\sqrt{\pi}} \sum_{m=-\infty}^{+\infty} a_m \overline{f_m^{(1)}} f_m^{(2)} \qquad (22)$$

Here

$$a_m = \frac{(\sigma+1)_m}{\Gamma(m-\sigma)} \qquad (23)$$

From (23), it follows that form (22) to be defined positively - it is necessary and sufficient for the satisfaction of the following condition:

$$\frac{m+\sigma+2}{m-\sigma+1} > 0$$

for all integer $m$andreal numbersσ. This condition is satisfied only when -1<σ<0.It is obvious that form (22)is non-degenerate for non-integer σ. Thus we get:

Theorem.*The representation (7)-(9) in space $\mathcal{F}^{\sigma}$is irreducible unitary with respect to scalar product (21) for -1<σ<0. This representation is called the supplementary series.*

For integer values of σ,form (22)-(23), obviously, degenerates.

1. $\sigma = 1,2, \ldots,$

Form (22) degenerates in subspace $\mathcal{F}_0^{\sigma}$, where

$$\mathcal{F}_0^{\sigma} = \{a_m = 0, \ \ m = \sigma, \sigma-1, \sigma-2, \ldots, -\infty\}$$

Space $\mathcal{F}_0^{\sigma}$consists of functions of the form:

$$f(\varphi) = \sum_{m=-\infty}^{\sigma} f_m e^{im\varphi} = e^{i\sigma\varphi} \sum_{m=0}^{+\infty} f'_m e^{-im\varphi}$$

2. $\sigma = -1, -2, -3, \ldots,$

Form (22) degenerates in subspaces $\mathcal{F}_-^{\sigma}$and$\mathcal{F}_+^{\sigma}$, where

$$\mathcal{F}_+^{\sigma} = \{a_m = 0, \ \ m = -\sigma, -\sigma+1, -\sigma+2, \ldots, +\infty\}$$
$$\mathcal{F}_-^{\sigma} = \{a_m = 0, \ \ m = \sigma, \sigma-1, \sigma-2, \ldots, -\infty\}$$

Space $\mathcal{F}_+^{\sigma}$consists of functions of the form:

$$f(\varphi) = \sum_{m=-\sigma}^{+\infty} f_m e^{im\varphi} = e^{i\sigma\varphi} \sum_{m=0}^{+\infty} f'_m e^{im\varphi}$$

Space $\mathcal{F}_-^{\sigma}$consists of functions of the form:

$$f(\varphi) = \sum_{m=-\infty}^{\sigma} f_m e^{im\varphi} = e^{i\sigma\varphi} \sum_{m=0}^{+\infty} f'_m e^{-im\varphi}$$

Thus, we obtain irreducible representations for nonnegativeσin a factor-space $\mathcal{F}^{\sigma}/\mathcal{F}_0^{\sigma}$, and for negative σin a factor-space$\mathcal{F}^{\sigma}/(\mathcal{F}_+^{\sigma} \oplus \mathcal{F}_-^{\sigma})$, respectively. They are representations of discrete series.

4.WIGNER COEFFICIENTS OF GROUP SO(2,1)

In this section we study invariant tri-linear forms in space $\mathcal{F}^{\sigma_1} \otimes \mathcal{F}^{\sigma_2} \otimes \mathcal{F}^{\sigma_3}$. Similar to (13), the invariant tri-linear forms will have the following form:

$$\left(f^{(1)}, f^{(2)}, f^{(3)}\right) = \frac{1}{(2\pi)^3} \int_0^{2\pi}\int_0^{2\pi}\int_0^{2\pi} K^{(3)}(\varphi_1, \varphi_2, \varphi_3)\, f^{(1)}(\varphi_1) f^{(2)}(\varphi_2) f^{(3)}(\varphi_3) d\varphi_1 d\varphi_2 d\varphi_3 \qquad (24)$$

Here$K^{(3)}(\varphi_1, \varphi_2, \varphi_3)$is a generalized function over space $\mathcal{F}^{\sigma_1} \otimes \mathcal{F}^{\sigma_2} \otimes \mathcal{F}^{\sigma_3}$. It follows from the invariance condition and also from (7)-(9) and (11) that:

• $K^{(3)}(\varphi_1, \varphi_2, \varphi_3)$is a function depending on differences of variables $\varphi_1 - \varphi_2, \varphi_2 - \varphi_3, \varphi_3 - \varphi_1$;
• $K^{(3)}(\varphi_1, \varphi_2, \varphi_3)$is a function satisfying the following equation:

$$K^{(3)}(\varphi_{1\alpha}, \varphi_{2\alpha}, \varphi_{3\alpha}) = \omega_\alpha^{\sigma_1+1}(\varphi_1)\omega_\alpha^{\sigma_2+1}(\varphi_2)\omega_\alpha^{\sigma_3+1}(\varphi_3)K^{(3)}(\varphi_1, \varphi_2, \varphi_3) \qquad (25)$$

Where$\omega_\alpha(\cdot)$is defined in (9). It is possible to show that the functional equation (25) has a solution with the accuracy of constant:

$$K^{(3)}(\varphi_1, \varphi_2, \varphi_3) = c\frac{[1-\cos(\varphi_1-\varphi_2)]^{\beta_3}}{\Gamma(\beta_3+1/2)}\frac{[1-\cos(\varphi_2-\varphi_3)]^{\beta_1}}{\Gamma(\beta_1+1/2)}\frac{[1-\cos(\varphi_1-\varphi_2)]^{\beta_3}}{\Gamma(\beta_3+1/2)}\ ; \quad (26)$$

Here

$$\beta_1 = \frac{\sigma_1-\sigma_2-\sigma_3-1}{2} \qquad (27.1)$$

$$\beta_2 = \frac{\sigma_2-\sigma_1-\sigma_3-1}{2} \qquad (27.2)$$

$$\beta_3 = \frac{\sigma_3-\sigma_2-\sigma_1-1}{2} \qquad (27.3)$$

Wigner coefficients are defined as the value of functional (24) on elements of a canonical basis:

$$\begin{pmatrix}\sigma_1 & \sigma_2 & \sigma_3\\ m_1 & m_2 & m_3\end{pmatrix}$$
$$= \frac{c}{(2\pi)^3}\int_0^{2\pi}\int_0^{2\pi}\int_0^{2\pi}\frac{[1-\cos(\varphi_1-\varphi_2)]^{\beta_3}}{\Gamma(\beta_3+1/2)}\frac{[1-\cos(\varphi_2-\varphi_3)]^{\beta_1}}{\Gamma(\beta_1+1/2)}\frac{[1-\cos(\varphi_1-\varphi_2)]^{\beta_3}}{\Gamma(\beta_3+1/2)}$$
$$\times e^{im_1\varphi_1}e^{im_2\varphi_2}e^{im_3\varphi_3}d\varphi_1 d\varphi_2 d\varphi_3. \qquad (28)$$

Where$\beta_1,\ \beta_2,\ \beta_3$are defined in (27).

By using expansion (20),we have:

$$\begin{pmatrix}\sigma_1 & \sigma_2 & \sigma_3\\ m_1 & m_2 & m_3\end{pmatrix}$$
$$= c\frac{2^{\sigma_1+\sigma_2+\sigma_3}}{(2\pi)^3\pi^{3/2}}\int_0^{2\pi}\int_0^{2\pi}\int_0^{2\pi}\sum_{k=-\infty}^{+\infty}\frac{(-\beta_3)_k}{\Gamma(k+\beta_3+1)}e^{ik(\varphi_1-\varphi_2)}\sum_{l=-\infty}^{+\infty}\frac{(-\beta_1)_l}{\Gamma(l+\beta_1+1)}e^{il(\varphi_2-\varphi_3)}$$
$$\times\sum_{n=-\infty}^{+\infty}\frac{(-\beta_2)_n}{\Gamma(n+\beta_2+1)}e^{ik(\varphi_3-\varphi_1)}e^{i(m_1\sigma_1+m_2\sigma_2+m_3\sigma_3)}d\varphi_1 d\varphi_2 d\varphi_3$$

Since the exponents are orthonormal, it follows that the last expression is not zero only under condition:

$$m_1 + m_2 + m_3 = 0 \qquad (29)$$

And after necessary integrations and transformations this expression is reduced to:

$$\begin{pmatrix}\sigma_1 & \sigma_2 & \sigma_3\\ m_1 & m_2 & m_3\end{pmatrix}$$
$$= c\frac{2^{-(\sigma_1+\sigma_2+\sigma_3+3)/2}}{\pi^{3/2}}$$
$$\times\sum_{n=-\infty}^{+\infty}\frac{(-\beta_1)_{n-m_1}}{\Gamma(n-m_1+\beta_3+1)}\frac{(-\beta_1)_{n+m_3}}{\Gamma(n+m_3+\beta_1+1)}\frac{(-\beta_2)_n}{\Gamma(n+\beta_2+1)} \qquad (30)$$

Here, we have taken into account that

$$\beta_1 + \beta_2 + \beta_3 = -\frac{\sigma_1+\sigma_2+\sigma_3+3}{2}$$

Formula (30) can be reduced to the following form:

$$\begin{pmatrix} \sigma_1 & \sigma_2 & \sigma_3 \\ m_1 & m_2 & m_3 \end{pmatrix}$$
$$= \frac{c}{\sqrt{2^{\sigma_1+\sigma_2+\sigma_3+3}\pi}} \frac{(-\beta_3)_{-m_1}(-\beta_1)_{m_3}}{\Gamma(\beta_2+1)\Gamma(-m_1+\beta_3+1)\Gamma(m_3+\beta_1+1)}$$
$$\times \sum_{n=-\infty}^{+\infty} \frac{(-\beta_3-m_1)_n(-\beta_1+m_3)_n(-\beta_2)_n}{(-m_1+\beta_3+1)_n(m_3+\beta_1+1)_n(\beta_2+1)_n}$$

The last expression with the accuracy of constant coincides with the bilateral series (Slater L.J. 1966):

$$\begin{pmatrix} \sigma_1 & \sigma_2 & \sigma_3 \\ m_1 & m_2 & m_3 \end{pmatrix} =$$
$$\frac{c(-1)^{m_1}\left[2^{\sigma_1+\sigma_2+\sigma_3+3}\pi\right]^{-\frac{1}{2}}(-\beta_1)_{m_3}}{\Gamma(\beta_2+1)\Gamma(-m_1+\beta_3+1)\Gamma(m_3+\beta_1+1)(1+\beta_3)_{m_1}} {}_3H_3\left[\begin{matrix} -\beta_3-m_1, & -\beta_1+m_3, & -\beta_2; \\ -m_1+\beta_3+1, & m_3+\beta_1+1, & \beta_2+1; \end{matrix} 1\right] \quad (31)$$

The expression for ${}_3H_3$-function is significantly simplified in case $m_1 = m_2 = m_3$=0. In this case, by applying the results from (Slater L.J. 1966), we will have:

$${}_3H_3\left[\begin{matrix} -\beta_3, & -\beta_1, & -\beta_2; \\ \beta_3+1, & \beta_1+1, & \beta_2+1; \end{matrix} 1\right] = \frac{\Gamma(\beta_1+1)\Gamma(\beta_2+1)\Gamma(\beta_3+1)\Gamma(\beta_1+\beta_2+\beta_3+1)}{\Gamma(\beta_1+\beta_2+1)\Gamma(\beta_1+\beta_3+1)\Gamma(\beta_2+\beta_3+1)} \quad (32)$$

The arbitrary constant c is defined so that the following condition is satisfied:

$$\begin{pmatrix} \sigma_1 & \sigma_2 & \sigma_3 \\ 0 & 0 & 0 \end{pmatrix} = 1 \quad (33)$$

Then from (31)-(33), for constant $c$we get:

$$c = \sqrt{2^{\sigma_1+\sigma_2+\sigma_3+3}\pi} \frac{\Gamma(\beta_1+\beta_2+1)\Gamma(\beta_1+\beta_3+1)\Gamma(\beta_2+\beta_3+1)}{\Gamma(\beta_1+\beta_2+\beta_3+1)}$$

Finally, taking into account (29),we get the following expression for Wigner coefficients:

$$\begin{pmatrix} \sigma_1 & \sigma_2 & \sigma_3 \\ m_1 & m_2 & m_3 \end{pmatrix} = \frac{(-1)^{m_1}\delta_{m_1+m_2+m_3,0}}{\Gamma(\beta_2+1)\Gamma(-m_1+\beta_3+1)\Gamma(m_3+\beta_1+1)} \frac{\Gamma(\beta_1+\beta_2+\beta_3+1)}{\Gamma(\beta_1+\beta_2+1)\Gamma(\beta_1+\beta_3+1)\Gamma(\beta_2+\beta_3+1)} \times$$
$$\frac{(-\beta_1)_{m_3}}{(1+\beta_3)_{m_1}} {}_3H_3\left[\begin{matrix} -\beta_3-m_1, & -\beta_1+m_3, & -\beta_2; \\ -m_1+\beta_3+1, & m_3+\beta_1+1, & \beta_2+1; \end{matrix} 1\right] \quad (34)$$

Here,$\beta_1,\ \beta_2,\ \beta_3$are defined in (27.1)-(27.3)

5.CONCLUSION

It is important to compare the results obtained for group$SO(2,1)$with the theory of representations of Lorentz subgroup $SO(3,1)$, (Gelfand I.M., MinlosR.A. 1958., Naimark M.A. 1958).It can be seen from the analysis given in Section 4 that the representations of group $SO(2,1)$,despite the dimension reduction, have more complex and rich structure. On the other hand, unlike Lorentz groups, Wigner coefficients are expressed not in the form of hypergeometric series, but in the form of bilateral series of one variable.

Since $SO(2,1)$is the normal divisor of the stationary subgroup of a 3-dimensional cone, which is the transitivity surface of the de Sitter group $SO(3,2)$, the obtained results will play a significant role in studying spin particles in the world of anti-de Sitter.

This work is the continuation of our investigations of the theory of representations and Wigner coefficients of the de Sitter and related groups.

References

Alhaidari, A.D. Graded extensions of $SO(2,1)$ Lie algebra and the search for exact solutions of Dirac equation by point canonical transformations, archiv:math-ph/0112004, 2002, p. 14.

Bateman, G., Erdélyi A., Higher transcendental functions, M.: Nauka, 1973, v. 1, 294 p. (In Russian).

Gaetano V. and Patrizia V. On the $SO(2,1)$ symmetry in General Relativity, arXiv:gr-qc/0202018v.1, 2002, p.10.

Gelfand I.M., Minlos R.A. Shapiro Z.Y., Presentations of group of rotation and Lorentz group, M.: Physmatgiz, 1958, 368 p. (In Russian).

Gelfand I.M.,Shilov G.E. Generalization of the function and operations on them (Generalized Functions, vol. 1, 2nd edition) - M.: Physmatlit, 1959, 471 p.(In Russian).
Gelfand I.M., Graev M.I.. Vilenkin H.Y. Integral geometry and associated questions of the theory of representation, M.: Physmatlit**,**1962, 656 p.(In Russian).
NaimarkM.A. Linear representations of the Lorentz group - M.: FM 1958, 376 p. (In Russian).
Slater L.J. Generalized hypergeometric functions – Cambridge, 1966, 273 p.
Verdiev I.A. Group$SO(2,1)$and duality, Nuclear Physics, 1974, v. 20, issue. 4, pp. 819-826. (In Russian).
Vilenkin N.Y, Special functions and theory of groups representation, M.: Nauka, 1965, 588 p. (In Russian).

Astronomy & Astrophysics (Caucasus) 2, (2016) (81-89)

THE ROTATION OF SOLAR PROMINENCES IN HYDROGEN LINES

M. Sikharulidze [1,2], R. Chigladze[1,2], D. Khutsishvili[2,3], T. Kvernadze[2], E. Khutshishvili[2]

1. Samtskhe-Javakheti State University, Akhaltsike, Rustaveli Street #106, Georgia
2. E. Kharadze Abastumani Astrophysical Observatory at the Ilia State University, 3/5 Cholokashvili str., 0162 Tbilisi, Georgia
3. Ivane Javakhishvili Tbilisi State University, 1 Chavchavadzeave., 0162 Tbilisi, Georgia

Email:revazchigladze@yahoo.com

Received October 24, 2016; revised December 1, 2016

Abstract

One of the main directions of researches in solar physics is the study of ongoing physical processes in solar prominences and their "feet". To study the velocities of plasma motions in prominences, the spectral observational data in Hα and D_3 were obtained in years 2012-2015 using 53-cm non-eclipsing coronagraph of Abastumani Astrophysical Observatory.

The following main results were obtained: in 40% of all 227 spectral images of Hα prominences, the asymmetry of temporal variations of Doppler velocities and spectral line FWHM are seen; for D_3 prominences, 320 spectral images were processed, out of which 70% show the asymmetry of temporal variations of Doppler velocities and spectral line FWHM; for Hα prominences, the Doppler velocities vary between 3-10 minutes and FWHMs vary between 5-12 minutes; for D_3 prominences, the Doppler velocities vary between 7-10 minutes and FWHMs vary between 5-10 minutes.

Key words: Solar atmosphere., Prominences., Doppler velocities

1. Introduction

The prominences are one of the active structures in solar atmosphere, which are cooler ($T=10^4$ K) and denser ($n=10^{10}–10^{11} cm^{-3}$) chromospheric plasma "clouds" ejected to the corona during the explosion in the lower layers of the solar atmosphere. At the solar limb, they are observed in the spectral lines of H, He, Ca+ and others as bright clouds of different structure or arcs. On the solar disc, they are observed as the group of dark fibers located in the zones of sunspot formation (sometimes in high latitudes).

The prominences (see Fig. 1) are quite large structures and reach several hundred thousand kilometers from the solar limb to corona while along the solar limb, they usually spread only for 6,000-10,000 km. The prominences and spicules are the main sources of material exchange between chromosphere and corona (Gilbert et al., 2000; Delannee et al., 2000). An obvious sign of it is the observed plasma motion velocities in the solar prominences and spicules. The creation of prominences is directly associated with the evolution of the solar sunspot groups.

The classification of the prominences is done by their characteristic forms, motion velocities and inner dynamics: Quiescent, Active, Eruptive, Coronal and Arch.

Figure 1. The huge prominence is seen at the solar limb, whose plasma is supported by magnetic field loops. The size of this prominence is about 600,000 km, 4 times larger than that of Jupiter and 46 times larger than that of the Earth.

2. Observation and data processing

Every stage of advances of the solar atmosphere observational technique and methods since the first observations of the solar eclipse through modern space-based observations and development of the large non-eclipsing coronagraphs provided certain observational results and knowledge of the solar fine structure. The improvements of active solar structure studies are mainly connected with the innovations in the observational technique and methods.

The development of the large non-eclipsing coronagraph by Nikoilsky and Sazanov (1966) with the main objective diameter of 53 cm and focal length of 8 m, allowed to obtain new observational data. The advantage of high spatial and spectral resolutions of this coronagraph caused significant improvements in the studies of structure and dynamics of the active chromospheric and coronal structures.

The coronagraph of Abastumani Astrophysical Observatory is equipped with Ebert-Fast spectrograph having 230mm x 250mm diffraction grating. The grating has 600 lines per mm and the highest concentration in the visual spectral range located in the second order. The spectral dispersion is equal to 0.96 Å/mm and spectral resolution in the second order is equal to 0.04 Å. The linear diameter of the solar disc at the spectrograph slit equals 125 mm. The diameter of the collimating mirror is 360 mm and the camera mirror is 420 mm with focal length of 8 m for both. The spectrograph is equipped with Apogee U9000 CCD having 3056x3056 array, 12x12 μm pixel size and 36.7x36.7 mm linear size.

During the 2012-2015 observational runs, we obtained spectral images of Hα spicules and D_3 prominences for 5,500-10,000 km heights from the solar limb with high cadence and period of time reaching 10-15 min (see Fig. 2). The exposure time is 0.3 sec.

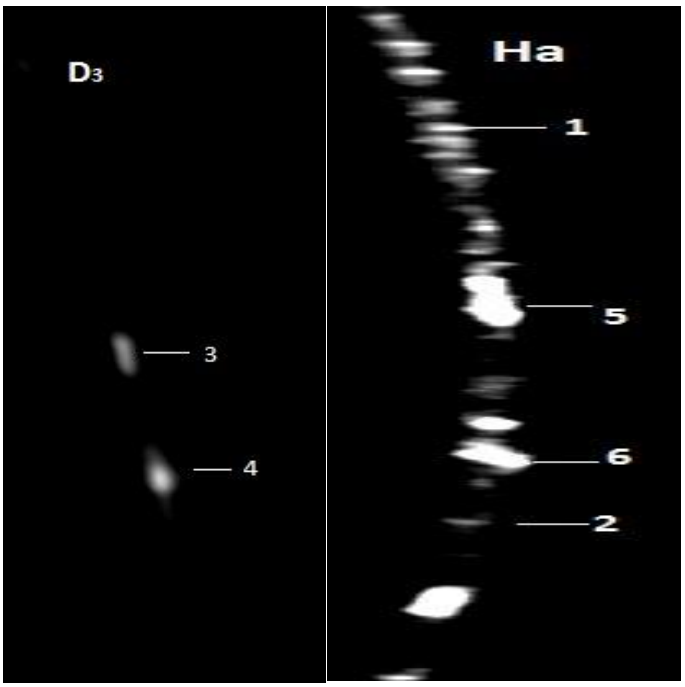

Figure 2. The spectral images of D_3 prominences and Hαspicules (1 and 2 are Hα spicules; 3,4,5 and 6 are D_3 and Hαprominences)

The data processing of these observational data was done by using special software AImaP V.3.59 developed at Abastumani Astrophysical Observatory, which has very convenient graphical interface and allows measuring the Doppler and tangential velocities, as well as FWHM of spectral lines. The software uses Gaussian fitting of the spicules, prominences and reference spectral lines and calibrates the pixel distances between the Gaussian centroids into Doppler velocities (see Fig. 3).

Further time-series processing was done by using Lomb periodogram method (Press et al. 1992), which is especially suitable for observations unevenly spaced in time.

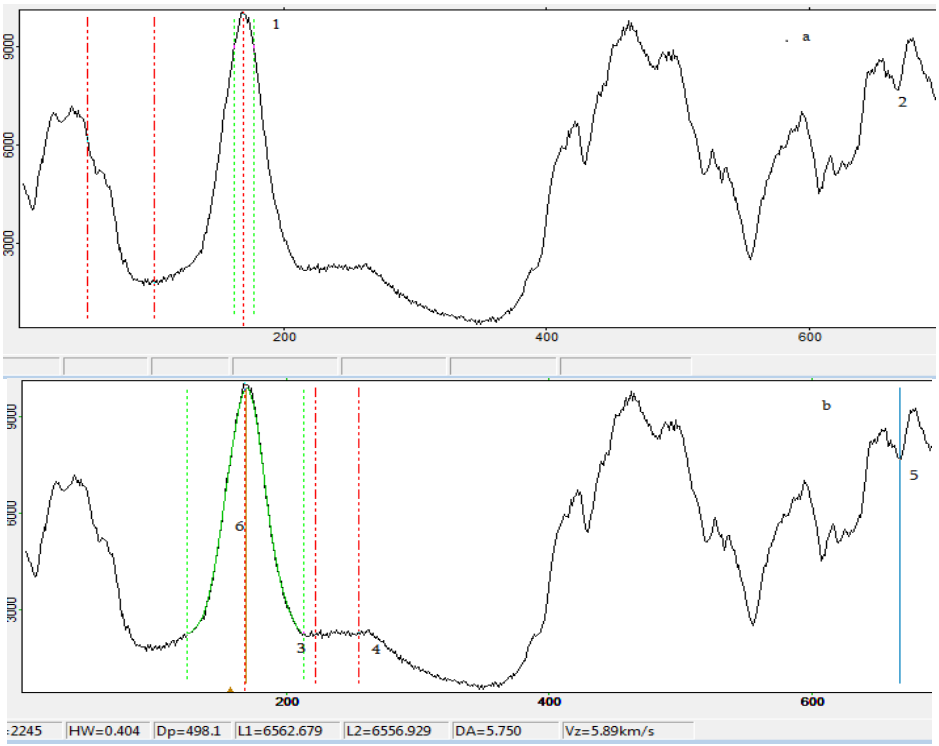

Figure 3. The profiles of spicules and reference spectral lines

3. Data analysis

One of the main directions of the studies of the solar physics is the study of physical processes taking place in the prominences and their "feet". Many authors (Costa et al. 2004; Labrosse et al. 2010; Mackay et al. 2010; Arregui & Ballester, 2011) studied rotational motions and oscillation characteristics of plasma in the prominence feet. The authors attribute the oscillations observed in the feet to the global photospheric and chromospheric oscillations with periods being equal to 3 and 5 min.

The authors (Oliver, & Ballester 2002; Yi & Engvold 1991; Lin 2004; Díaz 2005) studied the periods of oscillations of plasma in tubes and fibers of prominences using high resolution observations and found that these periods vary between 3-20 min. These results raise the main question: are these periodical oscillations always associated with structural changes in the prominences? Díaz et al. (2001) analyzed digital researches and concluded that the fibers are rather oscillating in groups than individually.

This problem is extremely interesting as the studies in this direction will allow better understanding the nature of physical processes taking place in the prominences and also transfer of matter and energy towards the corona. Processing and analyzing the observational data obtained in Abastumani (Hα and D_3 prominences - see Fig. 4) will improve our knowledge in this field.

For more effective study of this problem it would be necessary to match and identify ground-based and space observations of the prominences. Each prominence has to be identified and the time difference between the observations should be close to zero. The sample of such identification is shown in Fig. 5. The both images are taken on October 19, 2012, and the exposures match exactly. The image scales are not identical, but they were corrected during the data processing.

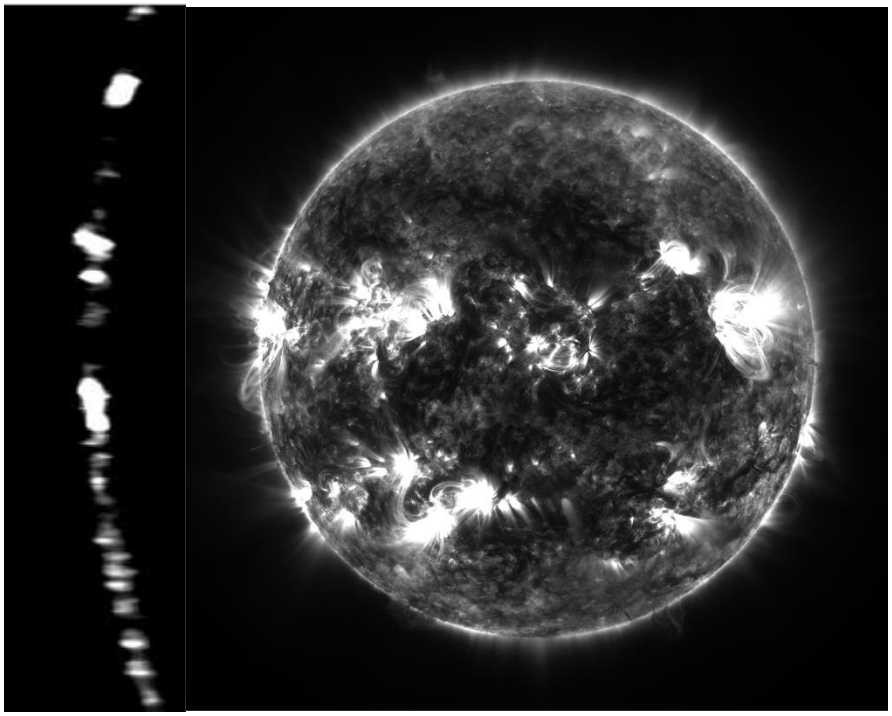

Figure 5. The left image shows Hα spectra of the spicules and prominences taken with a large non-eclipsing coronagraph of Abastumani Astrophysical Observatory and the right image is that of the Sun taken from the space.

We processed 227 Hα and 320 D_3 spectral images and measured the Doppler velocities and FWHMs. The temporal variations of the Doppler velocities and FWHMs of 2 randomly selected Hα

prominences are shown in Fig. 6. The temporal variations of the Doppler velocities and FWHMs of 2 randomly selected D_3 prominences are shown in Fig. 7.

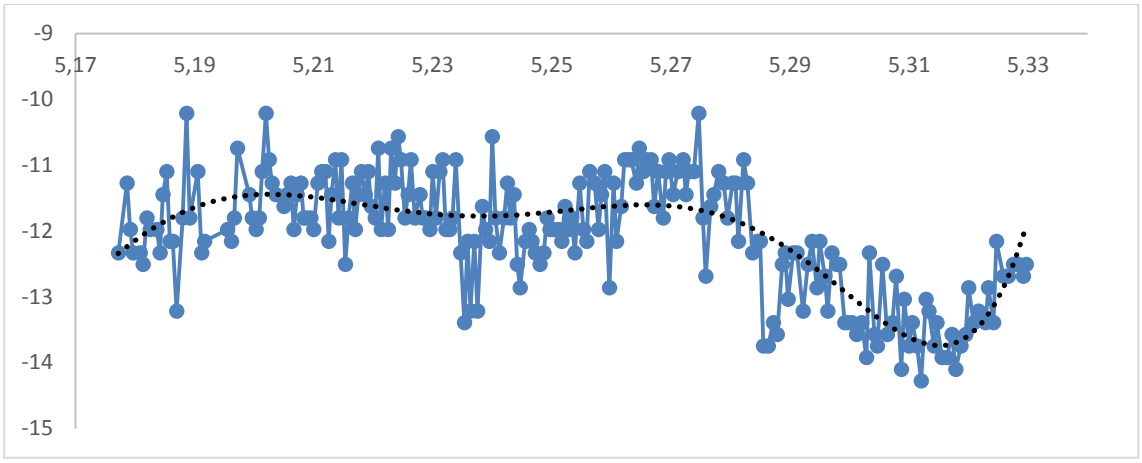

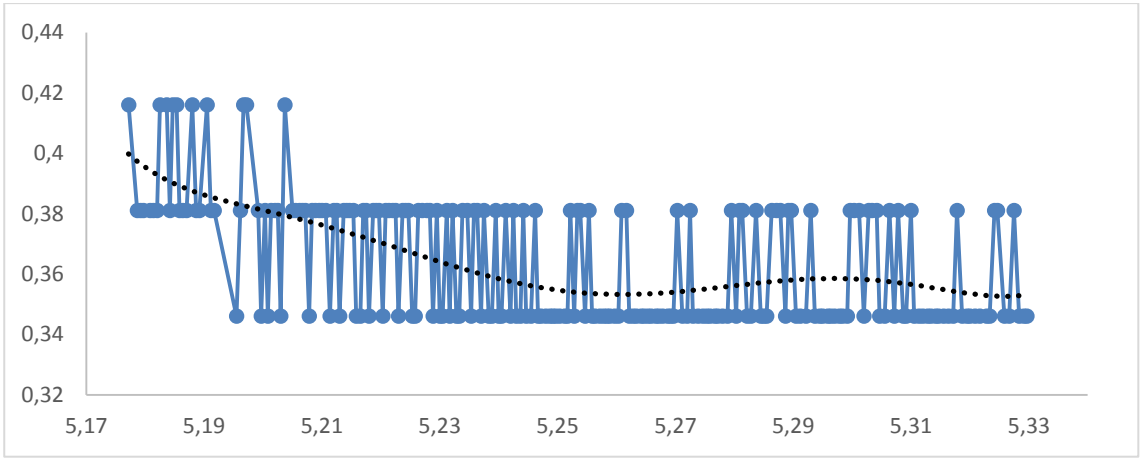

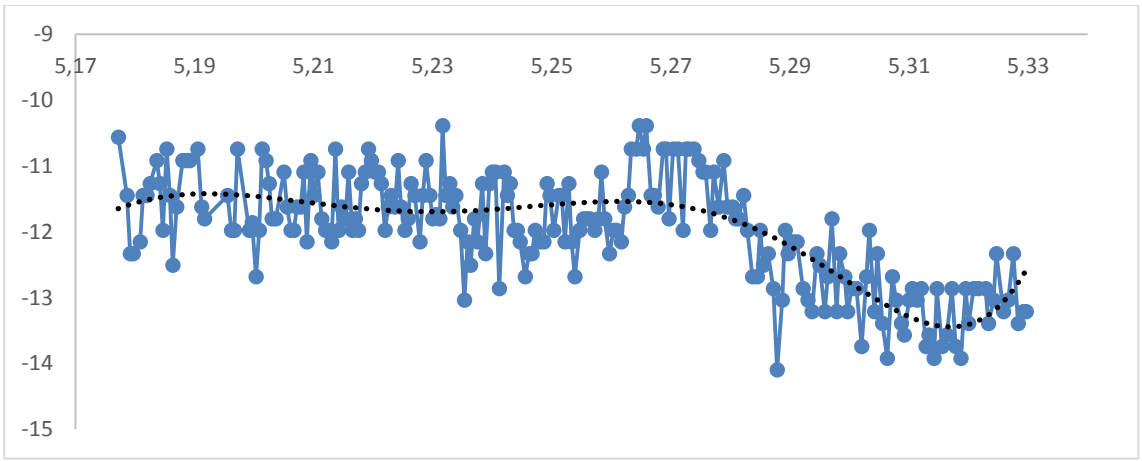

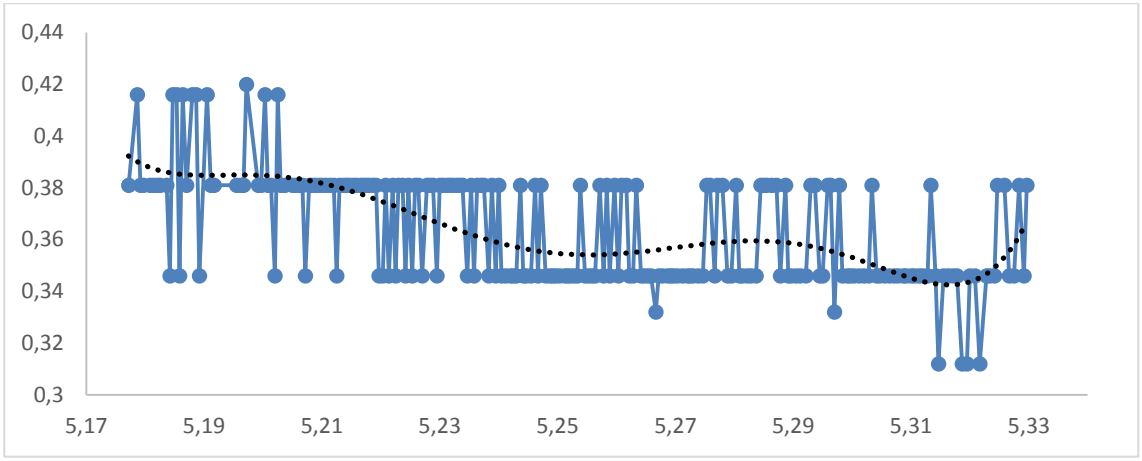

Figure 6. The temporal variations of the Doppler velocities and FWHMs of 2 randomly selected Hα prominences.

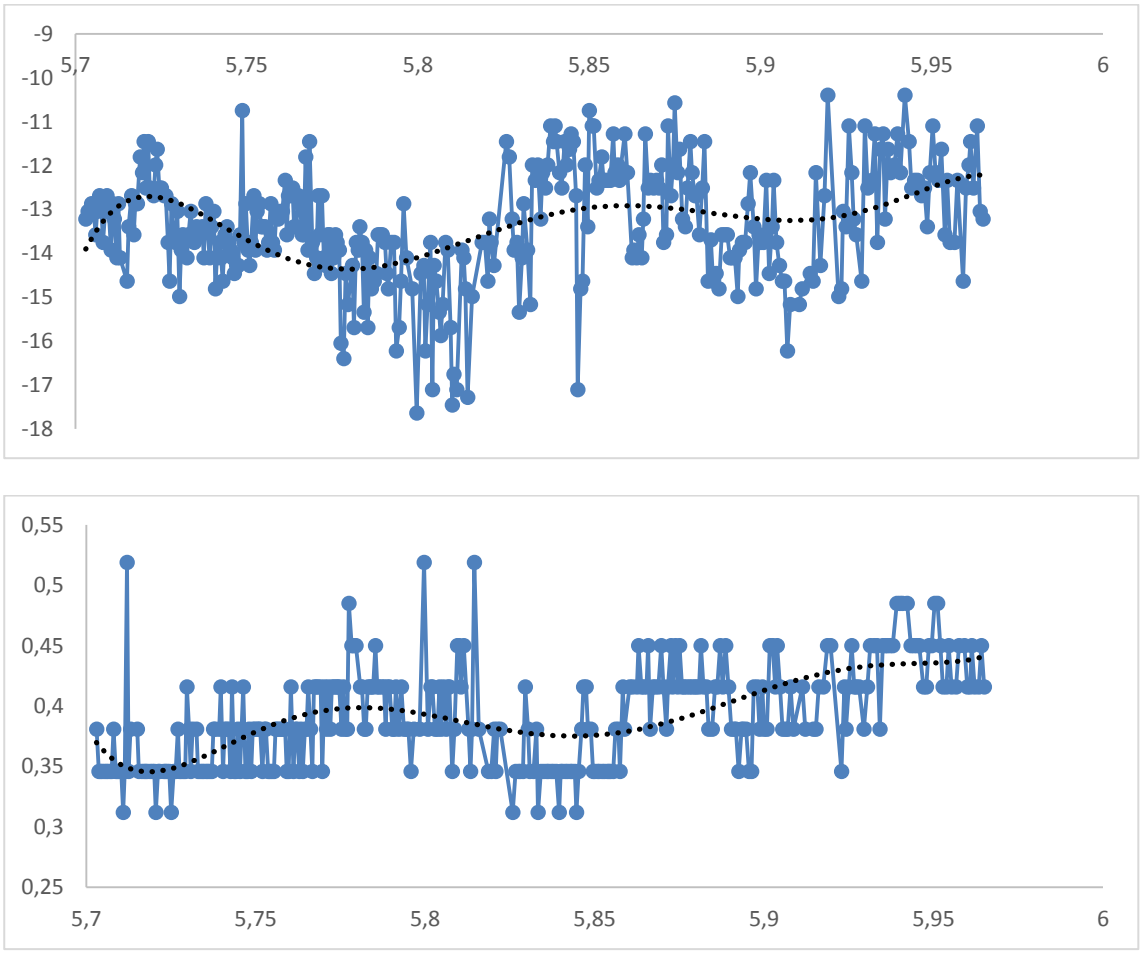

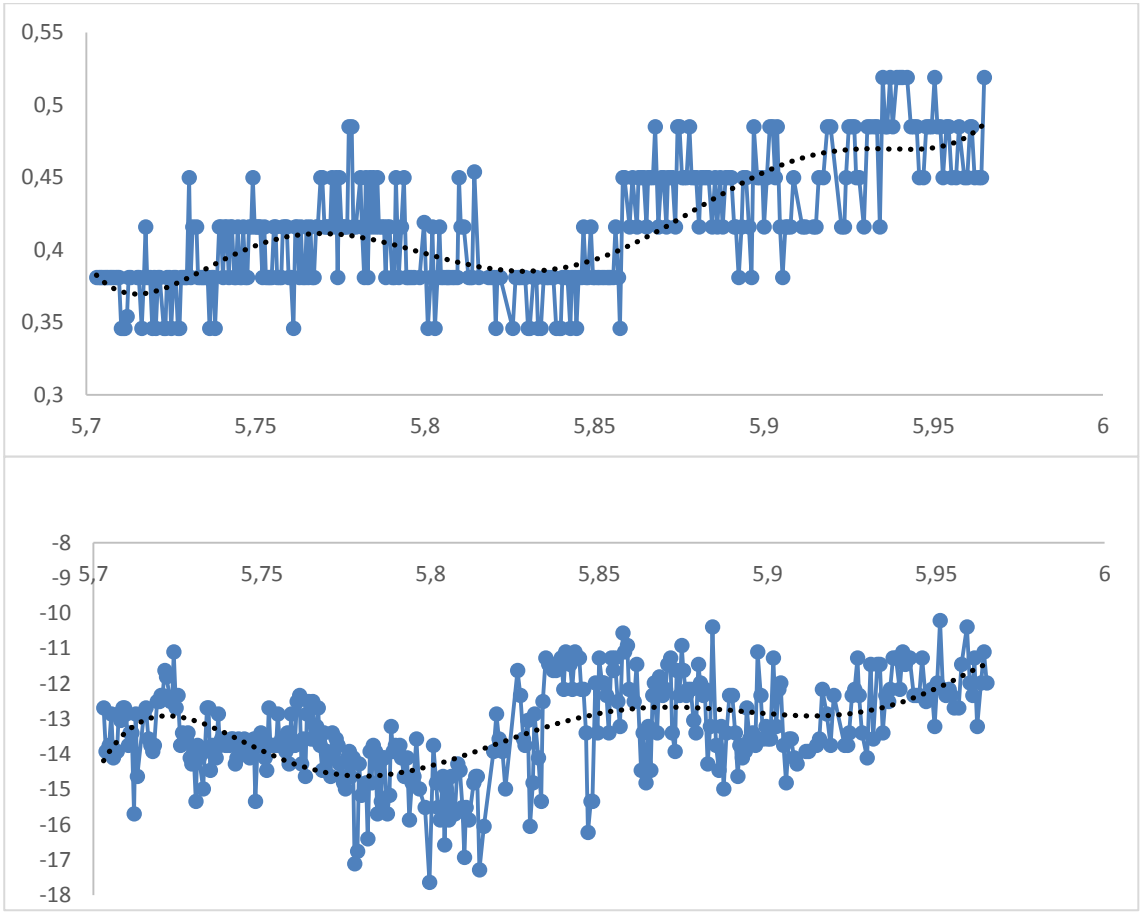

Figure 7. The temporal variations of the Doppler velocities and FWHMs of 2 randomly selected D_3 prominences.

Our observational data show that the Doppler velocities in the feet of Hα prominences vary between 9-15 km/sec and in the feet of D_3 prominences vary between 8-18 km/sec.

In Fig. 6, the asymmetry of temporal variations of the Doppler velocities and FWHMs in Hα prominences is slightly seen in the upper 2 drawings, while there is no asymmetry seen in the 2 drawings below. In all the 227 spectra, the asymmetry is seen in 40% of images.

The asymmetry of temporal variations of the Doppler velocities and FWHMs in D_3 prominences is seen better (see Fig. 7). In all the 320 spectra, the asymmetry is seen in 70% of images.

The periodograms of temporal variations of the Doppler velocities and FWHMs were studied and the oscillation periods were estimated (see Fig. 8 and Fig. 9).

The periods of temporal variations of the Doppler velocities in Hα prominences vary between 3-10 min and those of the FWHMs - vary between 5-12 min (see Fig. 8).

The periods of temporal variations of the Doppler velocities in D_3 prominences vary between 7-10 min and those of the FWHMs - vary between 5-10 min (see Fig. 9).

The groups of periods were identified to their confidence levels in the power spectrum are above 95 %.

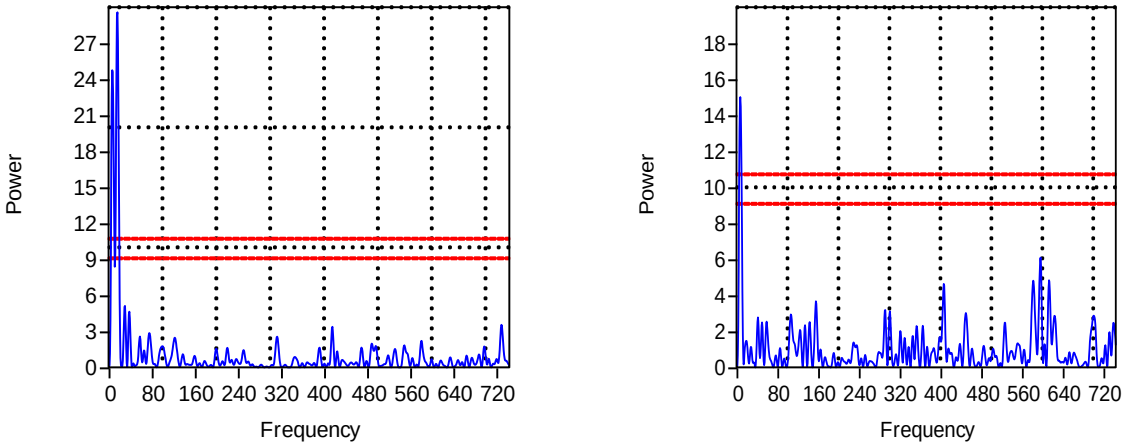

Figure 8. The oscillation frequencies of temporal variations of the Doppler velocities and FWHMs in Hα prominences

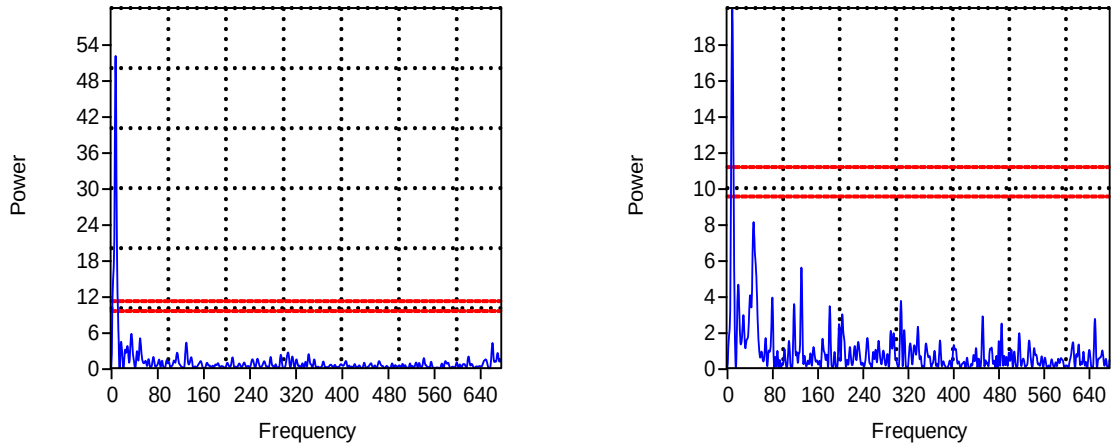

Figure 8. The oscillation frequencies of temporal variations of the Doppler velocities and FWHMs in D_3 prominences

4. Conclusions

For all the 227 spectra of Hα prominences, the asymmetry of temporal variations of the Doppler velocities and FWHMs is seen in 40% of images. In all the 320 spectra of D_3 prominences, the asymmetry of temporal variations of the Doppler velocities and FWHMs is seen in 70% of images.

The periods of temporal variations of the Doppler velocities in Hα prominences vary between 3-10 min and those of the FWHMs - vary between 5-12 min. The periods of temporal variations of the Doppler velocities in in D_3 prominences vary between 7-10 min and those of the FWHMs - vary between 5-10 min.

Acknowledgements: The work is supported by the Shota Rustaveli National Science Foundation grant FR/417/6-310/13.

References

Arregui, I., &Ballester, J. 2011, Space Science Reviews, Volume 158, Issue 2-4, pp. 169-204

Costa A., R. González, and A. C. Sicardi Schifino, 2004, Stability analysis of quiescent prominences using thermodynamic irreversible energy principles, A&A 427, 353–361

Delannee, C., Delaboudiniere, J.-P., & Lamy, P. 2000, A&A, 355, 725

Díaz A. J., R. Oliver, and J. L. Ballester, 2005, Astronomy and Astrophysics, Volume 440, Issue 3, September IV 2005, pp. 1167-1175

Díaz, A. J.; Oliver, R.; Erdélyi, R.; Ballester, J. L., 2001, Fast MHD oscillations in prominence fine structures, Astronomy and Astrophysics, v. 379, p. 1083-1097

Gilbert, H. R., Holzer, T. E., Burkepile, J. T., & Hundhausen, A. J. 2000, ApJ, 537, 503

Labrosse, N., Heinzel, P., & Vial, J. C. 2010, Space Sci. Rev., 151, 243

Lin, Cheng-Horng, 2004, Repeated foreshock sequences in the thrust faulting environment of eastern Taiwan, Geophysical Research Letters, Volume 31, Issue 13, Cite ID L13601

Mackay, D. H., Karpen, J. T., Ballester, J. C., Schmieder, B., &Aulanier 2010, Space Sci. Rev., 151, 333

Oliver, Ramón; Ballester, José Luis, 2002, Oscillations in Quiescent Solar Prominences Observations and Theory (Invited Review), Solar Physics, v. 206, Issue 1, p. 45-67

Press, W.H., Teukolsky, S.A., Vetterling, W.T., Flannery, B.P.: Numerical Recipes in C. The Art of Scientific Computing. Cambridge University Press, Cambridge (1992)

Yi, Zhang; Engvold, Oddbjorn, 1991, Solar Physics (ISSN 0038-0938), vol. 134, p. 275-286.

Chronicle

Giorgi Malasidze (1936 - 2016)

Giorgi Malasidze was born on May 1, 1936, in village Didi Chailuri of Sagarejo Region, Georgia. In 1955, he finished his secondary school studies and in 1962, he enrolled in Ivane Javakhishvili Tbilisi State University, Faculty of Mechanics and Mathematics.

In 1962, Giorgi Malasidze started to work at Abastumani Astrophysical Observatory as a senior scientific worker. In 1965-1968, he studied at a graduate school with the specialty of star dynamics. His scientific leader was Roman Dzigvashvili, an outstanding scientist in this field.

In 1971, Giorgi Malasidze defended his Candidate's thesis "The study of plain star orbits in the gravitational potential field in ellipse integrals" and was conferred a scientific title of a Candidate of Physical-Mathematical Sciences.

In 1972, Professor Giorgi Malasidze started to work at Georgian Technical University, the Chair of Theoretical Mechanics, and in 1988, he started to work simultaneously at Ivane Javakhishvili Tbilisi State University, Chair of Astronomy where he delivered a major course in sky mechanics and star astronomy.

In 2003, Giorgi Malasidze defended his Doctoral thesis on topic "Methods of modeling the gravitational field of star systems and study of the galactic orbits of the stars" and was conferred a scientific title of a Doctor of Physical-Mathematical Sciences.

In 2007, Giorgi Malasidze started to work at Samtskhe-Javakheti State University, Faculty of Engineering and Agrarian and Natural Sciences where he delivered lectures to the students of all three degrees.

Professor Giorgi Malasidze was a scientific leader of a number of candidate and doctoral dissertation theses and was his students' favorite lecturer. Term "Kuzmin-Malasidze gravitation

potential" has long been introduced to the scientific literature. The Professor contributed much to the solution of the actual problems of star dynamics.

Professor Giorgi Malasidze was a chairman of the Doctoral Dissertation Supervisory Committee at Samtskhe-Javakheti State University, in the field of astronomy, member of the editorial board of scientific journal "The Astronomy and Astrophysics" and author of more than 70 scientific works.

Professor Giorgi Malasidze was distinguished for the unique properties of a great scientist and teacher, faith, professionalism and great erudition in every position he served.

Professor Giorgi Malasidze died in August of 2016 and was buried in his native village Didi Chailuri of Sagarejo Region.

Astronomy & Astrophysics (Caucasus) 2 (2016)

Key Words

Absorption coefficients' NH3 λ 6475 Å band
Atmospheres of Jupiter and Saturn
Bursts
Chromospheric flare
Chromosphere
Continuousseries
Correlation length
De Sitter space
Doppler velocities
Discrete series
Electrophotometric observations
Evolution of massive stars
Line formation
LBV
Massive stars
Polarization-holographic
Polarization-sensitive materials
Prominences
P Cygni
Radiative
Radio
Radio emission
Representation of Lie group
Rpectral lines
Solar atmosphere
Spicules
Stokes astropolarimeter
Sunspots
Supplementary series
Transfer
Turbulent atmosphere
Wigner coefficients
WRs

Astronomy & Astrophysics (Caucasus) 2 (2016)

Author Index for Volume 2

Astronomy & Astrophysics (Caucasus)

Scientific paper Submission

The submitted article's technical parameters are the same as in the USA leading international scientific journals.After the positive review only astronomy and astrophysical original articles will be published in this journal.

The manuscript should be presented in A4 format. The size of the article ,including bibliography and other types of enclosure should not exceed 20 pages printed with 1interval and 12 sized font.

It is possible to submit the online version of the manuscript but is should be written only in English. (Text must be typed in Times New Roman, MS word or Pdf file)

The text should be written on the whole page and not separately on twocolumns,the same as in this journal.

Structure of the paper:

Title of the paper:

Author/authors:

Name of the author/authors,firstname,secondname, working place,country and online address must be presented below the manuscript title.

Abstract

The abstract must be informative.Shouldrepresent the content of the paper,describe the goal of the research,symmerize results of the survey and show its theoretical and practical importance.The abstract should not exceed more than 250words,nearly one page.

Key words: Authors should provide key words,which are relevant to the topic.Maxium amount of the words should be 8 . Use only commonly used shortenings .

Introduction: Authors should highlight the essence of the problem, their sub-aims,what is their hypothesis,importance of their paper and what have been done peviously in this field.

Methods: The article should be build methodologically correct way. It should reflect the usage of modern research methods.

Results: Results must be described clearly and briefly**.** Each illustration should have its inscription**.** Number the tables used in the text consistently.

Analysis: This paragraph should investigate the importance of the paper results.You should compare your result to the previous ones**.**

Conclusions: The main conclusion can be written in this paragraph**.**

Acknowledgment: At the end of the paper on the separate chapter you should express your gratitute to those people who helped you during the research.

Literature citation: Consider that every source you have used in this paper is also indicated in the bibliography or vice versa.

Sources Reference Style: The literature quoted in the scientific publication should be indicated with round brackets.(Sort version:name of the author and the rule of the article publication**.**

Reference: Nominated literature where the author's identity is indicated fully,the date of the publication and appropriate page should be arranged alphabetically.

It will be published twice in a year.

The paper should be send to the following e-mail address: astronomy@sjuni.edu.ge

CONTENTS

Publishing Groupi: **L. Gurgenidze**
L. Zedginidze

Correctional: T. Dolidze

Publishing-House
„Akhaltsikhe University”

Akhaltsike, Rustaveli Street №106
Tel.: 0(365)22-19-90, 591-41-12-78
E-mail: astronomy@sjuni.edu.ge